Probing the electronic properties of bulk and monolayer crystals of tungsten dichalcogenides using magneto-spectroscopy

Anatolie Mitioglu

Université de Toulouse

THÈSE

En vue de l'obtention du

DOCTORAT DE L'UNIVERSITÉ DE TOULOUSE

Délivré par : *l'Université Toulouse 3 Paul Sabatier (UT3 Paul Sabatier)*
Cotutelle internationnale *Institut de Physique Appliquée*

Présentée et soutenue le *6 Juillet 2015* **par :**

ANATOLIE MITIOGLU

Probing the electronic properties of bulk and monolayer crystals of tungsten dichalcogenides using magneto-spectroscopy

-

Etude des propriétés électroniques de monocristaux massifs et monocouches de dichalcogénures de tungstène par magnéto-spectroscopie

---

JURY

ADNEN MLAYAH	Professeur des Universités	Président du jury
LUIS VIÑA	Professeur des Universités	Rapporteur
MARK-OLIVER GOERBIG	Chargé de Recherche	Rapporteur
MARIA VLADIMIROVA	Chargé de Recherche	Examinateur
PAULINA PLOCHOCKA-MAUDE	Chargé de Recherche	Directrice de Thèse
LEONID CULIUC (KULYUK)	Professeur des Universités	Co-Directeur de Thèse

---

École doctorale et spécialité :
SDM : Physique de la matière - CO090
Unité de Recherche :
Laboratoire National des Champs Magnétiques Intenses (UPR 3228)
Directeur(s) de Thèse :
Paulina PLOCHOCKA-MAUDE et *Leonid CULIUC (KULYUK)*
Rapporteurs :
Luis VIÑA et *Mark-Oliver GOERBIG*

Acknowledgments

.

Contents

Chapter 1

Electronic properties of bulk and monolayer tungsten dichalcogenides

Contents

1.1 Introduction

Layered compounds involving transition metals from group VI and chalcogens (the so-called dichalcogenides) are promising candidates for exploring atomically thin structures. The basic building block referred to as "monolayer" consists of three atomic layers: the layer of transition metal atoms is sandwiched between two layers of chalcogens.[1] All the dichalcogenides have a strong intra "layer" chalcogen-metal covalent bond while, the layers are weakly held together by van der Waals forces. Nevertheless, the inter layer coupling plays a significant role in the electronic properties. Bulk crystals are semiconductors with an indirect gap in the near infrared spectral range [Coehoorn 1987]. In contrast, monolayer transition metal dichalcogenides such as molybdenum disulfide (MoS_2), molybdenum diselenide ($MoSe_2$), tungsten disulfide (WS_2) or tungsten diselenide (WSe_2) are two dimensional (2D) semiconductors with a direct gap in the *visible spectral range* at the **K**+ and **K**− points of the Brillouin zone [Mak 2010, Splendiani 2010, Eda 2011]. Moreover, the inversion symmetry breaking together with strong spin-orbit coupling in monolayer

[1] Hereafter, the term "monolayer" is used to refer to the triple-layer (X-T-X) of dichalcogenides.

dichalcogenides leads to valley contrasted optical selection rules [Xiao 2012]. As a consequence, under optical excitation the population of each valley can be controlled by the circular polarization of the light. Therefore, monolayer dichalcogenides have been proposed as a building block for "valley-tronics" (see *e.g.* the review of Xu *et al.* [Xu 2014]).

Transition metal dichalcogenides are among the most studied layered compounds that have been isolated in monolayer form from bulk crystals by mechanical exfoliation [Novoselov 2005, Mak 2010, Splendiani 2010], synthesized using chemical vapor deposition (CVD), molecular beam epitaxy (MBE) [Zhang 2014, Zhan 2012], or obtained by liquid exfoliation using different solvents [Cunningham 2012]. The progress in these directions has triggered developments in the field of device fabrication using 2D dichalcogenides. For example, it has recently been demonstrated that a monolayer MoS_2 field effect transistor shows a high current on/off ratios which exceeds 10^8 at room temperature and low standby power dissipation [Radisavljevic 2011]. Other applications include light emitting diodes (LED), sensors, photovoltaic devices and integrated circuits [Ross 2014, Pospischil 2014, Baugher 2014]. Moreover, very recently a unique 2D optical system has been achieved by integrating chemically grown dichalcogenide monolayers with a silver-array supporting narrow surface-lattice plasmonic resonances. The enhanced exciton-plasmon coupling enables radical changes in the emission and excitation processes. This leads to a spectrally tunable and enhanced photoluminescence, as well as surface-enhanced Raman scattering at room temperature [Najmaei 2014, Lee 2015].

In addition to devices and circuits based on individual semiconducting dichalcogenides materials, these materials present opportunities for novel device geometries based on junctions and heterostructures using not only 2D dichalcogenides, but also a combination with others 2D crystals such as graphene, hexagonal boron nitride (hBN), black phosphorous, etc (see *e.g.* the review of Geim *et al.* [Geim 2013]. As a consequence, the properties and physical phenomena in such Van der Waals heterostructure devices are fundamentally distinct from those observed in their individual components. For example, in graphene/WS_2 heterostructures, the spin-orbit interaction affects the transport properties and thus, enables a current modulation exceeding 10^6 at room temperature and a very high ON current [Georgiou 2013]. Moreover, using 1D carbon nanotubes/monolayer MoS_2 heterojunctions, Jariwala et al. have demonstrated a notably different charge transport phenomena called anti-ambipolarity [Jariwala 2013].

In this chapter, we briefly introduce the basic properties of monolayer dichalcogenides and summarize recent discoveries in this rapidly expanding field of research. First, a description of the lattice structure, electronic and optical properties of bulk crystals is given. Next, the electronic structure of the monolayer crystals from first-principles calculations is presented. This is followed by a discussion on the inversion symmetry breaking in a monolayer. Following this discussion, the optical selection rules in 2D crystals, which underly the great application potential of 2D dichalcogenides are explained.

1.2 Bulk crystals

Transition metal dichalcogenides in the bulk form have been extensively studied on an experimental and theoretical basis for decades due to their applications in such areas as photovoltaic solar cells [Levy-Clement 1992], solid lubricants [Prasad 1993], or energy storage [Ballif 1996, Reshak 2003] (and references therein). In this section the electronic band structure of tungsten dichalcogenides, WS_2 and WSe_2, bulk crystals are discussed.

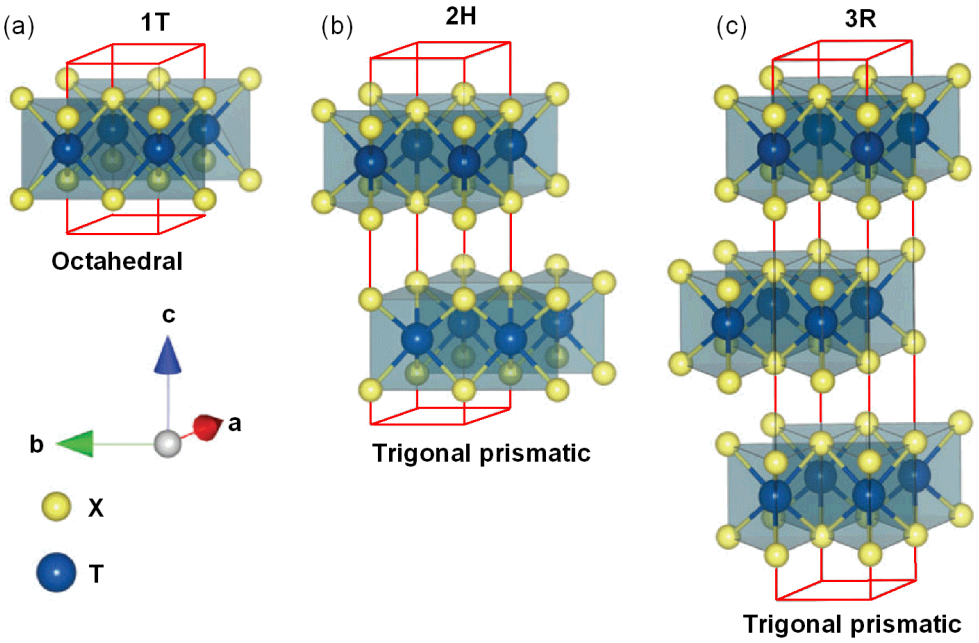

Figure 1.1: The crystal structure of different dichalcogenides polytypes: (a) 1T (tetragonal symmetry, one monolayer per repeat unit, octahedral coordination), (b) 2H (hexagonal symmetry, two monolayers per repeat unit, trigonal prismatic coordination) and (c) 3R (rhombohedral symmetry, three monolayers per repeat unit, trigonal prismatic coordination). The primitive unit cell is indicated by a red line. The chalcogen atoms (X) are yellow and the metal atoms (T) are blue. After Kuc and Heine [Kuc 2015].

1.2.1 Crystal structure

Due to the layered structure of dichalcogenides, most of their physical properties are anisotropic, *i.e.* the in plane and out of plane properties are significantly different. The basic building block for these materials is composed of three hexagonally packed atomic layers where a layer of metal atoms (T = Mo, W) is sandwiched between two layers of chalcogen atoms (X = S, Se) [Wilson 1969]. Due to the strong chalcogen-metal covalent bonds within a single layer and weak van der Waals forces between

layers, it is relatively easy to exfoliate them and obtain a monolayer.

Different possible stacking arrangements of the monolayers give rise to distinct polytypes. Each polytype is given a prefix, *e.g.* 1T, 2H, 3R, where the number refers to the number of monolayers within a unit cell and the letter to the symmetry of the unit cell: trigonal, hexagonal and rhombohedral, respectively. Their structural representations are illustrated in Fig. 1.1. In both 2H and 3R polytypes, the metal atom is situated at the center of a trigonal prism formed by six chalcogen atoms. In 2H polytype (called also trigonal prismatic configuration), the upper layer is rotated by 180 degrees with respect to the lower layer. Thus, the metal atoms are placed above the chalcogen atoms and *vice versa*. In the case of the 3R polytype, each monolayer keeps the previous orientation but, it is translated in the [2,1,0] direction by 1/3 of the lattice constant with respect to the lower layer. Therefore, the chalcogen atoms are placed above the interstices of the previous layer and the metal atoms above the chalcogens. For 1T polytype the coordination is octahedral and the atoms of the underlying monolayers exactly overlap with the monolayers above. Of these three polytypes, only 2H and 3R polytypes are stable and semiconducting, while the 1T polytype is metastable and metallic. We note that it is a convention to denote the polytype as the prefix to the crystal, *i.e.* 2H-WS_2 stands for the 2H polytype of WS_2.

In this thesis, we investigate the bulk and monolayer tungsten dichalcogenides in the 2H form. Figure 1.2(a) shows the crystal lattice in 2H polytype monolayer dichalcogenides. The lattice vectors are given by:

$$\vec{a} = a\left(\frac{\sqrt{3}}{2}\hat{x} + \frac{1}{2}\hat{y}\right)$$
$$\vec{b} = a\left(-\frac{\sqrt{3}}{2}\hat{x} + \frac{1}{2}\hat{y}\right)$$
$$\vec{c} = c \cdot \hat{z}$$

The resulting reciprocal lattice vectors are given by:

$$\vec{a}^* = \frac{4\pi}{\sqrt{3}a}\left(\frac{1}{2}\hat{x} + \frac{\sqrt{3}}{2}\hat{y}\right)$$
$$\vec{b}^* = \frac{4\pi}{\sqrt{3}a}\left(-\frac{1}{2}\hat{x} + \frac{\sqrt{3}}{2}\hat{y}\right)$$
$$\vec{c}^* = \frac{2\pi}{c} \cdot \hat{z}$$

As a consequence, the Brillouin zone has the form presented in Fig. 1.2(b). There are several symmetry points which are important for the electronic structure of TX_2 compounds: (i) the center of the Brillouin zone, *i.e.* the $\mathbf{\Gamma}$ point, where the electronic states are involved in the indirect transitions in bulk crystals and, (ii) the

middle of the edge joining two rectangular faces, *i.e.* the **K** point, where the states are involved in the direct transitions in bulk and monolayer crystals.

The high symmetry points at the Brillouin zone boundary for two-dimensional monolayers are usually labeled as **Q** and **P**. For convenience, and following the convention in the literature, we use throughout this work the same labels as for the 3D bulk crystals where **M** corresponds to **Q** and **K** corresponds to **P**.

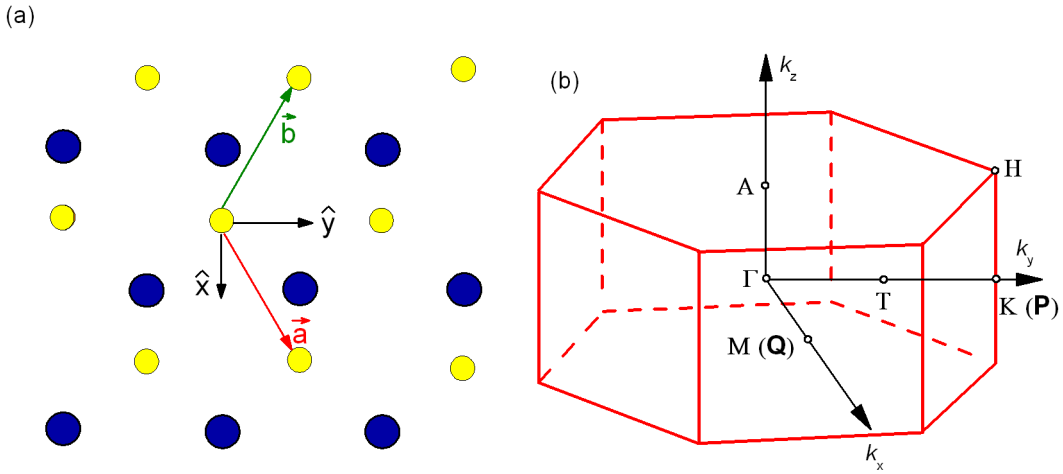

Figure 1.2: (a) In plane lattice vectors marked by green and red colors. Yellow circles denote the chalcogen (X) atoms layer while the blue circles represent the metal atoms (T). (b) Brillouin zone together with the symmetry points of 2H-TX_2 compounds. The labels given in brackets for some of the high symmetry points in the Brillouin zone are sometimes used for 2D systems.

1.2.2 Optical properties and band structure

The calculated electronic band structures of WS_2 and WSe_2 bulk crystals are presented in Figure 1.3 [Roldán 2014]. The calculations reveal an indirect band gap in bulk crystals which is located between the valence band maximum (VBM), situated at the center of the Brillouin zone (**Γ** point), and a conduction band minimum (CBM) between the **Γ** and **K** point (noted as **T**). The red arrows in Fig. 1.3 illustrate the indirect optical transition between these points. The electronic states involved in the indirect transition, *i.e.* the CBM at **T** and VBM at **Γ**, originate from a linear combinations of tungsten d_{xy} and $d_{x^2-y^2}$ orbitals and chalcogen p_z-orbitals. The wave functions have a spatial extension in z-direction, *i.e.* along the c-axis of the crystal. These electronic states exhibit a strong interlayer coupling, and their dispersion strongly depends on the number of layers. The indirect band gap in bulk crystals leads to an extremely weak (negligible) quantum yield for the photoluminescence (PL) [Mak 2010]. In addition to the indirect transitions in bulk

crystals, there is another set of possible direct optical transitions at the **K** point, marked by blue arrows in Fig. 1.3.

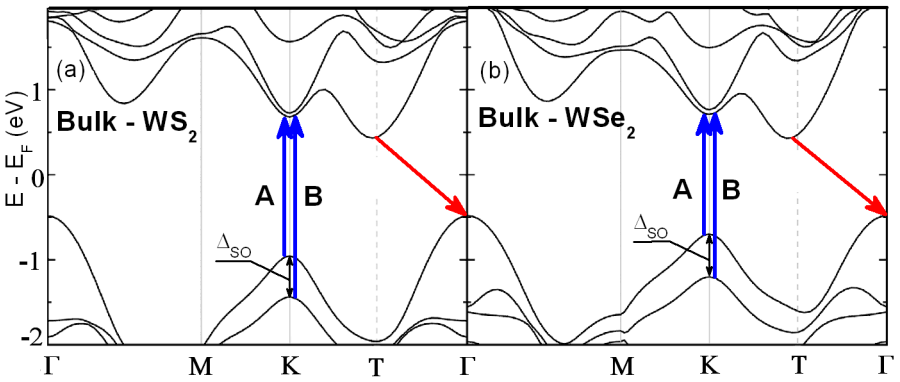

Figure 1.3: Calculated DFT electronic band structures of WS_2 and WSe_2 bulk crystal. The solid red arrows indicate the lowest energy transitions, *i.e.* the indirect band gap, while the blue arrows show the direct transitions associated with the low-energy Wannier excitons (A and B excitons). After Roldan et al. [Roldán 2014].

The electronic states of both valence and conduction bands at the **K** point are mainly associated with the tungsten *d*-orbitals and have weak spatial extension along the *c*-axis. Thus, these electronic states have a two-dimensional (2D) character. The direct transitions at the **K** point can be observed in the optical absorption measurements as two prominent peaks at a energy higher than the indirect transition energy. They are refereed to as A and B excitons [Ballif 1999]. For example, Figure 1.4 shows the absorption measurements of WS_2 bulk crystal with A and B excitons at energies 2 and 2.4 eV, respectively. A and B excitons arise from vertical transitions from a spin-orbit-split valence band to a spin-orbit-split conduction band. The large binding energy of these excitons, which is in the order of $\simeq 50$ meV, suggest that they can be easily observed even at room temperature, where $kT \approx 25$ meV. A strong absorption at higher energies (C peak) which arises from nearly-degenerate exciton states is observed in transmission and reflection measurements due to the band nesting effect [Kozawa 2014].

TX_2	E_g^{ind}(eV)	E_g^{dir}(eV)
WS_2	1.3	2.04
WSe_2	1.2	1.70

Table 1.1: Indirect band gap energies and direct transition energies for WS_2 and WSe_2 bulk crystals at room temperature.

In Table 1.1 are summarized the values of the indirect band gap energy and direct transition energy values determined experimentally by optical or photocurrent measurements on WS_2 and WSe_2 bulk crystals [Kam 1982, Ballif 1999]. The direct

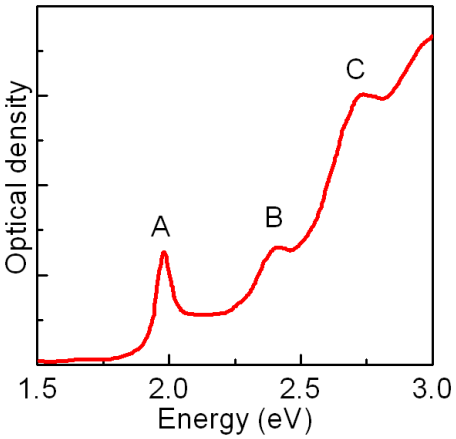

Figure 1.4: Optical absorption spectrum for WS_2 bulk crystal measured at room temperature. The two absorption peaks, noted as A and B, indicate the direct excitonic transitions marked by blue arrows in Fig. 1.3(a). The C denotes the band nesting. After Ballif et al. [Ballif 1999].

transition energies E_g^{ind} were determined by adding a constant exciton binding energy of 60 meV [Beal 1976, Wilson 1969] to the experimentally determined energy position of the excitonic peak A [Ballif 1999].

1.3 Monolayer crystals

The atomically thin dichalcogenide crystals are of interest since their electronic properties are quite distinct from their bulk counterparts. Here, the electronic and optical properties of 2D dichalcogenides crystals are described.

1.3.1 Electronic structure

While reducing the number of layers the electronic band structure evolves to the one presented in Fig. 1.5 for monolayer WS_2 and WSe_2 crystals. The states at the **Γ** and **T** point have a strong metal d-orbital character combined with p_z-orbitals of chalcogen and therefore, strongly depend on vertical interlayer coupling (absent in monolayer). In contrast, the orbitals contributing to the conduction/valence band states at the **K** point are localized within the X-T-X sandwich and do not depend on the number of layers. Decreasing the number of layers, the energy at **Γ** point changes dramatically, while at the **K** point remain practically unchanged. In the monolayer limit, both the VBM and CBM, move from the **Γ** and **T** respectively, to the **K** point of the Brillouin zone. As a result, a monolayer 2H-TX_2 becomes a direct band gap material with an optical transition at the the corner of the Brillouin zone [Mak 2010].

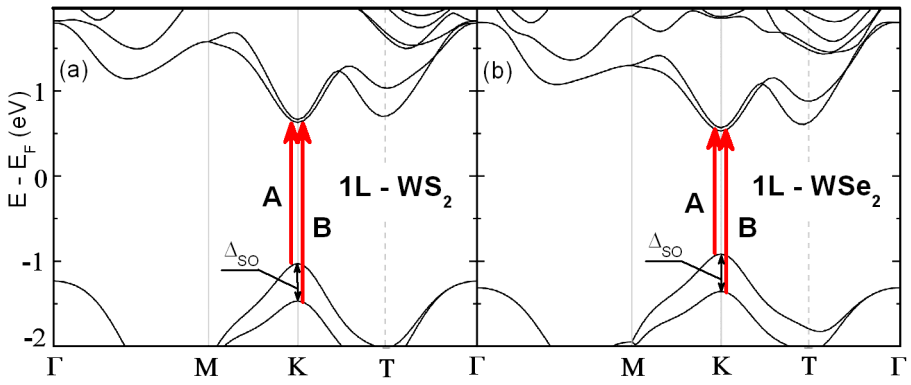

Figure 1.5: Calculated DFT electronic band structures of WS_2 and WSe_2 monolayer crystals. The red arrows show the direct band gap and also the transition associated with the low-energy A and B excitons. Δ_{SO} denotes the energy of the split VBM due to spin-orbit coupling. After Roldan et al. [Roldán 2014].

The optical response of the monolayers is determined by the direct transitions at the **K**+ and **K-** points of the Brillouin zone. Since the electronic structure at the **K** point are almost identical for monolayer and bulk samples, their absorption spectra are roughly similar showing two strong resonances (A and B excitons). However, this is not the case for the PL emission. In monolayer the emission occurs at a significantly different energy than in bulk. Decreasing the number of layers from bulk induces a shift towards higher energies in the PL emission peak in monolayer. This confirms the crossover from an indirect band gap in bulk to a direct band gap in the monolayer limit [Mak 2010, Splendiani 2010]. In Fig. 1.6(a) and (b) are presented the normalized PL spectra for WS_2 and WSe_2 flakes consisting of 1 to 5 layers which illustrate the shift in the energy emission with changing the number of layers. In addition, the PL for monolayer is about two orders of magnitude larger in amplitude compared to that from bilayer and four order of magnitude larger compared to bulk crystals. Figure 1.6(c) and (d) illustrates the change in the PL emission quantum yield (QY) with decreasing the number of layers. Very recent angle-resolved photoemission spectroscopy has directly mapped out the band structure of MoS_2 and $MoSe_2$ [Jin 2013, Zhang 2014]. Similar behavior in the PL emission energy and intensity with decreasing decreasing the number of layers has been observed for the other isoelectronic compounds of this family due to similar lattice structure [Mak 2010, Splendiani 2010].

Additionally, a clear band splitting of VBM at the **K** point of the Brillouin zone in monolayers TX_2 is observed due to the strong spin-orbit coupling as in bulk crystals. The spin-orbit splitting increases with the atomic number of transition metal or chalcogen atom. Due to a heavier mass of tungsten atoms, in tungsten dichalcogenides compounds this splitting is larger ($\simeq$ 400 meV) compared to molybdenum dichalcogenides ($\simeq$ 150 meV). Moreover, the spin-orbit coupling leads also to

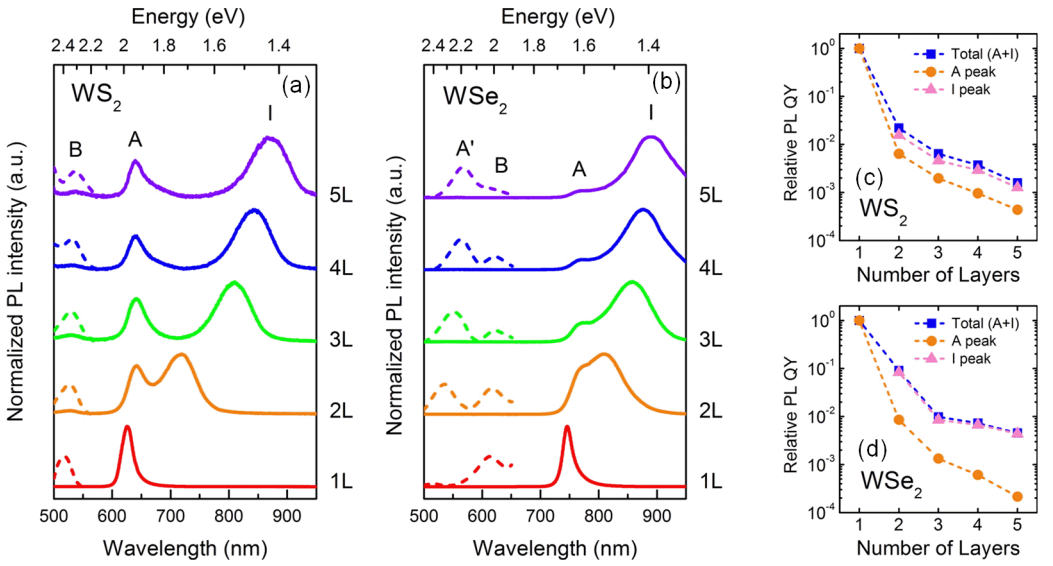

Figure 1.6: (a,b) Normalized PL spectra of exfoliated 2H-WS_2 and 2H-WSe_2 flakes consisting of 1-5 layers. A and B are the direct excitons. Peak I is the indirect band gap emission. The A' and B peaks are typically 100 to 1000 times weaker than the band edge emission peaks and are magnified for clarity. (c,d) Relative decay in PL quantum yield with the number of layers. After Zhao et al. [Zhao 2013].

a splitting of the CBM at both, the band edge at the **K** point and at the secondary minimum **T**, as illustrated in Fig. 1.5. Again, the spin-orbit coupling in the CBM is larger for Se compounds as compared to S compounds. This is expected due to the heavier mass of selenium as compared to sulfur. As the orbital weight of the p_x and p_y orbitals of chalcogen atoms at the **K** point of the conduction band is of the order of $\simeq 20\%$, Cappelluti and co-workers [Cappelluti 2013] proposed that first order processes associated with these X atoms lead to a contribution to the spin-orbit splitting, being more noticeable for the Se compounds.

In Table 1.2 are summarized the direct band gap values determined experimentally by both photoluminescence and absorption measurements, as well as the splitting at the VBM and CBM at the **K** point in WS_2 and WSe_2 monolayer crystals [Roldán 2014, Zeng 2013].

TX_2	E_g^{dir}(eV)	Δ_{VBM}(eV)	Δ_{CBM}(eV)
WS_2	1.95	0.435	0.029
WSe_2	1.64	0.461	0.036

Table 1.2: Optical direct band gaps for WS_2 and WSe_2 monolayer crystals. The spin-orbit splitting of level at the top of valence-band and minimum of conduction-band at the **K** point of BZ.

1.3.2 Excitonic effects

The optical response of monolayer dichalcogenides is dominated by excitonic effects. Upon the absorption of a photon, a valence band electron is excited to the conduction band leaving behind a vacancy (hole) in the valence band. The attractive Coulomb interaction between the negatively charged electron and the positively charged hole bind them into a hydrogen-like state, called as **exciton** (X). The bound electron-hole pair can also capture an extra electron or hole to form a negatively (X^-) or positively (X^+) charged exciton, which is also referred to as **trion** [Kheng 1993]. The binding energy of a neutral exciton is defined as its lowered energy compared to the free electron-hole pair, while the trion binding energy is the difference between $X^\pm$ energy and the unbound state of a neutral exciton, plus a free electron or hole. In the PL spectra this corresponds to the separation between neutral exciton emission energy and charged exciton (X^+ or X^-) emission.

According to the hydrogen model, the energies of exciton levels for a three-dimensional crystal (referred to the bottom of the conduction band) can be evaluated using the following relation

$$E_X^{3D} = \frac{E_B}{n^2}, \tag{1.1}$$

where n=1, 2, 3,... is the principal quantum number and E_B is the 3D exciton binding energy or Rydberg ($R_y^* = \mu e^2/2\hbar^2(4\pi\varepsilon_0)^2\kappa^2$). Here, $\mu = m_e m_h/(m_e + m_h)$ is the reduced mass of the exciton and m_e, m_h are the electron and hole effective masses; κ is the effective dielectric constant. For the n=1 level we have $E_X^{3D} = R_y^*$.

For a 2D system, the energies of exciton levels is given by [Zaslow 1967]

$$E_X^{2D} = \frac{E_B}{\left(n - \frac{1}{2}\right)^2}, \tag{1.2}$$

We can see that in 2D structures, the exciton energies are always deeper in the band gap, implying that the 2D exciton binding energy is increased. For the n=1 level we have $E_X^{2D} = 4R_y^*$, so that the binding energy in a perfect 2D system is four times larger than that of the 3D exciton binding energy. In monolayer dichalcogenides, the excitons are strongly confined in the plane and additionally experience reduced screening due to the change in the dielectric environment outside of the layer. This has major effects on the electronic and excitonic properties of the material. Chernikov and co-workers have proposed that the dielectric screening is reduced because the electric field lines joining the electron and hole begin to extend outside of the sample as shown in Fig. 1.7(a), therefore yielding an even greater enhancement factor. Indeed, the reflectance measurements and two-photon photoluminescence excitation spectroscopy have been used to extract a binding exciton energy of $\sim$ 320 meV and $\sim$ 370 meV in monolayer WS_2 [Chernikov 2014] and WSe_2 [He 2014], which is at least six times larger that in bulk ($\simeq$ 55 meV)[Beal 1976, Bordas 1976], and almost two orders of magnitude larger than that found for the excitons in conventional bulk semiconductors, such as Si and GaAs [Knox 1983]. From the PL

experiments, the trion binding energy, which depends upon the Fermi energy, has been determined to be 20-40 meV [this work] and 30 meV [Jones 2013], in WS_2 and WSe_2, respectively.

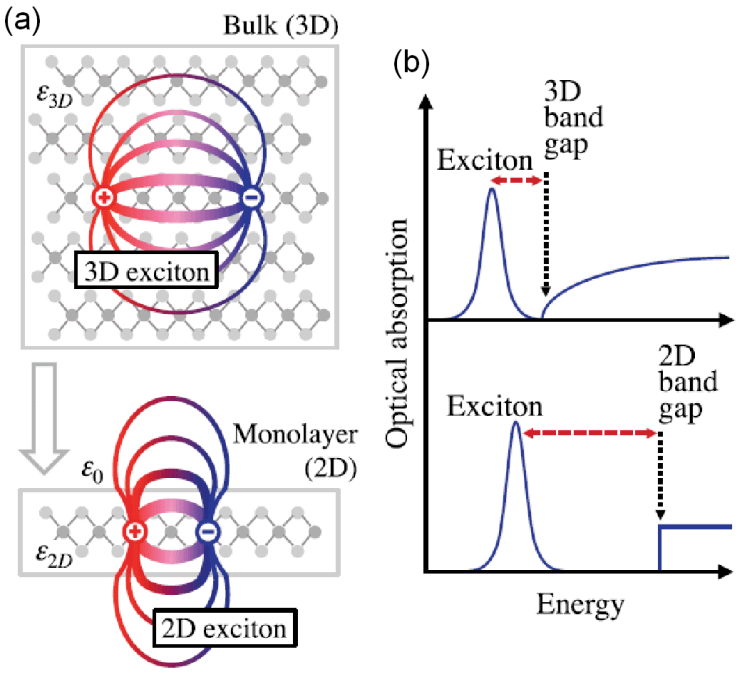

Figure 1.7: Real-space representation of electrons and holes bound into excitons for the 3D bulk and a two-dimensional monolayer. The changes in the dielectric environment are indicated schematically by different dielectric constants ε_{3D}, ε_{2D}, and the vacuum permittivity ε_0. (b) Influence of the dimensionality on the electronic and excitonic properties, schematically represented by optical absorption. The transition from 3D to 2D is expected to lead to an increase of both the band gap and the exciton binding energy. After Chernikov et al. [Chernikov 2014].

Typically, the excitons are classified as Frenkel or Wannier-Mott excitons depending upon the spatial extent of the wave function. In monolayers dichalcogenides, the exciton wave function is larger than the lattice constant like in Wannier-Mott type of excitons, while the binding energy is comparable to that for typical Frenkel excitons. The calculated 2D Bohr radius is about 1 nm [Qiu 2013], so that the wave function for the electron-hole relative motion extends over several tens of unit cells [Ye 2014]. Moreover, the exciton series deviates significantly from the 2D hydrogen model. In the hydrogen model, the orbitals with the same principal quantum number are degenerated. In contrast, for the TX_2 excitons, the GW-BSE calculations have shown that the states with the same shell but of higher orbital angular momentums are at lower energy-levels, that is, $E_{3d} < E_{3p} < E_{3s}$ [Ye 2014]. A theoretical microscopic model, which takes into account the modification of the functional form of the Coulomb interaction due to the nonlocal nature of the effective dielectric

screening, has been successful in explaining these unusually strong electron-hole interactions [Chernikov 2014]. This so-called dielectric confinement or image charge effect [Chernikov 2014, Lin 2014] was also observed in nano-structured materials such as 1D carbon nanotubes [Deslippe 2009] and layered organic-inorganic perovskites [Tanaka 2005].

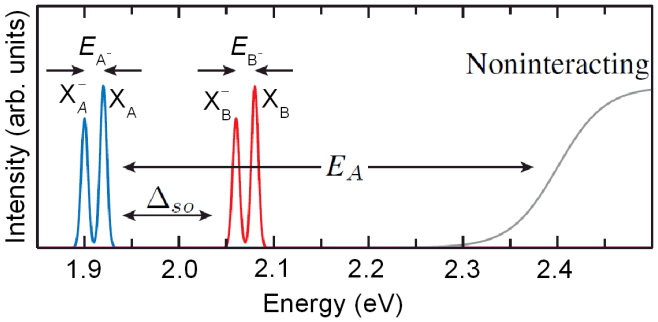

Figure 1.8: Schematic absorption spectrum which shows the A (blue) and B (red) excitons that result from the sizable spin-orbit splitting. After Berkelbach et al. [Berkelbach 2013].

The scenario revealed by experiments to date is summarized in Figure 1.8. The spin-orbit coupling in the valence band give rise to two-distinct excitonic features - the A and B in the schematic absorption spectrum [Berkelbach 2013]. The neutral exciton shows a large binding energy, E_A. The exciton feature exhibit a fine structure, which can be identified with formation of trions (X_A^- and X_B^-), with binding energies $E_A{}^-$ and $E_B{}^-$. Moreover, several recent studies have also demonstrated the generation of others exciton complexes, such as biexcitons (two bound electron-hole pairs) or localized states (due to residual impurities, defects and/or disorder effects), in monolayer dichalcogenides [Jones 2013, He 2014, Shang 2015], akin to those previously observed in quasi-2D semiconductor QWs.

1.3.3 Valley physics from inversion symmetry breaking

It has been theoretically demonstrated that the inversion symmetry breaking in 2D materials leads to contrasted circular dichroism in different k-space regions, which takes the extreme form of optical selection rules for inter band transitions at high symmetry points [Yao 2008]. A monolayer of dichalcogenides has a honeycomb lattice structure in which the inversion symmetry is naturally broken due to two different types of atoms (transition metal and chalcogen), as illustrated in Fig. 1.9(a). As a result of the inversion symmetry, the valleys[2] of energy-momentum dispersion are located at the corners of the hexagonal Brillouin zone, *i.e.* at the **K**+ and **K**− points (see Fig. 1.9(b)). Among the six corners of the Brillouin zone, there exists

[2]The term "valley" simply refers to an energy extrema of Bloch bands in momentum space.

two sets of three equivalent points. As a consequence, we have two inequivalent valleys, which form a *time-reversal pair* with each other. Because the valleys are well separated from each other in momentum space, the inter valley scattering is relatively weak. This leads to a long lived valley polarization, providing an additional degree of freedom in a similar manner as spin polarization [Xu 2014].

To control such an internal degree of freedom of the carriers, it should be associated with a physical property that allows the coupling with an external field so as to manipulate the dynamics. The aim is to control the valley index in a way similar to the manipulation of the spin in conventional semiconductors. The key quantity that allows it is the **orbital magnetic moment** (**m**). Briefly, the orbital magnetic moment arises from the self-rotating motion of the electron wavepacket and it is a pseudovector derived from the periodic part of the Bloch function. From the $k \cdot p$ analysis, the orbital magnetic moment is given by

$$m(k) = -i\frac{e\hbar}{2m_e^2}\sum_{i\neq c}\frac{\mathcal{P}^{ci}(k)\times\mathcal{P}^{ic}(k)}{\varepsilon_i(k)-\varepsilon_c(k)}, \tag{1.3}$$

where $\mathcal{P}^{ci}(k) = \langle u_{c,k}|\hat{p}|u_{i,k}\rangle$ is the inter band matrix element of the canonical momentum operator, $\varepsilon(k)$ is the band dispersion, and $|u_k\rangle$ the periodical part of the Bloch function [Chang 1996, Yafet 1963]. It is important to note that this term is common for all semiconductors and is responsible for the anomalous g-factor of electrons, *i.e.* the Bloch states with opposite spin at the Γ point form a Kramer's pair with opposite orbital magnetic moment which in a magnetic field renormalizes the Zeeman energy thus, changing the effective g-factor [Yafet 1963].

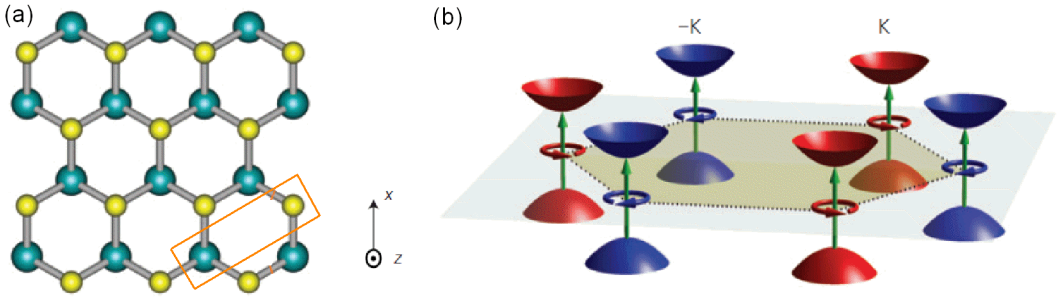

Figure 1.9: (a) A top view of a 2D hexagonal lattice in monolayer dichalcogenides where it can be observed the inversion symmetry breaking because of two different types of atoms. Green and yellow color spheres denote the metal (T) and chalcogen atoms (X). (b) The first Brillouin zone of a monolayer. The red and blue colors refers to the two inequivalent valleys. After Xu et al. [Xu 2014].

The orbital magnetic moment (**m**) is dictated by symmetry considerations such as (i) time-reversal symmetry and (ii) space-inversion symmetry. In the first case, the orbital magnetic moment is odd, *i.e.* $m(k) = -m(-k)$, while in the second case it is even, $m(k) = m(-k)$. In a system with both symmetries, their effect would typically

vanish ($m(k) = 0$). It is important to look for such a physical quantity that allows us to distinguish a *time-reversal pair* of valleys. The orbital magnetic moment $\mathbf{m}$ is a good candidate, since it does not vanish under time-reversal operation. Thus, the orbital magnetic moment $\mathbf{m}$ can have opposite values once an inversion symmetry is broken in the system - such as in a monolayer of dichalcogenides.

If we consider the simplest situation of a two band model, which in the case of a monolayer TX_2 would be the conduction and valence band at the $\mathbf{K}\pm$ valleys, than the carriers can be described by a massive Dirac fermion model [Xu 2014]:

$$\hat{H} = \hbar v_F \left(\tau_z p_x \hat{\sigma}_x + p_y \hat{\sigma}_y\right) + \frac{\Delta}{2}\hat{\sigma}_z, \tag{1.4}$$

where $\tau_z = \pm 1$ is the valley index, v_F is the Fermi velocity and Δ is the band gap. The Pauli matrix $\hat{\sigma}$ is defined in a basis consisting of two d-orbitals of the metal atom with magnetic quantum numbers of $m = 0$ and $m = 2\tau_z$, respectively. For this massive Dirac fermion model [Xu 2014], the orbital magnetic moment has identical values for conduction and valence bands, which has the form:

$$\mathbf{m}(k) = -\hat{\mathbf{z}}\frac{2\hbar^2 {v_F}^2 \Delta}{4\hbar^2 {v_F}^2 t^2 k^2 + \Delta^2}\frac{e}{2\hbar}\tau_z \tag{1.5}$$

At the $k = 0$ point, the value of the orbital magnetic moment has the form $\mathbf{m}(k = 0) = -\hat{\mathbf{z}}\tau_z \mu_B^*$, where $\mu_B^* \equiv e\hbar/2m^*$ is the effective Bohr magneton with the bare electron mass replaced by the effective mass at the band edge. Thus, the valley spin is also associated with an intrinsic magnetic moment, at least for the carriers near the the band edge. The valley-dependent $\mathbf{m}$ makes possible coupling of the valley spin to a magnetic field and the detection of valley polarization as a magnetic signal.

The orbital magnetic moment $\mathbf{m}$ gives rise to the circularly polarized optical selection rules for inter band transitions in monolayer dichalcogenides [Xiao 2012]. As the two valley have opposite $\mathbf{m}$ values, valley-dependent selection rules arises. For the massive Dirac fermion model, the orbital magnetic moment and optical circular dichroism are related by

$$P_{circ}(k) = -\frac{\mathbf{m}(k)\hat{\mathbf{z}}}{\mu_B^*(k)} \tag{1.6}$$

where $P_{circ}(k)$ is the degree of circular polarization for the direct inter band transitions at $k = 0$ point relative to the extreme. Such connections open up the possibility to engineer optical circular dichroism in given bands through the so called "intercellular component" determined by bulk symmetry properties. This has a completely different origin for the selection rules and circular dichroism for optical inter band transitions in solids compared to the one typically observed in conventional semiconductors, where the optical transition selection rules are determined by orbital magnetic moments of the atomic orbits and are called "intracellular component".

1.3.4 Spin-valley coupling and selection rules

The lack of inversion symmetry together with strong spin-orbit coupling leads to coupled spin and valley physics in monolayer dichalcogenides, making possible spin and valley control in these 2D materials. The spin-valley coupling at the valence-band edges suppresses spin and valley relaxation, as flipping a single index (spin or valley) is forbidden by the valley contrasting spin splitting. This results in valley-dependent **optical polarization selection rules** for individual valley. Since time reversal symmetry forces opposite spin-splitting at each valley, this effect can be used to control the valley polarization by means of optical helicity [Xiao 2012], such that the **K**+ valley would correspond to optical selection rules of a certain helicity as well as carriers of a fixed spin, while the **K**− valley would correspond to opposite conditions. This makes possible to control carrier spin and carrier confinement within a specific valley with circularly polarized light, an effect that has been observed experimentally [Mak 2012, Cao 2012, Zeng 2012, Kioseoglou 2012].

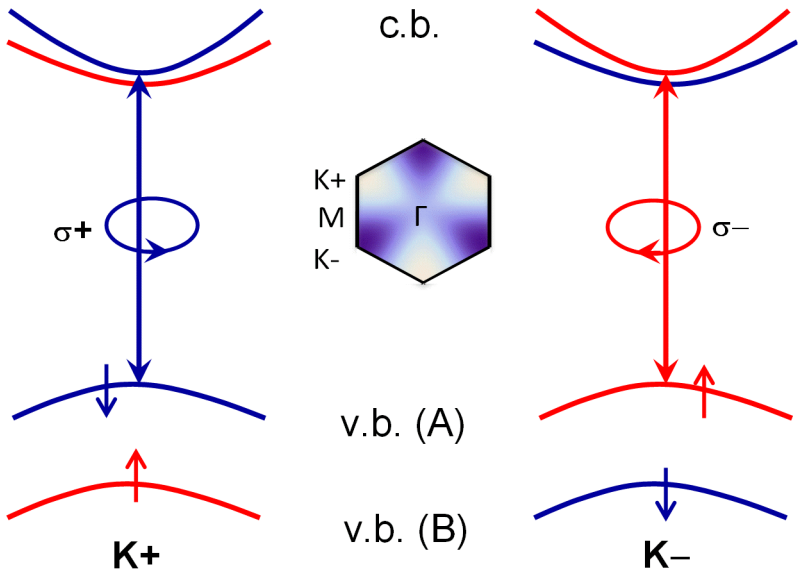

Figure 1.10: Electronic structures at the **K**+ (left) and **K**− (right) valleys illustrating the conduction and valence bands and their spin states. The inset illustrates the hexagonal Brillouin zone with the two inequivalent **K**+ and **K**− points (c.b. labels the conduction band and v.b. labels the valence band).

Let us now look in more details at the optical selection rules from the top of the spin-split valence-band to the bottom of the spin-split conduction band in monolayers. Figure 1.10 shows the valence and conduction bands at the **K**+ and **K**− valleys. The large spin-splitting in the valence bands is induced by the spin-orbit coupling. As illustrated in Figure 1.10, at the **K**+ valley, the spin-down and spin-up holes occupy the VBM(A) and VBM(B) bands, respectively; while at the **K**−

valley the spin occupation is opposite. Since the conduction bands **K**+ and **K**− are spin-split, the light couples only to the orbital part of the wave function and the spin is conserved in the optical transitions[3]. Because of the spin-valley coupling and the valley optical selection rules from inversion symmetry breaking, spin and circular polarization are related in opposite ways at the two energies. Selective excitation of carriers with various combination of valley and spin index becomes possible using optical fields of different circular polarizations and energies. Light with $\sigma+$ circular polarization (blue arrow) generates spin-up electrons and spin-down holes in the **K**+ valley, while the excitation in the **K**− valley is simply the time-reversal of the above.

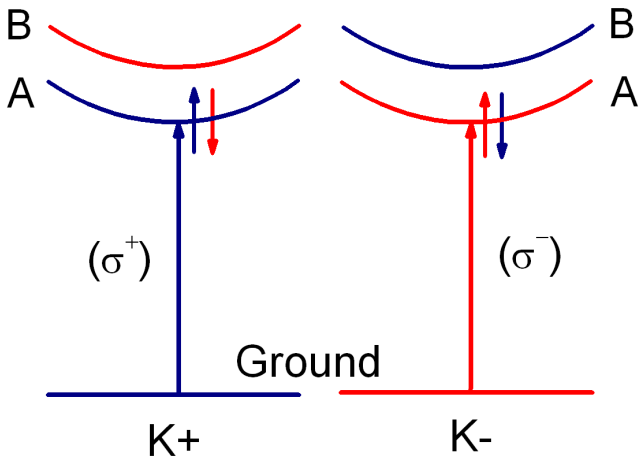

Figure 1.11: Valley neutral exciton optical selection rules in monolayer dichalcogenides for $\sigma+$ and $\sigma-$ circular polarization of the photons.

Since the optical properties of 2D dichalcogenides crystals are dominated by excitons due to their large binding energies, the valley polarization can be probed through charged and neutral exciton emission. Let us consider first the neutral exciton (X) selection rules. When an electron and hole are at different valleys, their direct recombination is forbidden[4], since the momentum conservation cannot be satisfied. If the electron and hole are in the same valley, their recombination is possible with the emission of a photon. Figure 1.11 shows the exciton bands, A and B, formed by holes in VBM(A) and VBM(B), respectively, with electrons in the conduction bands. The lifetime of B excitons is much shorter, due to relaxation to the lower energy configurations through fast non-radiative channels. In the following we focus only on the A excitons. At the **K**+ valley only spin-down holes populate

[3]Here we use a convention that an unoccupied spin-up (-down) state in the valence band is referred as a spin-down (-up) hole.

[4]the so called dark exciton

VBM(A), an A-exciton at the **K**+ valley is formed by a spin-down hole with a spin-up electron. At the **K**− valley, an A-exciton is formed by a spin-up hole with a spin-down electron. Based on these selection rules, a circular polarized light can inject spin- and valley-polarized excitons in monolayer crystals, which in turn recombine and emit circularly polarized photoluminescence. Valley polarization has been reported by several groups in steady-state PL experiments [Mak 2012, Cao 2012, Zeng 2012].

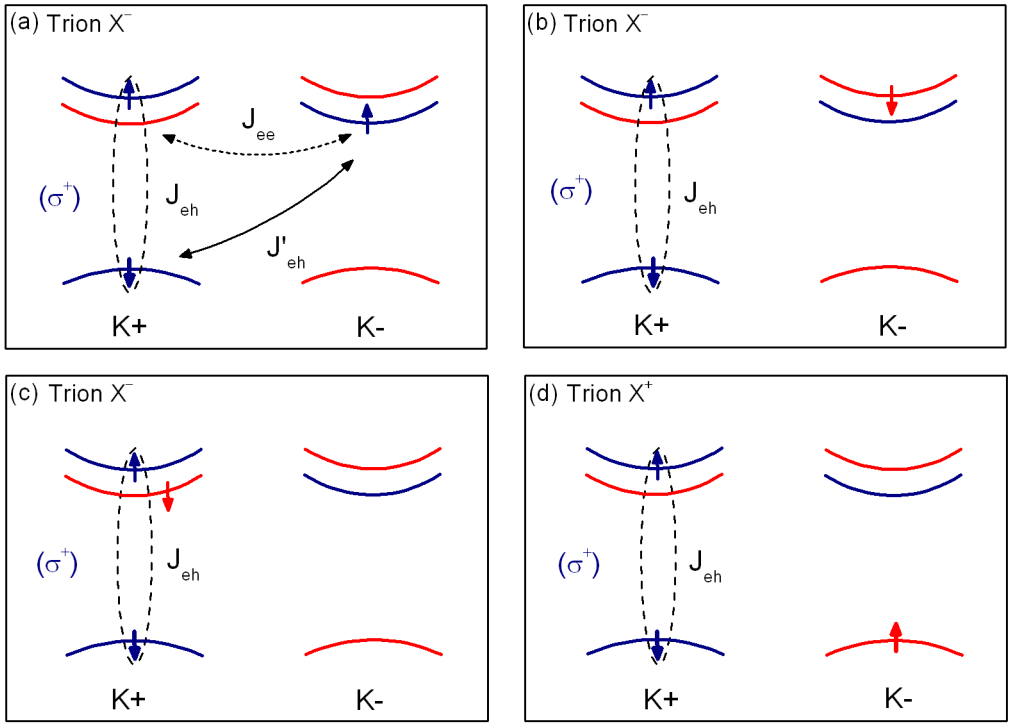

Figure 1.12: Valley charged excitons (trions) configurations in monolayer dichalcogenides. Three configurations (a-c) of the negative charged exciton (X^-) and one configuration (d) for positive charged exciton (X^+). The electron-electron (e-e) exchange interaction is indicated by a black dash-dotted arrow. In all the configurations the polarization of the emitted photon is $\sigma+$.

In the case of charged excitons (trions), the selection rules are illustrated schematically in Fig. 1.12. There are three possible configurations for the negative charged exciton (X^-) (Figs. 1.12(a-c)), and only one for the positive charged exciton (X^+) (Fig. 1.12(d)), since the holes in the valley **K**+ only have to be spin-down states, and holes in the **K**− valley have to be spin-up, due to the large spin-valley coupling. All the other configurations are the time-reversal equivalent of the ones shown in Figure 1.12. Because at the **K**+ valley only spin-down holes populate the valence band maximum, negative charged-excitons are formed by a electron-hole pair with

a spin-down (-up) electron from the conduction band minimum at the other **K**− valley (scenario (a,b) in Fig. 1.12). It is also possible to form a negative charged exciton through a bound electron-hole pair which captures an electron from the other conduction band minimum at the same valley (Fig. 1.12(c)). Upon electron-hole radiative recombination, an electron is left in the CBM and the PL emission polarization is determined by the valley in which the neutral exciton has recombined.

The positive charged exciton can only be formed by an electron-hole pair in a certain valley (**K**+) which captures a hole from the other valley (**K**−), as shown in Fig. 1.12(d). Upon electron-hole recombination, the X^+ becomes $\sigma+$ photon plus a spin-up hole and *vice versa* for their time-reversal configuration.

The formation of a neutral and charged excitons is mainly due to the direct part of the Coulomb interaction. However, there is another known Coulomb contribution, called exchange interaction [Pikus 1971], which leads to a splitting of the exciton energy in semiconductors. Recently, Yu and coworkers have calculated the exchange interaction effect on charged excitons in tungsten dichalcogenides monolayers [Yu 2014a]. Among the four ground state configurations of negative and positive trions illustrated in Fig. 1.12(a-d), the exchange interaction between the excess electron (or hole) and the recombining electron-hole pair is present only for the one shown in Fig. 1.12(a) (and its time-reversal configuration). The exchange energies for the two electrons (e-e) repulsion and electron-hole (e-h) attraction are expressed through the J_{ee} and J'_{eh}. The exchange energy is proportional to the probability of finding the electron-electron or the electron-hole in the same position. Due to the electron-electron Coulomb repulsion, the probability of finding an e-e is much smaller compared to the one of finding an e-h. Therefore, taking into account the calculated distance of the excess electron at opposite valleys from the hole $a_{eh} = 2$ nm, it has been estimated an exchange energy $J'_{eh} \sim 6$ meV [Yu 2014a]. There has been indirect evidences supporting these predictions. Polarization resolved μPL measurements in magnetic field perpendicular to the layer have revealed a different behavior for neutral and charged exciton which has been assigned to a distinct exchange fine structures of X and X^- [Srivastava 2015, Aivazian 2015]. Moreover, the absence of linear polarizations in the PL emission of the negative charged excitons has been explained through the exchange Coulomb interaction [Jones 2013].

Chapter 2

Experimental techniques

Contents

This chapter describes the experimental techniques used during this thesis. It is composed of two sections: in section 2.1, the experimental techniques used to performed measurements in the absence of magnetic field are described: steady-state and time-resolved μPL, as well as μ-Raman. Section 2.2 contains a detailed description of the experimental techniques such as transmission and micro-photoluminescence used in high magnetic field.

2.1 Spectroscopy in the absence of magnetic field

The optical response of two-dimensional crystals provide direct access to its electronic properties. In this thesis a combination of various spectroscopy methods with magnetic field have been used to probe the electronic properties of atomically thin TX_2. In particular, μ-photoluminescence (PL), Raman spectroscopy and optical inter band absorption in the visible spectral range have been used.

Let us start from the description of the experimental techniques used in the absence of external magnetic field. We have performed steady-state and time-resolved μPL measurements, as well as μ-Raman measurements. The experiments have been performed at the Laboratoire National des Champs Magnétiques Intenses (LNCMI), in Toulouse (France). A schematic overview of the setup is presented in Figure 2.1. The setup is composed of two separate geometries: the first one was used to measure steady-state μPL (Setup-STPL) and μ-Raman and it is enclosed by a rectangle with red-dashed line; the second geometry, enclosed by blue-dashed line, was employed for time-resolved μPL (Setup-TRPL) measurements. For both time resolved and steady state measurements, the samples were placed in a helium flow cryostat with optical access, which allowed measurements in the temperature range from 4 to

300K. The cryostat was mounted on motorized x-y translation stages, which allows high resolution spatial mapping. We used free beam optics in a backscattering configuration (see Fig. 2.1). Excitation and collection of the signal from the sample was implemented using a non-polarizing cube beamsplitter and long working distance (7 mm) microscope objective with a numerical aperture $NA = 0.66$ and magnification $50\times$. The typical diameter of the spot on the sample was of the order of $1\mu m^2$. Additionally, the TX_2 flakes deposited on a silicon substrate with lithographic orientation marks were identified *in situ* by illuminating the sample with white light from a halogen lamp which, after being reflected from the sample, was imaged on a small CCD camera. Example of a WS_2 flake image with orientation marks is on the bottom of Fig. 2.1.

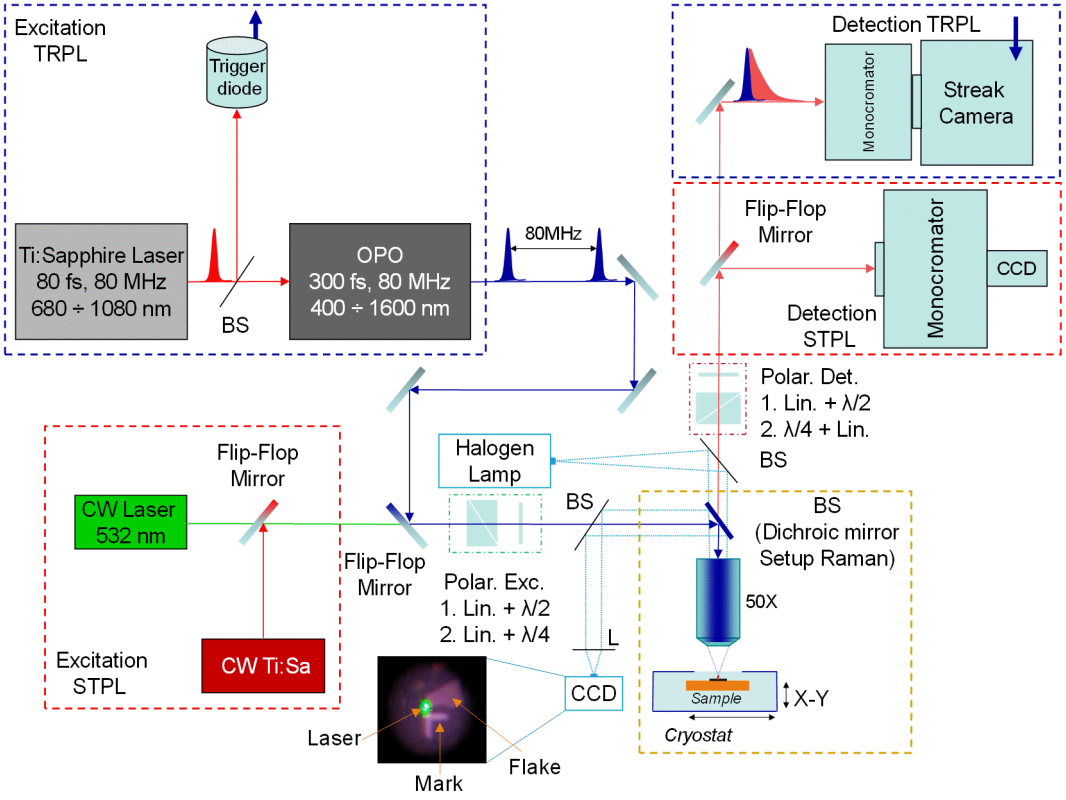

Figure 2.1: Layout of the experimental set up layout at LNCMI-Toulouse. Two different geometries are shown: for steady-state PL (STPL) measurements cw lasers were used for excitation and a CCD in detection; for time-resolved PL (TRPL) - femtosecond laser in excitation and streak camera in detection.

2.1.1 Steady-state μPL and μ-Raman

For the excitation of the steady-state μPL and μ-Raman, a solid-state laser emitting at 532 nm, as well as a tunable Ti:Sapphire were used. The signal from the sample

was dispersed using a spectrometer equipped with a nitrogen-cooled CCD camera. Additionally, for some measurements, the sample was simultaneously illuminated by a tunable Ti:Sapphire laser, with the laser beams entering collinearly to the microscope objective. For μ-Raman measurements, the 520 cm^{-1} phonon mode from the silicon substrate or several known spectral lines of Neon lamp were used for calibration. In addition, we introduce polarization optics in both excitation and detection paths. It is marked in Fig. 2.1 as "Polar. Exc." and "Polar. Det.", respectively. To control the linear polarization in excitation, a Glan-Taylor polarizer together with a $\lambda/2$-plate was used. The axis $\lambda/2$-plate was rotated over 180^0 by a motorized controller. For circular polarization in excitation, a Glan-Taylor polarizer followed by a quarter-wave plate was used (see Fig. 2.1). In detection, the PL linear polarization analysis was performed by a $\lambda/2$-plate followed by the Glan-Taylor polarizer placed in the collimated beam. For circular polarization analysis we used a quarter-wave plate followed by a polarizer. The μPL (μ-Raman) signals corresponding to two different polarizations were stored and analyzed separately.

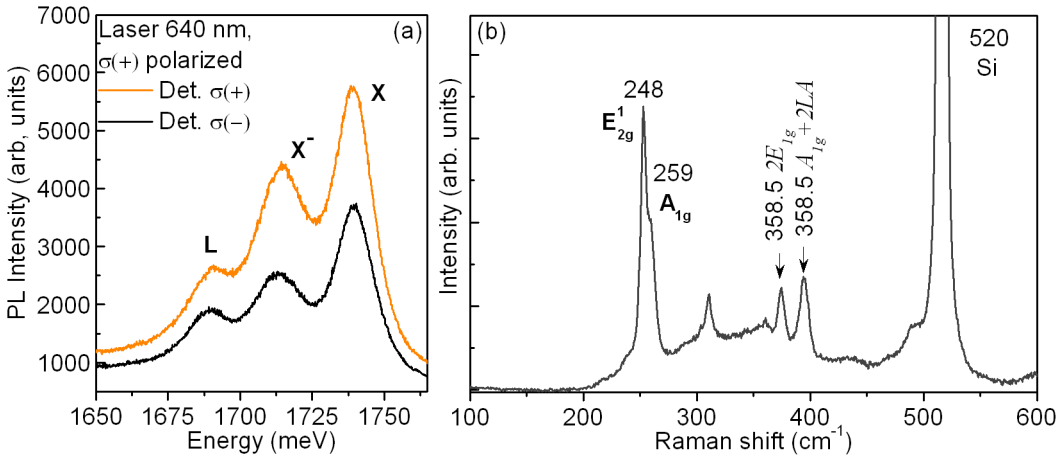

Figure 2.2: (a) and (b) Typical emission μPL spectra and μ-Raman spectrum of WSe_2 monolayer measured at 4K. The PL emission in detection was analyzed by σ^+ (orange line) and σ^- (black line) circular polarization, respectively.

Typical polarization-resolved μPL spectra of WSe_2 monolayer measured at low temperature ($T = 4$K) are presented in Fig. 2.2(a). The excitation was σ^+ polarized and detection was performed for both co-polarized (σ^+) and counter-polarized (σ^-) configurations marked by orange and black lines, respectively. The two highest energy transitions, marked as X and X$^-$, correspond to the recombination of a neutral exciton and charged exciton (trion), respectively.

μ-Raman is used in the identification of the number of layers in the TX_2 samples under investigation. The μ-Raman scattering polarization measurements were performed in the same configuration as μPL. However, the non-polarizing beamsplitter was replaced by a laser-flat dichroic beamsplitter which, together with a ultrasteep

long-pass edge filter, placed in front of the spectrometer, enabled the measurements of Raman spectra up to 30 cm^{-1} from the laser line wavelength. Typical μ-Raman spectrum from a monolayer WSe_2 is depicted in Fig. 2.2(b).

2.1.2 Time-resolved μPL

We now describe the experimental set-up used to measure time-resolved μPL (TRPL). In this experimental geometry, shown in Fig. 2.1 enclosed by blue dashed rectangles, the PL was excited by femtosecond pulses generated by a tunable frequency-doubled optical parametric oscillator (OPO) synchronously pumped by a mode-locked Ti:Sapphire laser. The typical pulse duration and spectral width of the OPO are 300 fs and 3 meV respectively; the repetition rate is 80 MHz. The OPO wavelength can be tuned between 400 and 1600 nm. The Ti:Sap laser used for pumping the OPO has a typical pulse width of 80 fs and a tunable wavelength range between 680 and 1060 nm. For detection we used a Hamamatsu Streak Camera equipped with a synchro-scan unit. The spectral response was dispersed by an imaging spectrometer placed at the entrance of the streak camera.

The streak camera is an ultra high-speed detector which captures light emission phenomena occurring over extremely short time periods. The operating principle of a streak camera is shown in details in Fig. 2.3(a). In the TRPL setup the PL signal that enters the streak camera is already spatially dispersed by the spectrometer. In a simplified picture, several photons distributed in horizontal direction according to their respective energies reach the detector. Also, some delay in time between the photons is introduced. These photons are projected onto the slit and focused by a lens into an optical image on the photocathode. Here, the photons are converted into a stream of electrons proportional to the intensity of the incident light due to the photoelectric effect. The electrons are accelerated along the evacuated tube and pass between a pair of sweep electrodes, where a time-varying voltage is applied to the electrodes, resulting in a high-speed sweep (see Fig. 2.3(b)). As a results, the early part of the pulse is deflected less than the later part of the pulse, so that different parts of the pulse strike the micro channel plate (MCP) at different positions. As the electrons pass the MCP, they are amplified several thousands of times and are then bombarded against the fluorescent phosphorous screen, where they are converted back into light. Then, the image of the screen is acquired with a CCD-camera. In this way, the initial temporal distribution of PL photons is converted to a spatially resolved signal. The brightness of the PL image is proportional to the intensity of the corresponding incident light pulses and the position in the horizontal direction on the phosphor screen corresponds to the wavelength of the incident light. Thus, we obtain a typical 3D image, where on the x-axis we have the photon wavelength, the time dependence is given along the y-axis and the PL intensity is represented by the color plot. Typical results of such measurements is sketched in Fig. 2.3(c) for a monolayer WSe_2 at low temperature. The time-evolution for a particular wavelength or spectrum at a particular delay can be obtained by taking a vertical/horizontal cross-section on the interested region (see Fig. 2.3(c) the white-dashed rectangles).

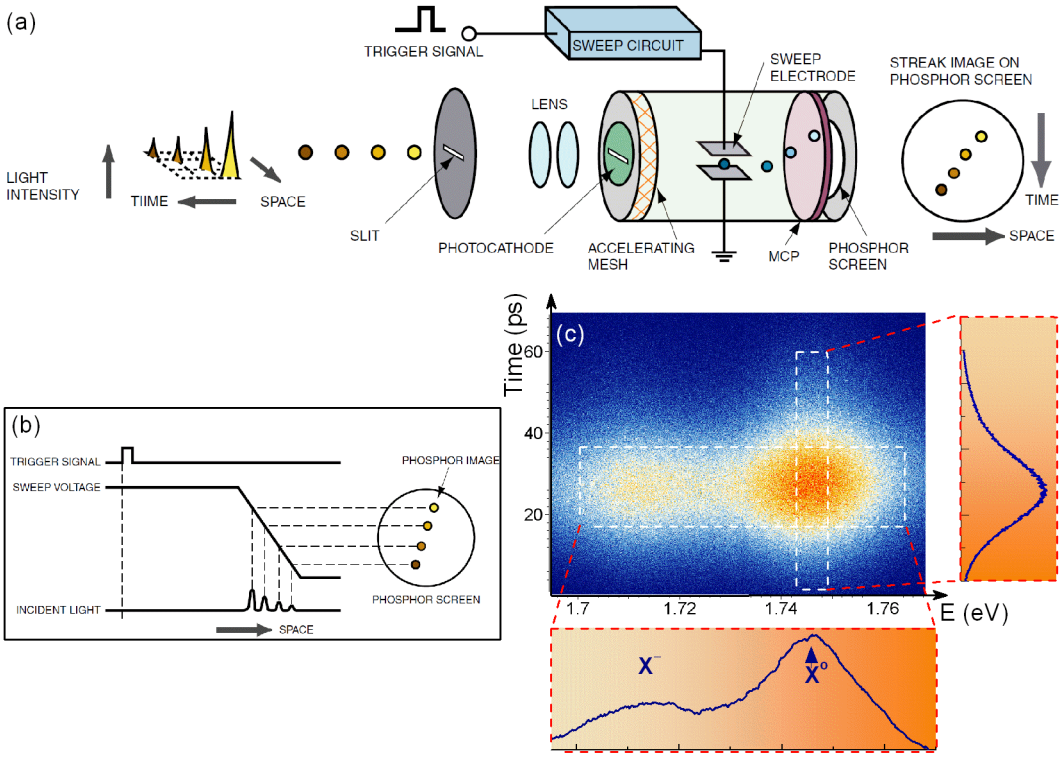

Figure 2.3: (a) and (b) Operating principle and timing of a streak tube. Picture adapted from Hamamatsu Guide to streak cameras. Typical μPL time-resolved image obtained by streak camera of WSe_2 monolayer at $T = 4$K is shown in (c). Vertical cross-section shows the rise- and decay-time of the neutral exciton (red dashed line on the right hand-side). Horizontal cross-section shows the μPL spectrum at a certain delay.

2.2 Spectroscopy in high magnetic field

We now describe the experimental technique used in high magnetic field. Steady-state μPL measurements were performed in High Field Magnetic Laboratory (HFML)-Nijmegen (Netherlands). The transmission measurements were carried out in pulse magnetic fields located at LNCMI-Toulouse (France).

2.2.1 Pulsed magnetic field generation

LNCMI is one of the world leading laboratories which currently produces nondestructive pulsed magnetic field up to 90 T. It has an extensive in-house research activity and serves also as a user facility offering access to high magnetic field installations for external scientists.

The operating principle of the pulse magnetic field generation is based on a discharge of a 14 MJ capacitor bank (Fig. 2.4(a)), and/or of a mobile 6 MJ capacitor

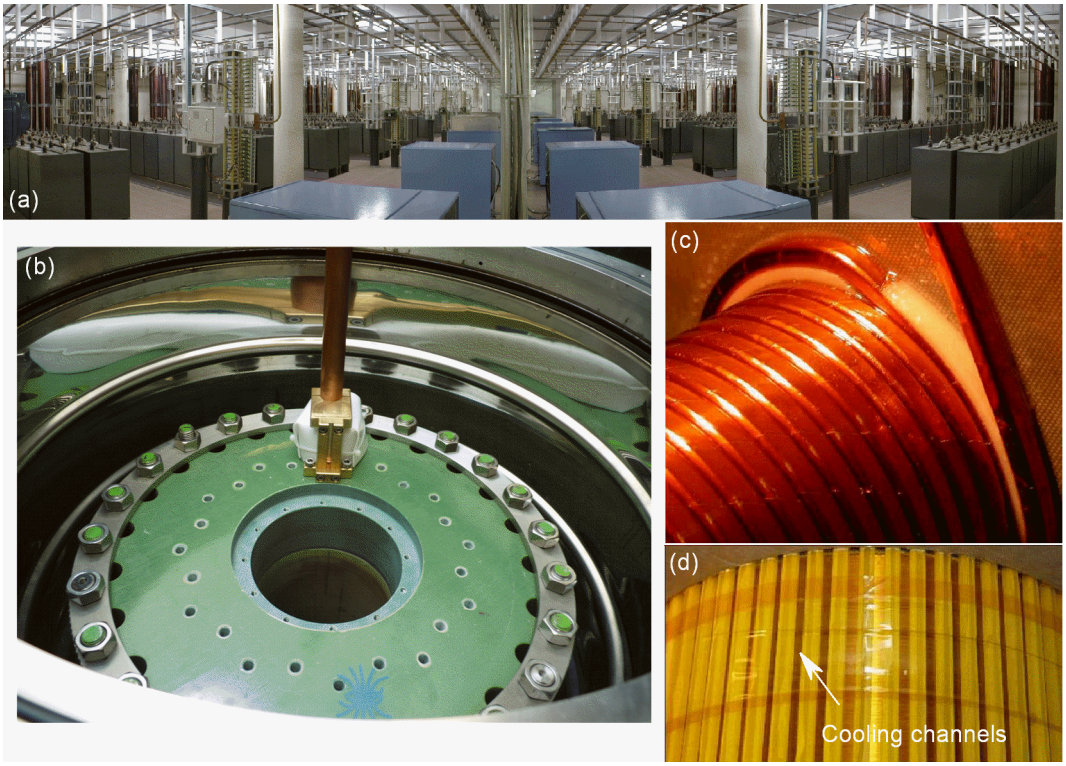

Figure 2.4: (a) 14 MJ capacitor bank at LNCMI-Toulouse; (b) standard resistive coil in a nitrogen cryostat; (c) shows rectangular cross-section copper wires in a coil together with vertical channels (d) for liquid nitrogen circulation.

bank in the case of a dual-coil system, in a home-made resistive coil. A typical coil in a nitrogen cryostat is illustrated in Fig. 2.4(b). The material used for coil fabrication has to combine three important properties: (1) high mechanical resistance; (2) high specific heat; and, (3) low electrical resistance. For this purpose, a rectangular cross-section copper composites reinforced at each layer by Zylon fibers is used as presented in Fig. 2.4(c). In order to avoid a magnet explosion, these properties are optimized by completely immersing the whole magnet in a liquid nitrogen cryostat. The total pulse duration depends on the peak field value and it is of the order of a few 10-s to 100-s of ms. Figure 2.5 summarizes the time profiles for all the magnets used in LNCMI-Toulouse. It can be observed that depending on the magnet bore and required energy, the magnet peak field and pulse duration are different (plotted in various colors). For instance, in a 28 mm magnet bore (violet line) the energy required to generate 55 T is 5 MJ, whereas for a 13 mm bore for generation of 80 T, 6 MJ are required (orange line).

The time between the pulses can vary from a few minutes to several hours depending on the length of the pulse and the peak field; i.e., the energy dissipation. However, a special technique developed in LNCMI allows to reduce the cooling rate

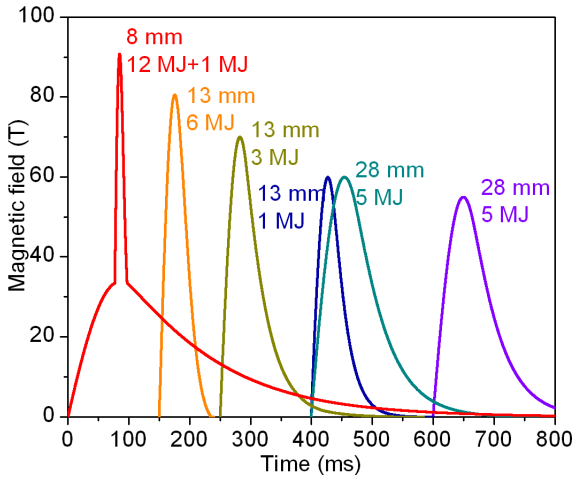

Figure 2.5: Magnetic field profiles as a function of time obtained by different resistive coils. The energy in MJ used for both inner and outer magnets.

by a factor of $\times 3$ using vertical channels inside the coil as shown in Fig. 2.4(d).

All the magneto-transmission measurements presented in this work were performed using 70 T and 90 T magnets, respectively. The 70 T magnet is a single coil based system with an inner bore diameter of 6 mm and pulse duration of 150 ms. The 90 T magnet is a prototype copper/niobium composite dual-coil system, where an outer magnet is energized with a 14 MJ capacitor bank. The inner magnet is energized with the 1.15 MJ mobile capacitor bank or by 3 MJ module of the new 6 MJ capacitor bank. As a result, as it is shown in Fig. 2.5 (red curve), the total magnetic field has a different shape compared to single coil systems: a long background 34 T pulse generated by the outer coil and a short 62 T pulse that, together allow to reach a maximum magnetic field of 90.8 T with pulse duration of 9.5ms. The inner bore diameter at LN_2 temperature (77K) is 7 mm, while at 4K is 4 mm.

2.2.2 Optical transmission in pulsed magnetic field

Optical transmission measurements in pulsed magnetic fields on bulk samples presented in this work were carried out in LNCMI. Magneto-transmission experiments which are performed in pulsed field require a special designed optical setup due to very limited space inside the magnet coil and the pulsed magnetic field environment. Insulating materials were used to avoid heating effects due to eddy currents during the pulse. In Figure 2.6(a) is presented the picture of the magneto-transmission probe used in these experiments. A multimode optical fiber was used to transmit the incident white light provided by a broad-band tungsten-halogen lamp to a sample placed in a cryostat. The technical drawing of the probe main optical elements of the system is sketched in Fig. 2.6(c). Two gold mirrors oriented in a **U** shape are used to reflect the incident white light through the sample into the collecting optical

fiber. In order to collimate the beam in the region of the sample, two lenses **L1** and **L2** were mounted. A quarter-wave plate followed by a linear polarizer were placed after the sample, as shown in Fig. 2.6(c). Thus, only one circular polarization of the transmitted light was allowed to pass through the optical fiber. The transmitted light was analyzed by a spectrometer equipped with a CCD camera placed on a mobile optical table. To detect the opposite circular polarization, the magnetic field direction was inverted. All the transmission measurements presented in this work were performed in a Faraday configuration (where propagation vector of light $\vec{k}$ is parallel to the magnetic field $\vec{B}$). The magnetic field was measured by a pick-up coil mounted close to the sample. The temperature was control by a cernox connected to the head of the probe as is shown as a zoom in Fig. 2.6(b).

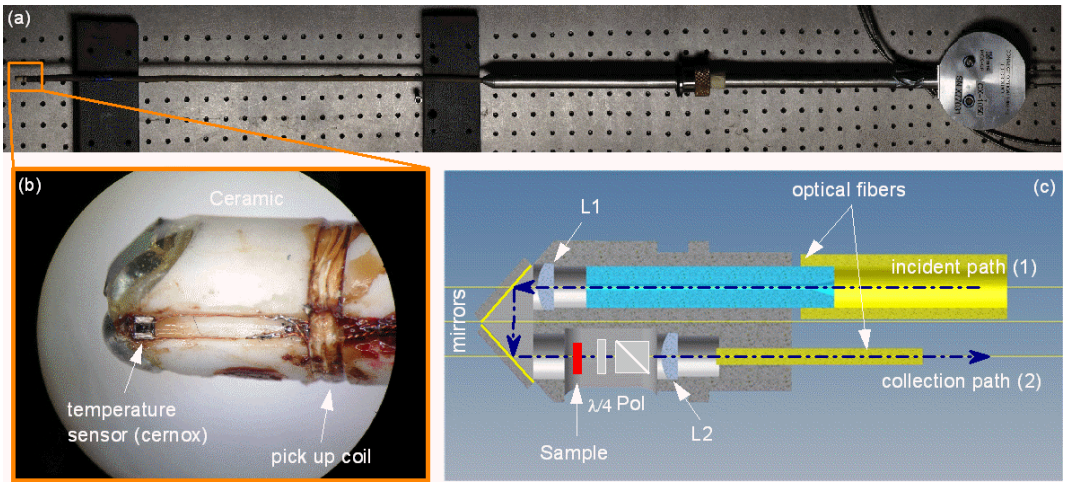

Figure 2.6: (a) Picture of the magneto-transmission probe. Zoom: Part of the probe fabricated from ceramics (b). Technical drawing of the part of probe with optical components (c).

Additionally, we developed a synchronization system to acquire transmission spectra in a very short pulse fields with a precision better than 0.1ms. Figure 2.7 shows the synchronization algorithm used in our magneto-transmission measurements. Because of a very short time scale peak of the magnetic field at 90 T (aproximately 9.5ms), it was crucial to be well synchronized with the maximum of magnetic field. To achieve better synchronization, the CCD detector was used to provide a master trigger. A typical sequence of the events was as follows: (1) first, a pre-trigger signal was send to the detector; (2) subsequently, the CCD sends a series of pulses for multiple acquisitions to a waveform generator and oscilloscope (Hyoki); The waveform generator converts the pulses series into a TTL rise signal, that later is sent to a delay unit. The delay unit is configured to retard the trigger such that the acquisition of the spectrum occurs at the maximum of the field (see inset Fig. 2.8); (3) the shutter sequence of the CCD is recorded by the oscilloscope (on channel 1); (4) after a user define delay, a trigger signal is sent to the capacitor

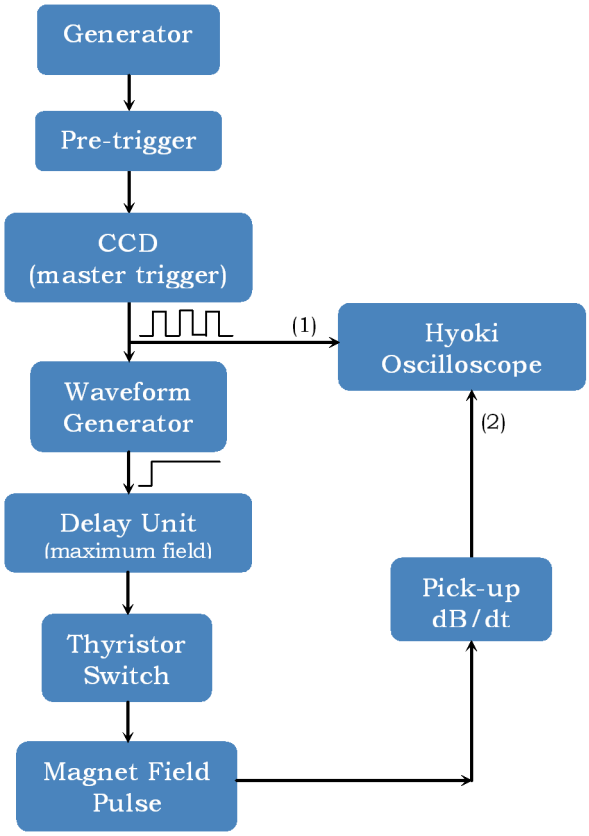

Figure 2.7: Schematic representation of the synchronization sequence in magneto-transmission measurements.

bank; (5) the pulse is detected via a large voltage spike in the pick-up coil placed close to the sample (recorded on channel 2); Later, this signal is integrated in order to calculate the magnetic field as a function of time. Using the recorded sequence on Hyoki oscilloscope and CCD acquisition spectra, every spectra is associated to its corresponding magnetic field value. Usually it was possible to acquire with a single shot a few tens of spectra and therefore, to complete the magnetic field dependence. An example of this is shown in Fig. 2.8 for a series of 40, 2ms acquisitions using a Si CCD. Thus, in a dual-coil system, a complete experiment would consist of a few pulses with different peak fields to have good coverage of the whole magnetic field range from 0 to 90T.

Typical transmission spectra of bulk WSe_2 measured at $T = 77$K are presented in Fig. 2.9 and shows a good signal to noise ratio. The magnetic field induced exciton energy shift can be reliably extracted by fitting a Gaussian to the data.

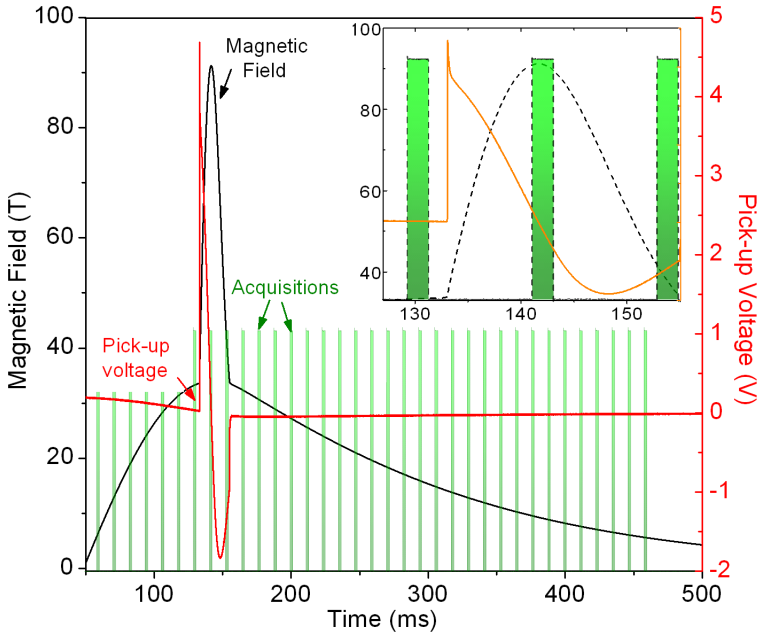

Figure 2.8: Magnetic field (black line) and pick-up voltage (orange line) as a function of time during a 90 T pulse. Green rectangular pulses represent the CCD acquisition time. The inset shows the synchronization of the CCD acquisition with the maximum magnetic field.

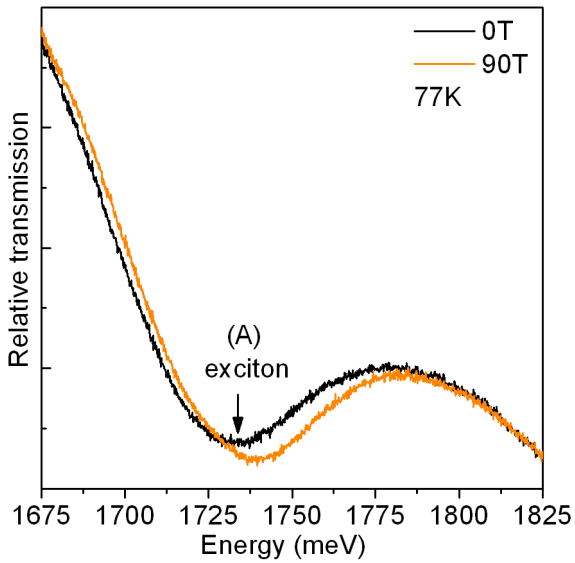

Figure 2.9: Typical magneto-transmission spectra of WSe_2 bulk crystal measured at $T = 77$K.

2.2.3 μPL under dc magnetic field

HMFL is a state of the art dc magnetic field facility with many visitors making their own specific experiments using the 20MW installation that can reach at the moment 37.5 T continuous magnetic field. μPL measurements in dc high magnetic fields (up to 31T) on TX_2 monolayer samples were carried out as a visitor in HFML. For our experiments, the 28 mm diameter probe fitted into a 32 mm, 33 T Florida-Bitter magnet, was entirely free beam, which allowed for full imaging of PL emission on a CCD detector. The probe consisted of a carbon tube, which has the advantage that it is strong, rigid, black (non-reflecting to reduce scattering light) and non-magnetic (Fig. 2.10). At the end of the tube, a special 40× microscope objective from Attocube (laser spot diameter 1μm) was mounted for μPL measurements on micrometer size samples. Because of the free-beam design it was possible to independently control the excitation and detection light, which allows for detecting PL emission as a function of the position relative to the laser excitation spot (imaging).

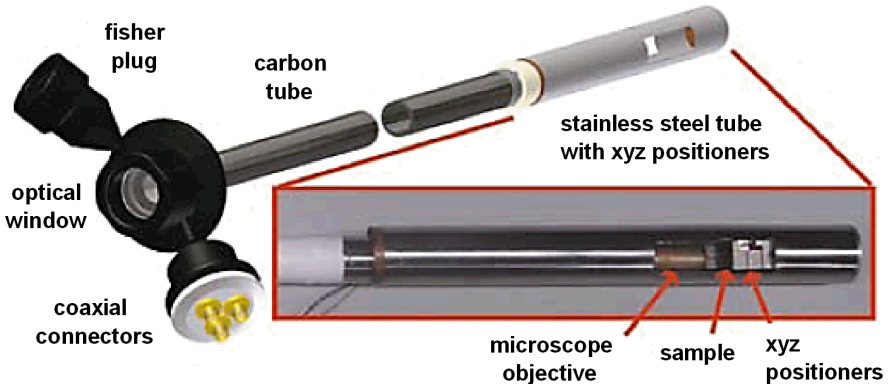

Figure 2.10: Optical insert for μPL imaging in HMFL-Nijmgen.

For the μPL measurements, the Si substrate on which the flakes are deposited were placed on x-y-z piezo stages (from Attocube Company). This allowed the recording of PL emission from the sample in x-y plane and regulating the distance from the objective (focus) in z direction as it is shown in Fig. 2.10 (red-rectangle). Both the excitation and collected light were transmitted through a non polarizing cube beam splitter (50:50) placed on the optical axis of the objective. However, due to the increased optical path lengths of aproximately 20 m, it was difficult to localize *in situ* an individual flake which is a few microns by a few microns size. We performed high magnetic fields measurements using circular excitation light, circular detection and their combination to investigate TX_2 monolayer flakes.

Typical polarization-resolved magneto-PL spectra of mechanically exfoliated WSe_2 monolayer measured at $T = 4$K are presented in Fig. 2.11. The direction of the magnetic field was the same for all measurements. However, the polarization control of excitation and detection was done using a liquid crystal retarder calibrated at half and quarter wavelength retardance at neutral exciton (X) and trion (X^-) located

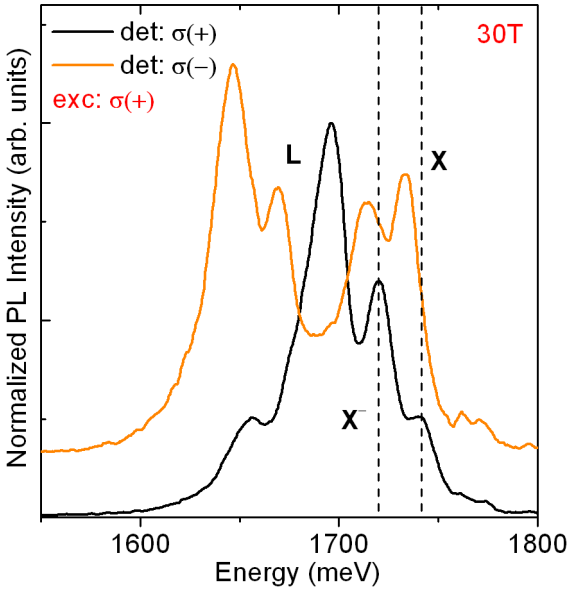

Figure 2.11: Typical low temperature μPL spectra of WSe_2 monolayer excited with σ^+ polarization in 30 T. The PL emission in detection was analyzed by σ^+ (black line) and σ^- (orange line) circular polarization, respectively. The spectra are shifted vertically for clarity.

outside the cryostat. Magnetic field up to 30 T was applied in a Faraday configuration. At 30 T magnetic field, we observe significant change in the PL spectrum recorded in co-polarized (σ^+) and counter-polarized (σ^-) configurations.

Chapter 3

Description and characterization of the samples

Contents

This chapter describes the samples used during this thesis and their characterization. The growth of the single crystals of TX_2 followed by the description of the mechanical exfoliation method used to obtain atomically thin crystals are presented in section 3.1. Section 3.2 contains a detailed characterization of the samples by the various experimental techniques used throughout this work, such as optical microscopy, atomic force microscopy (AFM), micro-Raman and micro-photoluminescence spectroscopy.

3.1 Technological preparation

Several samples of the atomically thin layered transition metal dichalcogenides 2H-WS_2 and 2H-WSe_2 have been investigated in this work. The bulk crystals were grown by the vapor transport method using Br_2 or Cl_2 molecules as a transport agent. Atomically thin layers were subsequently obtained by micromechanical exfoliation.

3.1.1 Single crystal growth

Based on the phase transformation process, single crystal growth techniques are classified as solid growth, vapour growth, melt growth and solution growth [Pamplin 1979]. Among them, the chemical vapor transport (CVT) technique is widely used for the transition metal dichalcogenides semiconductor class of materials. A general feature

of this method is that a *transport agent* (volatile substance), in most cases halogen molecules, is added to the nonvolatile starting mixture needed to transform the latter into a suitable molecular species which can diffuse elsewhere to be deposited in the form of *crystals*. The deposition and crystallization take place if different external conditions for the chemical equilibrium are created. Typically, a temperature gradient ($T_2 > T_1$) is used (see Fig. 3.1). The region with the higher temperature (T_2) is called the *charge zone*, whereas the lower temperature ampoule region (T_1) - the *growth zone*.

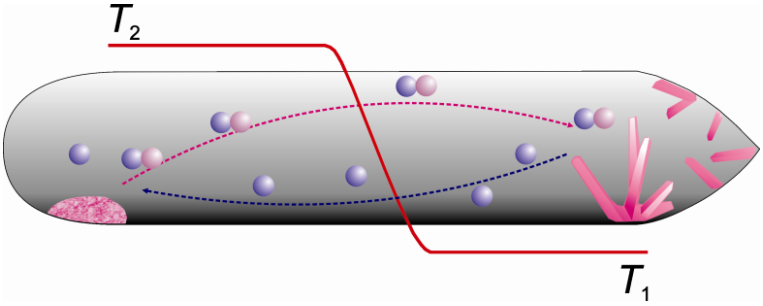

Figure 3.1: Scheme of CVT experiments for crystallization of solids in a temperature gradient. The left hand-side of the ampoule corresponds to the charge zone, while the right hand-side corresponds to growth zone. The red line depicts the temperature gradient with $T_2 > T_1$. After Schmidt et al. [Schmidt 2013].

Our synthetic tungsten disulfide (WS_2) and diselenide (WSe_2) single crystals were grown by CVT at the Institute of Applied Physics (IAP) from Moldova, using the experimental set up depicted in Fig. 3.2. As a starting materials, W and S/Se were used. The chemical elements were allowed to react in an evacuated sealed quartz ampoule of 8 mm inner diameter and 120 mm length in order to exclude the increase of the amount of material transported per unit time throughout the growth. The tubes were slowly heated up to the synthesis temperature of 1000°C for two days and maintained under these conditions for two days more. Halogen molecules were used as a transport agent in the concentration of 5 mg/cm^3. Subsequently, the ampoules with the polycrystalline material were placed in the two-zone tube furnace provided with the appropriate temperature profile. Depending on the TX_2 system, the crystallization chamber temperature at the charge zone and growth zone was set at values according to references [Wildervanck 1970, Lieth 1977]. The ampoules were hold inside the furnaces for a period of up to 6 days, after which they were slowly cooled to room temperature.

The temperature inside the tube furnace was precisely controlled in order to prevent oscillations of the temperature. For this purposes, two manually furnaces (manufactured in-house) with a +/- 0.1°C control precision of the temperature were used. The main parts of the two-zone tube furnace, as shown in Fig. 3.2, are:

- *two thermocouples* - one for each of two temperature zones, usually of type B (platinum -platinum/rhodium), which are in direct contact with the furnace tube

measuring the inside temperature;

- *proportional-integral-derivative* (PID) - automatic digital controller which collects the temperature information from the two temperature zone thermocouples and, using a PID algorithm, adjusts the output power in order to achieve the input temperature set point.

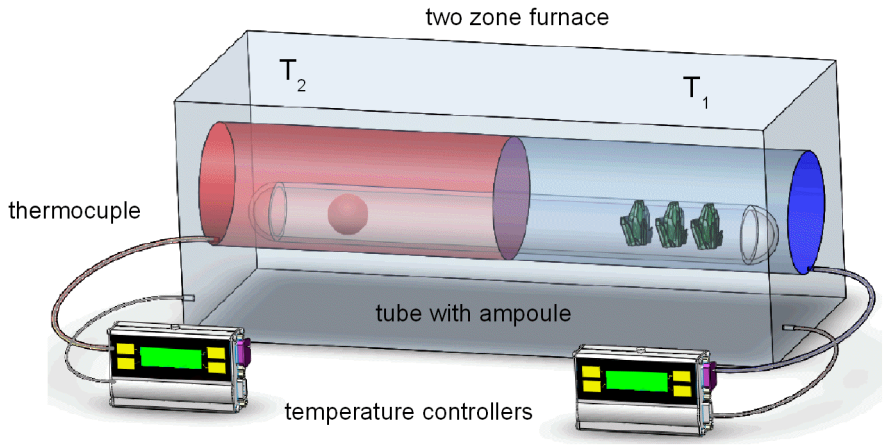

Figure 3.2: Experimental set up for chemical vapor transport in a conventional two-zone furnace.

Due to the weak interacting van der Waals forces existing between the monolayers of the single crystals, the samples were easily cleaved to obtain smooth and clean surfaces. In this way, no chemical etching or mechanical polishing was required. The thickness of each crystal was of the order of a few tens of micrometers with diameters varying from 1 to 3 mm. The obtained chlorine-transported crystals were very thin compared to the bromine-transported crystals. The WS_2 and WSe_2 single crystals had respectively bright blueish and greenish reflective metal look to them.

3.1.2 Mechanical exfoliation

Atomically thin crystals were fabricated from bulk TX_2 crystals using micromechanical cleavage method [Novoselov 2005]. This simple and inexpensive process allows to produce atomically thin layers TX_2 with high quality and with sizes up to several μm. An additional advantage of the exfoliation technique is that the flakes can be easily transferred onto different substrates.

As previously employed for other layered crystals [Novoselov 2005, Wang 2012, Alem 2009, Mak 2010, Li 2013, Ruppert 2014], the surface of the scotch containing bulk crystals was pressed against another clean scotch part and rapidly peeled off to re-cleave the crystals. This procedure was repeated several times until only faint atomically thin flakes were observed on the surface of the scotch by optical microscopy. As a final step, the thin crystals were transferred to an oxidized silicon

wafer (300 nm thick oxide) by slightly pressing the scotch against the wafer surface and subsequently peeling it off slowly. The 300 nm width of SiO_2 layer allows a direct observation of the semiconductor flakes using an optical microscope. The WSe_2 atomically thin samples studied in this work were obtained in the clean room at Laboratory for Analysis and Architecture of Systems (LAAS-Toulouse) with the help of Dr. G. Deligeorgis and the WS_2 samples at LNCMI-Toulouse with the help of Dr. W. Escoffier.

3.2 Samples characterization

To facilitate the localization and identification of the flakes, alphanumeric marks on the substrates fabricated by optical lithography were used. Inspection of the samples under an optical microscope permits a rapid identification of the flakes and their size. In our case, the obtained flakes with thicknesses below 40 nm were several microns large. Selected TX_2 flakes were further analyzed by AFM and μ-Raman spectroscopy.

3.2.1 Optical microscopy

Typical images of the TX_2 exfoliated samples are presented in Fig. 3.3(a) and (b). We used a Nikon Eclipse LV100 optical microscope under normal incidence with different magnification objectives and with a digital camera attached to the microscope trinocular. An *in situ* identification of the flakes was possible due to the lithographic orientation marks fabricated on the substrate.

The silicon substrate appears brown and defines the background, the WS_2 layers appear from yellow, light blue and finally dark blue as the number of number of layers decreases. A monolayer has a characteristic dark blue color in the optical microscope image. Therefore, it was possible to obtain a fairly reliable indication of the thickness of the flakes from the colour. The colour changes due to an interference effect owing to the presence of the thin silicon oxide layer which makes their color thickness dependent under white light illumination (this effect is usually referred as interference color) which can be better seen in Fig. 3.3(b). For an exact identification of the number of layers the actual height of the TX_2 flakes has to be measured, for instance by means of an atomic force microscope.

3.2.2 Atomic force microscopy

The TX_2 flakes selected by optical microscopy were further characterized by AFM. A Nano-R AFM (Pacific Nanotechnology) was operated in contact mode under ambient conditions. In order to avoid artifacts in the determination of the flake thickness, we selected contact mode instead of dynamic modes of operation. The piezoelectric actuators of the AFM have been calibrated by means of a recently developed calibration method to provide a determination of the flake thickness as accurately as possible. Typical AFM color coded image taken on WS_2 flake is

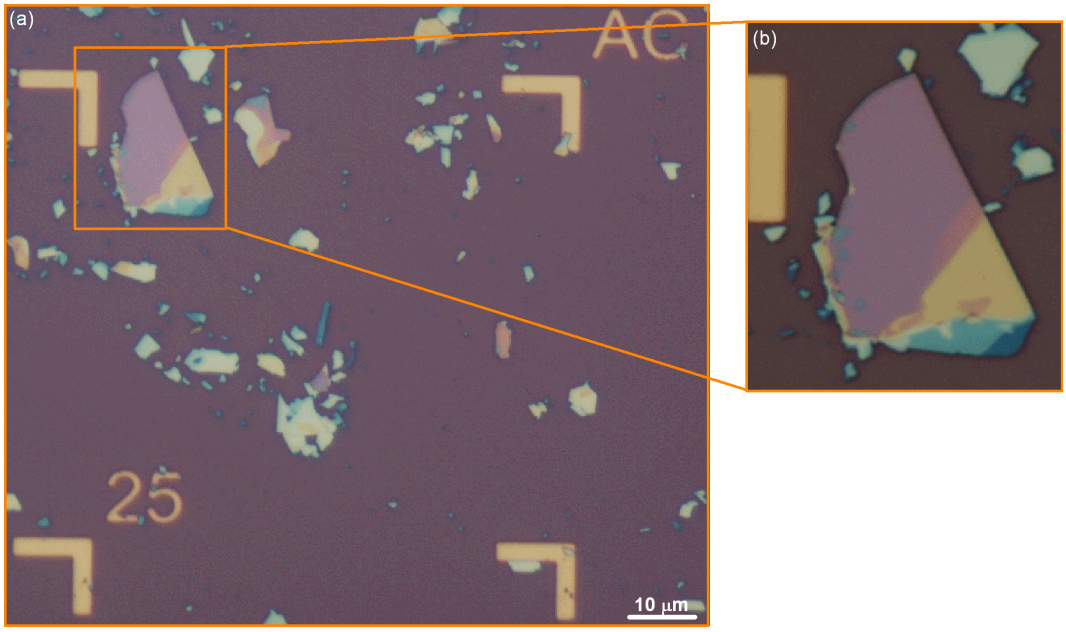

Figure 3.3: Optical microscope image of WS_2 flakes on Si/SiO_2 substrate taken with low magnification (a). Zoom: WS_2 flake with different number of layers regions (b). The alpha-numeric marks in gold color are used to localize the flake.

depicted in Fig. 3.4(a). Different colors correspond to the particular height of the flake. In order to determine the thickness of the flake the AFM height profile, measured moving along the blue line indicated on the AFM color image was analyzed (see Fig. 3.4(b)).

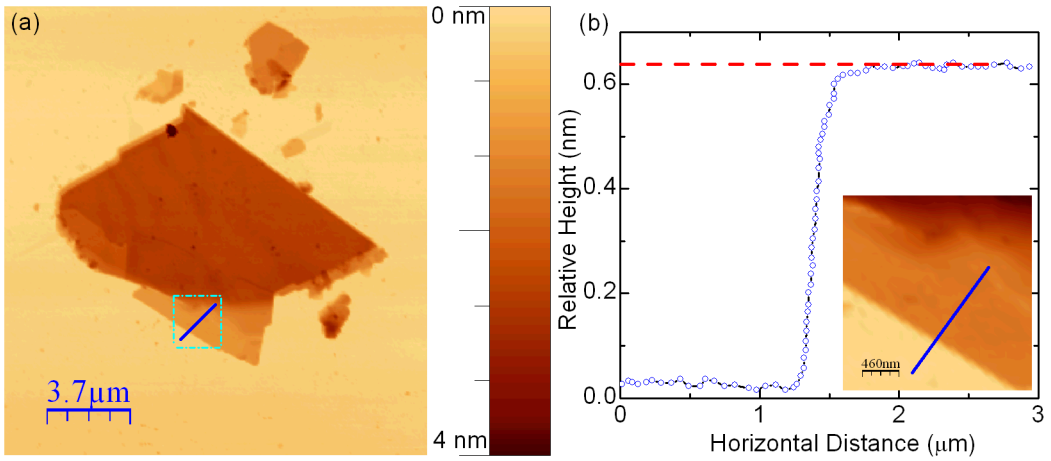

Figure 3.4: (a) AFM color coded image of the WS_2 flake and (b) AFM hight profile measured moving along the green line.

The 0.6 nm step in the AFM height profile observed in Fig. 3.4(b) corresponds to a monolayer WS_2 [Schutte 1987]. The spacing between the monolayer and the substrate determined by AFM (not shown) varies significantly in different measurements and presumably reflects changes in the tip-surface interaction between the substrate and the sample and possibly the presence of adsorbates under the sample. The measured interlayer separation lies in the range of 0.6-0.65 nm, which is consistent, within experimental uncertainty, with the bulk layer spacing of 6.982 ± 0.002 Å reported in the literature [Schutte 1987].

3.2.3 μ-Raman spectroscopy

Raman spectroscopy can be considered as an alternative, complementary, reliable and non-destructive technique to identify the number of TX_2 layers. Indeed, Raman spectroscopy has been successfully employed to characterize the thickness of several atomically thin materials such as graphene [Graf 2007, Ferrari 2006] and other 2D materials [Mak 2010, Korn 2011]. In this work, μRaman spectroscopy was used as a *in situ* tool in order to verify the monolayer character of the sample. The μ-Raman spectroscopy measurements for our samples were performed using an optical cryostat and microscope objective.

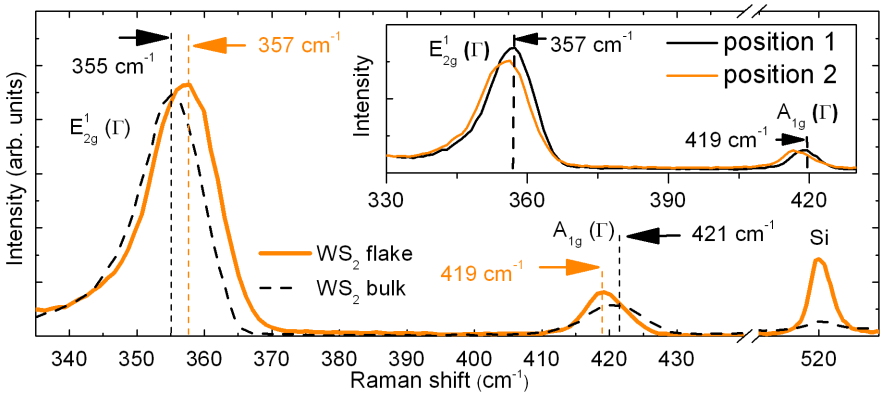

Figure 3.5: Raman spectra measured at $T = 300$K on monolayer (orange line) and bulk WS_2 (black dashed line). The inset shows the strain induced shift of Raman spectra taken at two different positions on the single-layer area of WS_2 flake.

Representative Raman spectra, obtained for WS_2 flake, are shown in Fig. 3.5. Raman measurements performed on the monolayer region of flake (orange line) and measured on a bulk crystal (black dashed line) are shown for comparison. In the spectrum for the bulk crystal we observe two Raman peaks at 355 cm^{-1} and 421 cm^{-1}. They corresponds to the well known active Raman modes E^1_{2g} and A_{1g}. In the spectra measured for monolayer these two peaks shift towards each other by 2 cm^{-1}. As a result the distance between Raman peaks is 62 cm^{-1} in comparison to 66 cm^{-1} observed in bulk. These results are consistent with previously

reported theoretical calculations and measurements on monolayer of tungsten disulfide [Albe 2002, Gutiérrez 2013, Zhao 2013].

Similar measurements were performed on WSe_2 samples. Hence, independently of the AFM measurements, the μ-Raman spectroscopy data provides an additional confirmation of the monolayer character of the investigated regions of our flakes.

3.2.4 μPL spectroscopy

A monolayer of TX_2 group of materials is found to exhibit an enhanced PL compared to thicker layered crystals [Splendiani 2010, Gutiérrez 2013, Zhao 2013]. Similarly, in our samples the PL emission from a monolayer region of a flake, previously confirmed by AFM and Raman measurements, was stronger compared to the emission from multi-layer regions. With experience, the PL spectroscopy can also be used as a technique to identify the number of layers in TX_2 flakes. In this work, the μPL spectroscopy measurements were carried out using the optical cryostat equipped with a microscope objective as described in section 2.1. The spatial resolution of the μPL system is 1 μm.

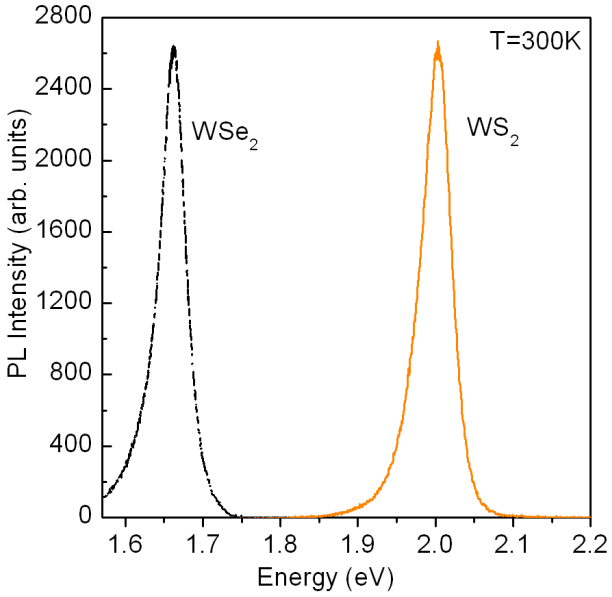

Figure 3.6: Typical μPL spectra measured at $T = 300$K on the monolayer WSe_2 (black dashed line) and WS_2 (orange line).

Typical μPL spectra measured at room temperature of a WS_2 and WSe_2 monolayer are shown in Figure 3.6. Due to the strong confinement, the monolayer PL spectra exhibit an intense emission peak, with the maximum emission at 2.05 eV and 1.67 eV for WS_2 and WSe_2, respectively. The spectral width (full width at half-maximum, fwhm) of the A exciton emission is aproximately 50 meV in WS_2 monolayer, while in WSe_2 is somewhat narrower at aproximately 40 meV. The strong

PL intensity, together with the position of the energy peak, can be used as a complementary and unambiguous evidence of a monolayer region in our samples. We note that we observe a small change in the emission PL maxima with changing the position of the laser spot on the sample. Typically this change is accompanied by a small rigid shift of the two Raman peaks (A_{1g} and E^1_{2g}), but with no change in the peak separation ($\omega(A_{1g}) - \omega(E^1_{2g})$). This suggests that the difference in PL maxima may be attributed to strain [see inset of Fig. 3.5]. This is consistent with the reported influence of the strain on the optical properties of a monolayer of MoS_2 [Conley 2013, Rice 2013].

Chapter 4

Optical properties of monolayer WS_2 and WSe_2

Contents

*In this chapter, the results of micro-photoluminescence measurements performed on monolayers dichalcogenides, in particular WS_2 and WSe_2, are presented. The low temperature μPL spectra show a direct gap emission of both neutral and charged excitons. We demonstrate that the ratio between the trion and exciton emission can be tuned by varying the power of the laser used for excitation of the μPL. Moreover, the intensity of the trion emission can be independently tuned using additional sub band gap illumination. The findings provide an alternative method to manipulate the carrier density and exciton charge state in monolayer dichalcogenides. Finally, the results of the polarization and temperature dependence of μPL on WS_2 and WSe_2 atomically thin crystals are discussed. The content of this chapter has been partially published in Physical Review B **88**, 245403 (2013).*

4.1 Introduction

Monolayer transition metal dichalcogenides with a direct bandgap offer unprecedented opportunities to explore semiconductor optics in the 2D limit. The elementary quasiparticle that plays a key role in optoelectronic phenomena is the exciton,

a bound electron and hole pair with an energy spectrum similar to that of a hydrogen atom. In doped semiconductors, a neutral exciton can bind an additional electron or hole to form a charged exciton (trion), a three-body ground state. Using gate-dependent photoluminescence, [Mak 2013, Jones 2013] have shown the evolution from positively charged, to neutral, and then negatively charged excitons as a function of the density and nature of excess carriers in molybdenum dichalcogenide monolayers. However, trion emission is not usually observed in exfoliated samples unless a gate is used. In this chapter we report trion emission in *ungated* dichalcogenides monolayer using the excitation power to tune the charge state of the exciton. We carried out our investigation on both WSe_2 and WS_2 monolayers, and we find that in WSe_2 the trion emission generally is more pronounced. Very recently, a solution-based chemical doping technique has been used to tune the carrier density in monolayer tungsten dichalcogenides [Mouri 2013, Peimyoo 2014]. At the time of writing this manuscript a similar trion emission has been reported in *ungated* monolayer WSe_2 by several groups [Srivastava 2015, Wang 2014, Shang 2015].

Here, we show that in a monolayer of WS_2 and WSe_2 obtained by the exfoliation of n-type bulk crystals, both charged and neutral exciton recombination in the PL emission spectra are observed. The excitation power, temperature and polarization analysis of WS_2 and WSe_2 monolayers emission is used to investigate the character of PL peaks. Moreover, by simply changing the intensity of the laser excitation, we can tune the ratio between the trion and exciton emission which demonstrates our ability to tune the density of 2D carriers with light. In addition, using additional sub band gap laser excitation, the trion emission intensity can be independently tuned.

4.2 μPL properties of monolayer WS_2

Typical μPL spectra measured on a monolayer region of WS_2 and WSe_2 flakes at $T = 4$ K are presented in Fig. 4.1. The PL spectra are very similar to the emission previously reported for this system [Jones 2013, Srivastava 2015]. In both materials, we observe several PL emission lines. The strong PL emission peaks (X) at around 2 eV in Fig. 4.1(a), and at 1.7 eV in Fig. 4.1(b), correspond well to the predicted recombination of the neutral A exciton across the direct gap of monolayer WS_2 and WSe_2, respectively [Klein 2001, Zhao 2013][1]. The emission energy can slightly change from flake to flake due to the strain, as shown in Refs. [Conley 2013, Rice 2013]. The second emission line (marked as X^-) on the low energy side of the neutral exciton emission corresponds well to a charge exciton (trion), as has been reported in Refs. [Mak 2013, Ross 2013, Mouri 2013, Peimyoo 2014]. Considering the commonly observed residual n-type doping in our samples, the trion charge is most likely to be negative, as assumed for the discussion below. It is important to note, that the clear separation by $\simeq 20$ meV of the charged and neutral exciton, as well as the

[1] Hereafter, the notation "X" we use to refer to the neutral exciton A and "X^-" to the charged exciton.

small full width at half maximum (FWHM) of approximately 15 meV, is a clear advantage compared to the MoS_2 monolayers for the independent investigation of the excitonic states [Mak 2013]. The emission peaks (L) observed below the charged exciton emission in WSe_2 spectra, disappear with increasing the temperature, and are ascribed to localized exciton complexes [Jones 2013, Wang 2014].

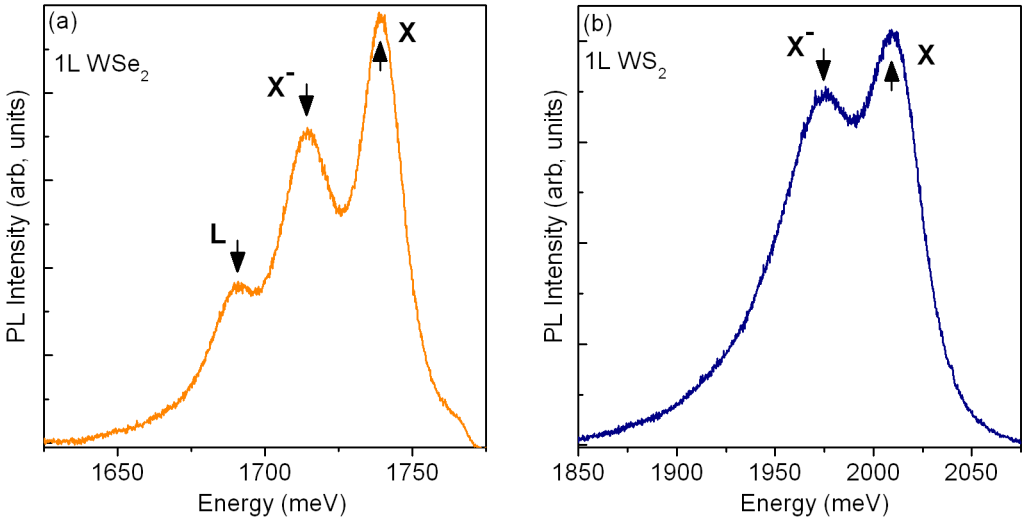

Figure 4.1: (a) and (b) Typical μPL spectra measured at low temperature ($T = 4$K) of WSe_2 and WS_2 monolayer, respectively.

4.2.1 Optical manipulation of exciton charge state

In Fig. 4.2 (a) and (b) are shown typical low temperature μPL spectra measured on two different flakes as a function of the excitation power. In both cases, at low excitation powers, we observe a neutral exciton (X) emission. However, as the excitation power increases the second emission line (corresponding to X^-) on the low energy side of the neutral exciton emission at around 1980 meV becomes much stronger. The PL spectra presented in Fig. 4.2 has been fitted using two gaussian functions to extract the integrated intensity and position of the two excitonic resonances. An example of a fitting procedure for flake 2 and excitation power 0.1 mW is shown in Fig. 4.2(c). The results of such an analysis performed on flake 1 and 2 are presented in Figs. 4.3 and 4.4.

Figure 4.3(a) shows the power dependence of the emission energy of the trion (E_{X^-}) and the exciton (E_X) for both flakes. The symbols indicate the emission energy for the recombination of a neutral and charged excitons. With increasing excitation power the neutral and charged exciton emission red shifts with a larger decrease observed for the trion. We have calculated the difference $\Delta E = E_X - E_{X^-}$ which corresponds to the dissociation energy of the trion. The evolution of the dissociation energy ΔE as a function of excitation power is presented in Fig. 4.3(b).

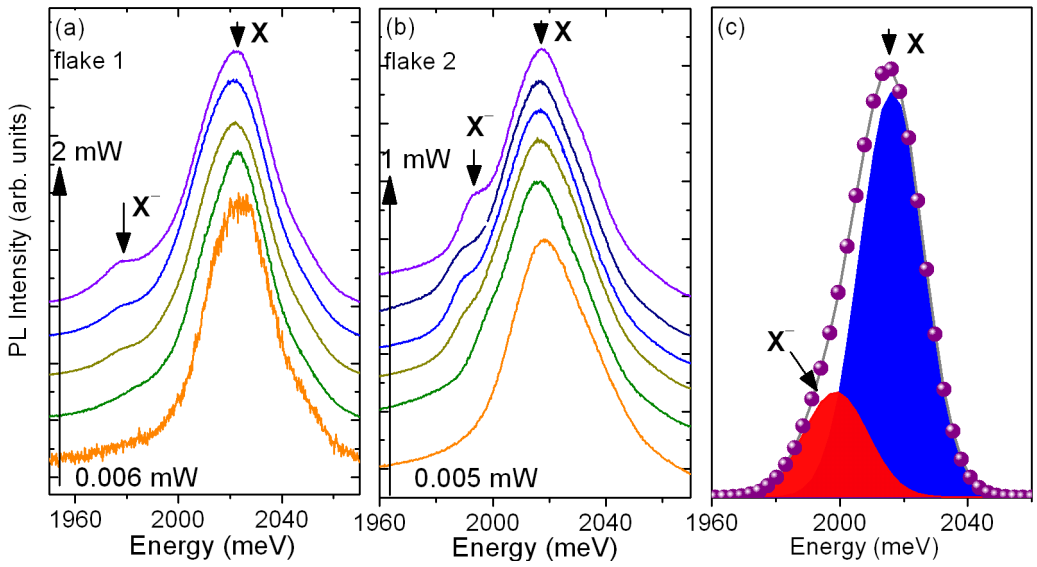

Figure 4.2: (a) and (b) Typical μPL spectra measured with 532 nm excitation power at 4K for WS_2 monolayer. Spectra are offset vertically for clarity. (c) Example of Gaussian fitting of the two excitonic resonances.

The symbols corresponds to the dissociation energy of the X^- measured on flakes 1 and 2. The data is well fitted by a linear dependence (solid line in Fig. 4.3(b)).

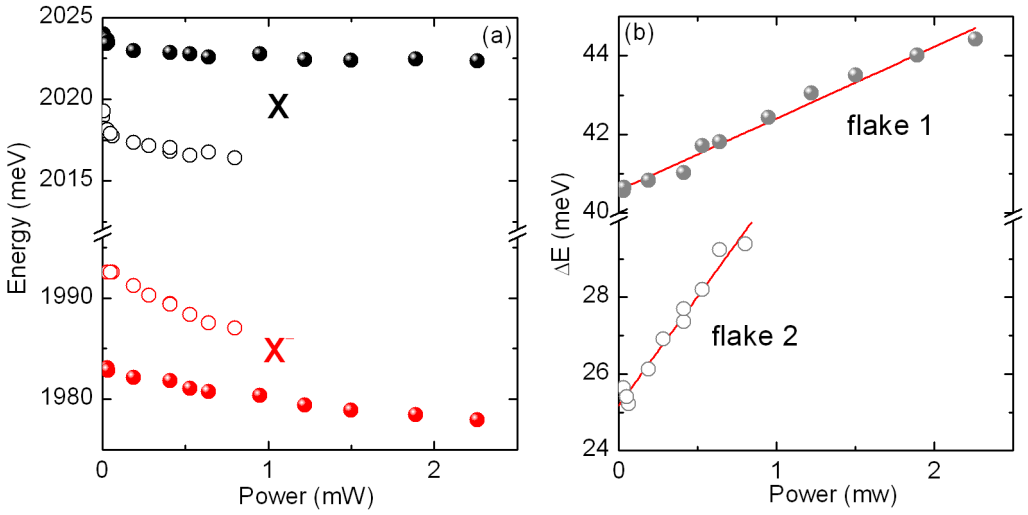

Figure 4.3: (a) The emission energy of the charged and the neutral exciton and dissociation energy (b) as a function of excitation power for WS_2 monolayer. Data is shown for flake 1 (closed symbols) and flake 2 (open symbols). The lines show the results of a linear fit.

The fact that the trion dissociation energy grows linearly with the excitation power suggesting that the density of the carriers also grows linearly with the laser power; the difference in the energy can be expresses as sum of the binding energy of the trion and Fermi energy ($E_{X^-} + E_F$) [Huard 2000]. Here the binding energy of the trion is defined as the dissociation energy in the limit of infinitively small doping ($E_F = 0$) where E_{X^-} is the energy needed to promote one electron from the trion to the bottom of the conduction band. The Fermi energy increases with increasing power of illumination (photon flux). The trion dissociation energy (Fermi energy) increases more rapidly with laser power in flake 2 due to a larger density of free carriers in this sample. As the excitation power increases, the trion dissociation energy increases and we can tune it over approximately 4 meV for both flakes. Similar behavior was also observed in II-VI QWs where the interplay between exciton and charged exciton was also achieved using external illumination of the sample [Kossacki 1999, Kossacki 2004]. The enhanced trion binding energy in dichalcogenides, compared to standard semiconductors, is a consequence of the true 2D nature of dichalcogenides, the greatly enhanced Coulomb interactions arising from reduced dielectric screening, and the larger effective mass [Ramasubramaniam 2012, Chernikov 2014].

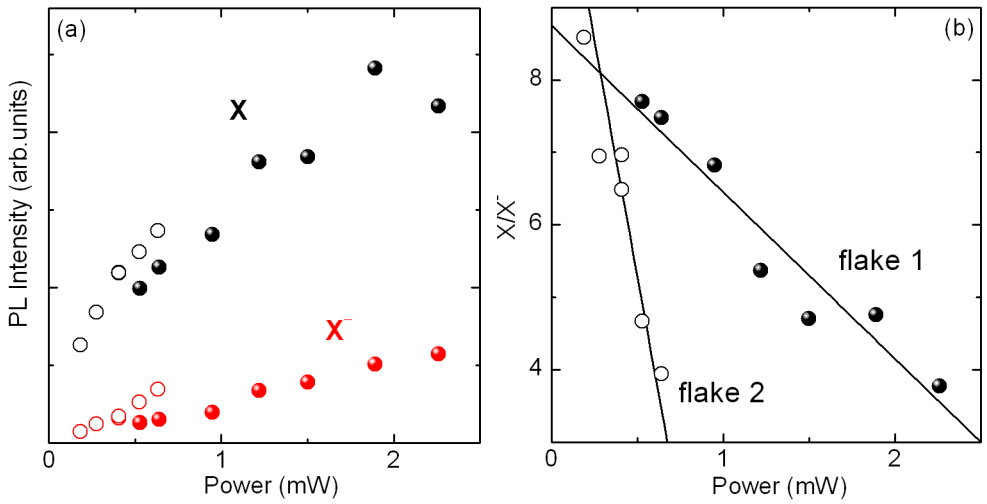

Figure 4.4: (a) Integrated intensity of the charged and the neutral exciton and their ratio (b) as a function of excitation power for WS_2 monolayer. Data is shown for flake 1 (closed symbols) and flake 2 (open symbols). The lines show the results of a linear fit.

The integrated intensity of the emission of the charged and neutral exciton as a function of excitation power, is presented in Fig. 4.4(a). For both excitonic lines the emission intensity increases with increasing power. However, the increase is not the same for the neutral and the charged exciton. To illustrate this the exciton/trion intensity ratio is plotted as a function of laser power in Fig. 4.4(b) for flakes 1 and 2.

For both flakes the ratio of the integrated intensities decreases with the excitation power by a factor of more than 2. This is due to probability of the formation of a trion with increasing excitation power. A detailed description of the physical mechanism will be given below. However, as the above gap green laser illumination also creates electron hole pairs, the intensity of the neutral exciton emission also increases with laser power. The decrease of the intensity ratio is much faster for the second flake as can also seen directly in the spectra in Fig 4.2 (b), where the trion line is rapidly becoming stronger with increasing excitation power. Note, that for both flakes we remain in the linear regime for the trion emission (the exciton emission shows some signs of saturation).

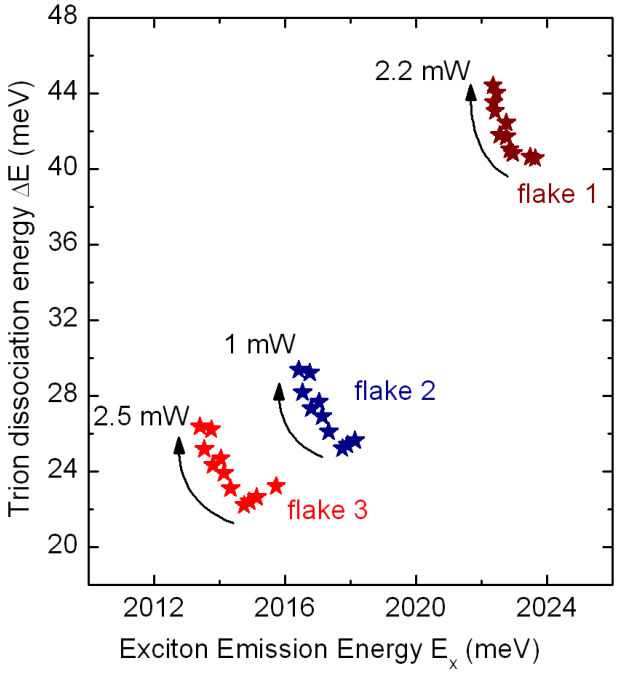

Figure 4.5: The trion dissociation energy ($E_X - E_{X^-}$) as a function of the exciton emission energy (E_X) for three different flakes of WS_2. For a given flake the exciton emission energy was tuned by varying the Fermi energy via the excitation power used. The arrows show the direction of increasing power from close to zero to the maximum indicated.

In Fig. 4.5 we plot the trion dissociation energy ΔE as a function of the exciton emission energy (E_X) for three different flakes. For a given flake the trion dissociation energy could be tuned over small range by varying the power of the 532nm excitation. As previously discussed, with increasing power the trion dissociation energy increases due to the increase in the carrier density (Fermi energy). For all flakes we can tune the trion dissociation energy over a range of $\simeq$ 4 meV which translates into the photocreation of 1.4×10^{12} cm^{-2} carriers. The increase in the

trion dissociation energy is accompanied by a small decrease ($1-2$ meV) of the exciton emission energy which we attribute to an increase in the exciton binding energy due to the reduced screening by trions which are in a spin singlet state and therefore cannot screen effectively due to the Pauli principle, as it was experimentally shown in [Plochocka 2004].

It is important to note that there is a considerable increase $\simeq 20$ meV in the trion dissociation energy when going from flake 3 to flake 1, which is accompanied by a smaller increase $\simeq 10$ meV in the exciton emission energy. Within the 2D hydrogen model the exciton binding energy is $E_B = 4R_y^*$, where R_y^* is the effective Rydberg, and the trion dissociation energy is $\approx R_y^*/2 = E_B/8$ [Ross 2013]. From flake to flake the trion dissociation energy varies in the range $20 - 40$meV corresponding to a change in exciton binding energy within the 2D hydrogen model from 160 to 320 meV. The observed increase in the exciton emission energy is much smaller ($\simeq 10$ meV) so that the increase in exciton binding energy when going from flake 3 to flake 1 has to be compensated by a similar ($\simeq 170$ meV) increase in the band gap of the crystal. However, such a compensation of the energy by large changes in the band gap seems to be unphysical. It is more likely that the trion binding energy fluctuations are due to a modification of 2D hydrogen model (screening).

4.2.2 Simultaneously tuning the exciton and trion emission using above gap excitation

Here, a simple physical mechanism which allows the tuning of the carrier density by light in our *ungated* monolayer samples is proposed. Given the n-type nature of the crystals, at low temperatures it is possible to photoionize the donors and therefore, to tune the trion dissociation energy. The unintentional n-type doping of our crystals was confirmed by transport measurements performed by Dr. Anghel in the Institute of Applied Physics, Academy of Sciences of Moldova. Figure 4.6 shows the semi-logarithmic plot of the free electron concentration (n) versus $1/T$ of unintentionally doped WS_2 bulk crystals. The free electron concentration increases exponentially with increasing temperature. At room temperature, n-type resistivity value measured is about 17 Ωcm, however, with a low electron mobility ($\simeq 40$ $\mathrm{cm}^{-2}/\mathrm{Vs}$). The solid line is the least square fitting using the relation

$$n(T) = n_0 exp(-E_D/2kT) \tag{4.1}$$

where n(T) is the free electron concentration at temperature T. We find $E_D \simeq 260$ meV with $n_0 = 4 \times 10^{19}$ cm^{-3}.

Using Hall experimental data, it is possible to estimate the density of dopants per layer. Therefore, taking into account the effective mass of the electrons in conductance band $m^* \approx 0.4m_e$ and the two fold valley degeneracy (spin degeneracy is lifted by the spin-orbit coupling $\simeq 30$ meV in conduction band), one can estimate the 2D density of states in a monolayer WS_2:

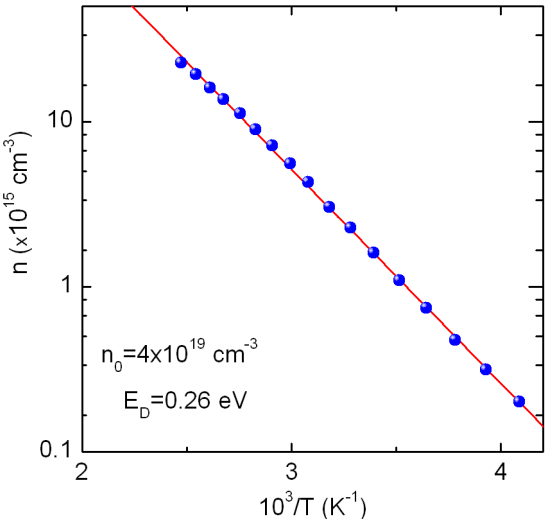

Figure 4.6: Measurements of Hall carrier density on a log scale versus inverse temperature of n-type WS_2 bulk crystals.

$$\rho^{2D} = \frac{2m^*}{\pi \times \hbar^2} = 3.3 \times 10^{11} (\mathrm{meV}^{-1}\mathrm{cm}^{-2}) \tag{4.2}$$

The 4×10^{19} cm^{-3} doping in the bulk crystal obtained from Fig. 4.6 translate to 3×10^{12} cm^{-2} dopants per sheet, assuming that layer separation in bulk crystal is $\simeq 7$Å. Thus, the change in the Fermi energy ($E_F = n_s/\rho_{2D}$) of about 4 meV at maximum power requires the creation of 1.4×10^{12} cm^{-2} carriers which is reasonable when compared to the 2D doping.

The mechanism for tuning carrier density by light in a monolayer WS_2 is presented in Fig. 4.7. Exciting the system with an energy above the band gap (green line) generates a constant density of electron-hole pairs together with a density of photo-ionized electrons in conduction band required for the observation of a charged exciton (X^-). In our 2D samples internal electric fields cannot spatially separate oppositely charged particles which makes it almost impossible to create excess charge from photo-created electron-hole pairs. However, as already presented in Fig. 4.6, at low temperature Hall data on the WS_2 crystals shows that the carriers are frozen out onto the donor levels (E_D). Thus, above gap laser illumination, in addition to creating electron-hole pairs, dynamically photo-ionizes the carriers trapped on the donor levels at low temperature, creating a non equilibrium excess electron density in the conduction band. At cryogenics temperature of 4 K and low excitation power, the dominant emission is due to excitonic states (exciton A), whereas increasing the excitation power the emission is dominated by both exciton and trion states. In higher doped samples, the trion emission becomes dominant at high excitation powers. Thus, by varying the laser power, the intensity ratio between neutral and charged exciton can be tuned.

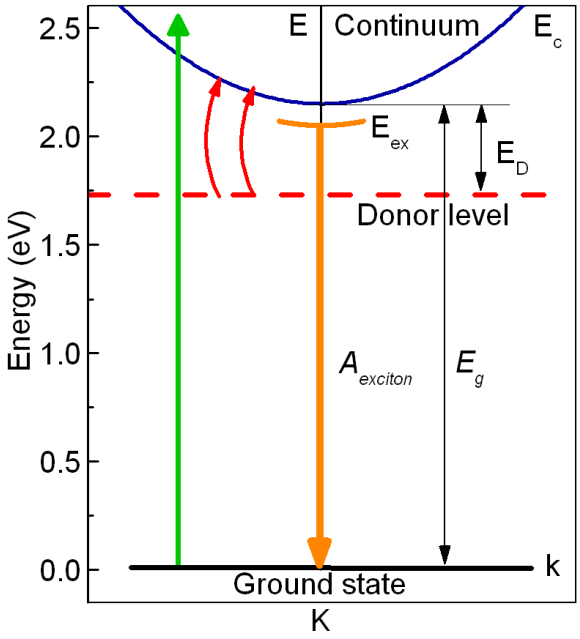

Figure 4.7: Schematic diagram showing the optical excitation of at the **K**-point in the monolayer WS_2 with above (green line) band gap excitation. The red arrows show the photo-ionization of the neutral donors using below band gap illumination. $A_{exciton}$ denotes the radiative recombination of the exciton A. E_D is the donor level energy placed below the minimum of the conduction band.

4.2.3 Independently tuning the trion emission using below gap excitation

In order to tune independently the intensity of trion emission, as well as to verify our hypothesis which invokes the photo-ionization of neutral donors, we have performed μPL using two color excitation. A low power (50 μW) for the above gap green excitation is used in order to generate a constant density of electron hole pairs together with a small density of photo-ionized electrons. Additional below gap excitation is provided by a laser centered at 860 nm (1441 meV). Photons with this energy, which is well below the gap, do not generate electron-hole pairs. The donor binding energy, attached to the direct conduction band in a monolayer is expected to be slightly different due to the different effective mass and possibly different central cell corrections. However, the correction to the binding energy is expected to be small so that photons at energy $\simeq$ 1.4 eV should be well above the threshold for the photo-ionization of the donors while remaining below the threshold for creating electron-hole pairs.

Representative two color μPL spectra measured on WS_2 flake 2 are presented in Fig 4.8(a). In the absence of below gap illumination, for the low green excitation power, the X^- line is very weak. However, when additionally illuminated using a

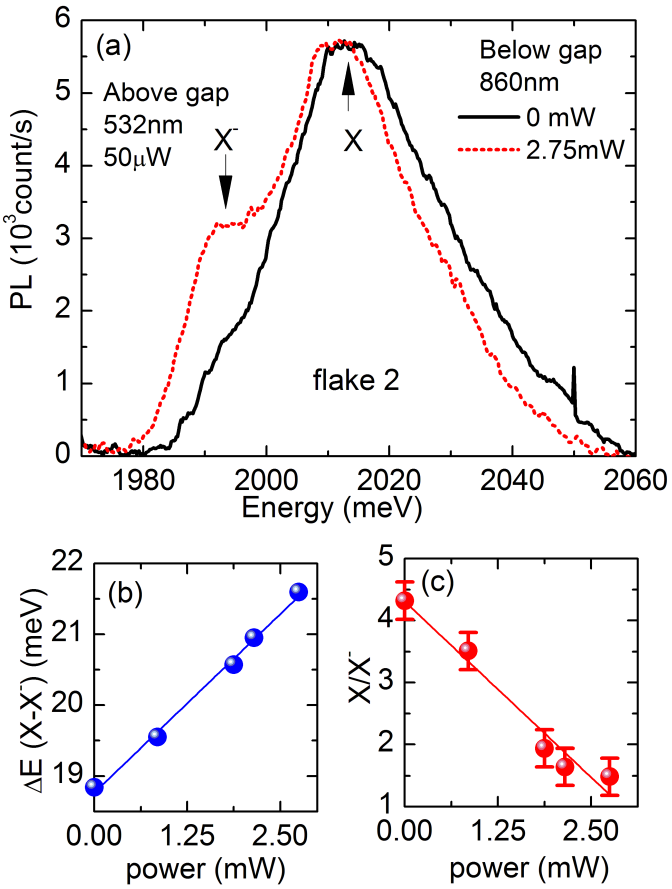

Figure 4.8: (a) Typical μPL spectra of WS_2 monolayer measured with and without additional below gap illumination. All spectra are measured with a low constant power of the green (532nm) laser (50μW). The difference between emission energy of the neutral and charged exciton (b) as a function of near infrared (860nm) laser power (below gap excitation). (c) The ratio of the integrated intensity of the charged and the neutral exciton as a function of the red laser power. The lines show the results of a linear fit.

laser at 860 nm, the intensity of the X^- emission increases while the intensity of the X emission does not change. A number of μPL spectra have been measured using a low power 532 nm excitation and different powers for the red below band gap excitation. The dissociation energy (ΔE) and ratio of the integrated intensity between X and X^- determined from the full data set are presented in Figs. 4.8(b) and (c), respectively. We observe that, as for green excitation, the trion dissociation energy ΔE increases linearly with the power of the red laser and that the intensity ratio between neutral and charged exciton also decreases linearly. This demonstrates that below band gap excitation can be used to vary the electron density in the conduction band and thus to independently tune the intensity of the trion emission.

4.3 μPL properties of monolayer WSe_2

4.3.1 Optical control of excitonic emission

The above physical picture is also consistent with the power dependence μPL measurements performed on exfoliated monolayer WSe_2 flakes. We have measured the low temperature μPL spectra as a function of excitation power for several flakes. The main difference between the results obtained on monolayer WS_2 and WSe_2 flakes is that, in most of the emission data measured on WSe_2, the charged exciton emission is more pronounced compared to WS_2. This is in a good agreement with the results recently published in Refs. [Jones 2013, Wang 2014], where the WSe_2 monolayer seems to be naturally more n-type doped. Hence, this is an advantage compared to current WS_2 monolayer flakes for the independent investigation of the neutral and charged exciton.

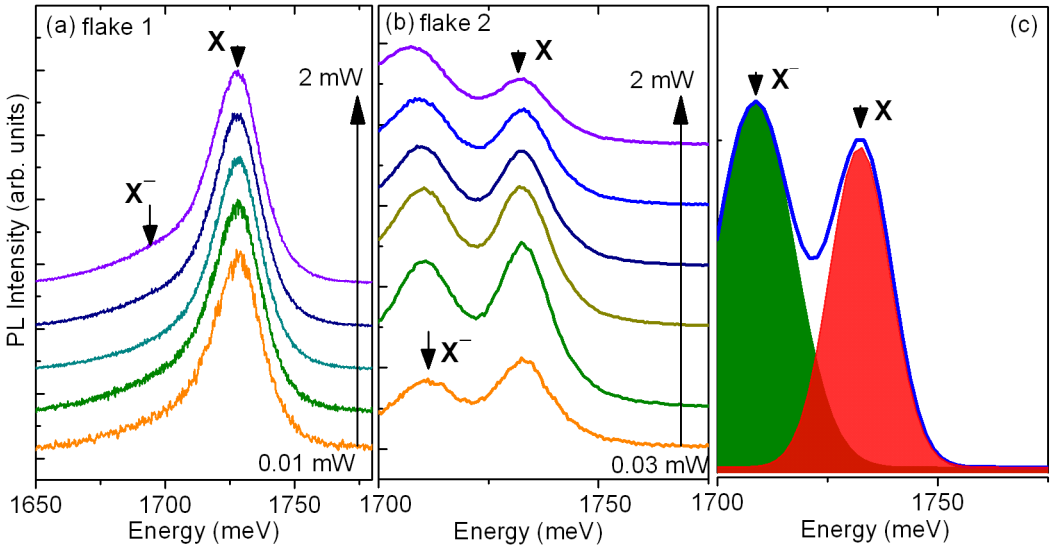

Figure 4.9: (a) and (b) Typical μPL spectra measured with 532 nm excitation power at 4K for WSe_2 monolayer. Spectra are offset vertically for clarity. (c) Gaussian fitting of the two excitonic resonances.

In Fig. 4.9 (a) and (b) the μPL spectra measured for two WSe_2 flakes as a function of excitation power are shown. The results for flake 1 WSe_2 are similar with those obtained for WS_2 monolayer flakes. The emission is dominated by neutral exciton emission while the charged exciton emission is rather weak. However, for flake 2 (Fig 4.9(b)), we observe two narrow strong PL emission lines which are clearly separated by $\simeq$ 25 meV. This suggests that already at low excitation power the trion emission is rather strong. Increasing the excitation power the trion emission line progressively gains intensity, relative to the exciton line (X) and eventually transforms into the dominant peak.

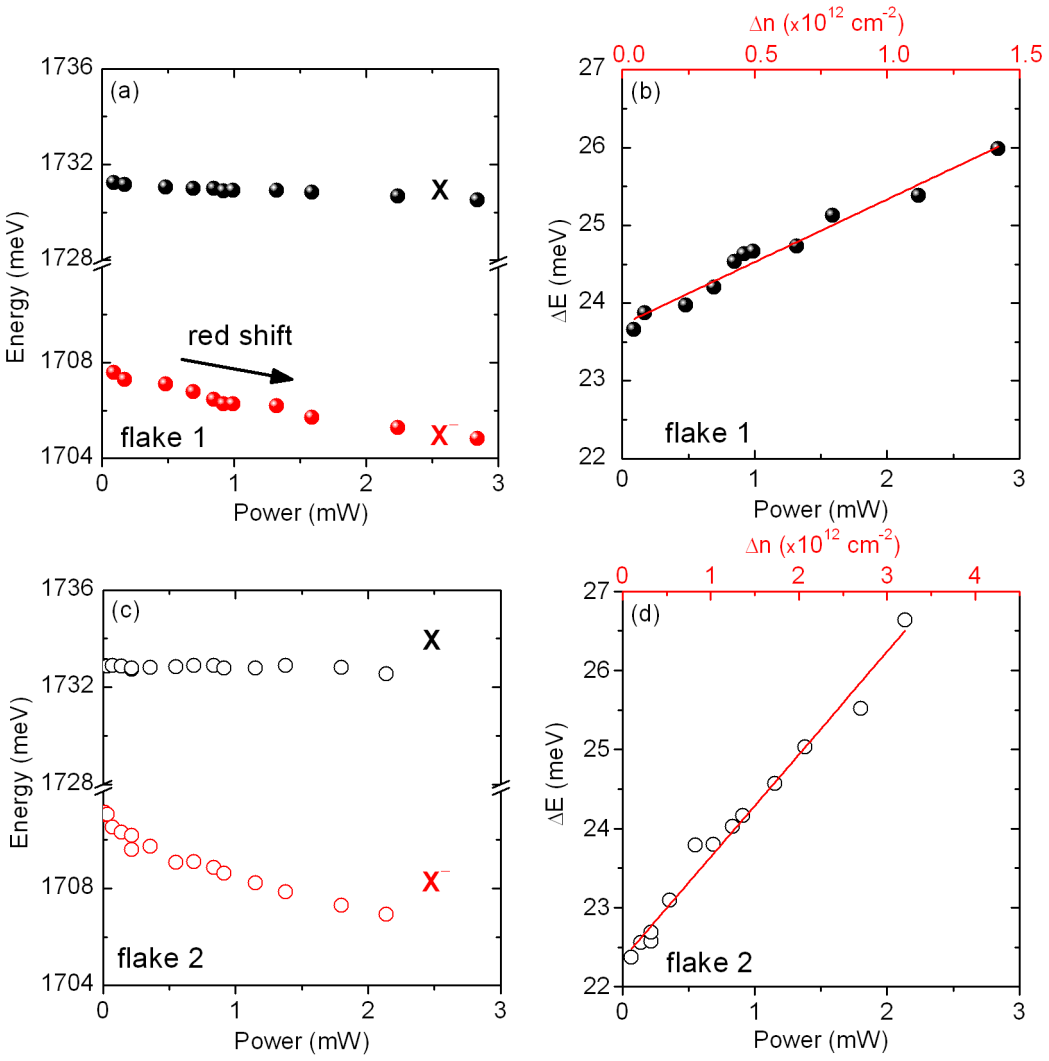

Figure 4.10: (a, c) The emission energy of the charged and the neutral exciton and dissociation energy (b, d) as a function of excitation power for WSe_2 monolayer flake 1 and 2. The lines show the results of a linear fit. Δn is the relative change of the photo-ionized carrier density.

We performed similar analysis of the data as for result obtained for WS_2 flakes. The PL spectra presented in Fig. 4.9 has been fitted using two gaussian functions to extract the intensity and position of the two excitonic resonances. For instance, in Fig. 4.9(c) is shown the fit of the PL spectrum measured on flake 2 at an excitation power of about 0.7 mW. The results of such an analysis performed on WSe_2 flakes 1 and 2 are presented in Figs. 4.10 and 4.11. Figure 4.10(a) shows the emission energy for charged and neutral exciton in WSe_2 flake 2 analyzed as a function of the excitation power. The PL peak position of X^- redshifts with increase of the

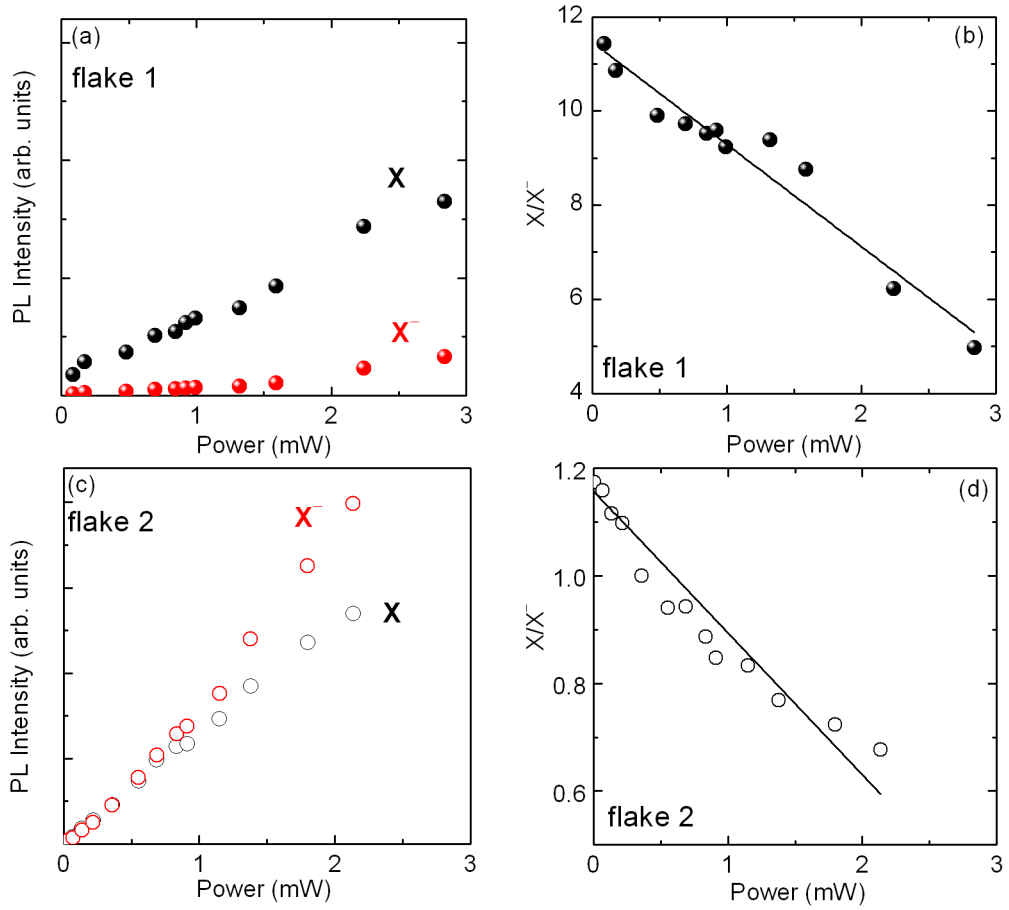

Figure 4.11: (a, c) integrated intensity of the charged and the neutral exciton and their ratio (b, d) as a function of excitation power for WSe_2 monolayer. The lines show the results of a linear fit.

excitation power, while the exciton remains almost unchanged. The typical trion dissociation energy ΔE, determined from the energy difference $(E_X - E_{X^-})$, is found to be about 22 meV, in agreement with results obtained for electrically gated WSe_2 device [Jones 2013]. The trion dissociation energy ΔE increases with the increase in excitation power, *i.e.* increase electron doping, as is shown in Fig. 4.10(b). However, in flake 2 (Fig. 4.10(d)) the trion dissociation energy increases more rapidly which, together with a larger tunable range (over 5 meV), suggests that in this flake we have a much larger concentration of free carriers.

Figure 4.11(a) and (c) shows the integrated PL intensity of neutral exciton and trion. The analysis of integrated PL performed on monolayer flake 1 WSe_2 gives similar results to WS_2 flakes (Fig. 4.4). At low excitation laser power the PL spectra of monolayer WSe_2 are dominated by the neutral exciton peak, which strongly suggests that the excitons can recombine without forming trions because of the decrease of the excess electrons in conduction band. However, in case of

the flake 2 WSe_2, shown in Fig. 4.11, we can clearly observe that increasing the excitation power, the trion emission intensity becomes dominant over the neutral exciton intensity and therefore, the probability of creating trions becomes higher as a result of capturing the excess electrons by initially generated electron-hole pairs. To illustrate this, we have calculated the intensity ratio of the neutral/charge exciton which are presented in Fig. 4.11(b) and (d). One can see that, again as in the case of WS_2, the ratio of integrated intensities decreases by a factor of more than 2. These experimental results provide a strong evidence that by only using light we can control the density of carriers in a monolayer WS_2 and WSe_2 samples.

4.3.2 Control of valley polarization by optical helicity

Linear and circular polarization analysis of the PL emission lines on monolayer WSe_2 have been performed. In Figs. 4.12(a) and 4.12(b) are shown the results of the circularly and linearly-polarized resolved PL emission on a monolayer WSe_2. As previously discussed, the spectrum consists of A exciton emission (X), trion (X^-) emission and weak emission ascribed to localized exciton complexes (L).

A typical circularly polarized-resolved PL spectrum of a monolayer WSe_2 is presented in Fig. 4.12(a). The sample were excited by $\sigma(+)$ radiation being close to the resonance with the A exciton at 1.93 eV (640 nm). We observe that that the $\sigma(+)$ polarized photoluminescence component of all three PL peaks (orange curve) is much stronger than the $\sigma(-)$ polarized photoluminescence component (black line). The magnitude of the effect is conveniently described by the degree of circular polarization,

$$P_{circ} = \frac{I(\sigma_+) - I(\sigma_-)}{I(\sigma_+) + I(\sigma_-)}, \tag{4.3}$$

where the $I(\sigma_+)$ and $I(\sigma_-)$ denotes the integrated intensity of the right and left circular polarization photoluminescence. The circular polarization of the PL emission depends on the inter valley scattering rate and the radiative recombination lifetime. In the absence of inter valley scattering the emission is expected to be 100% polarized. The measurements of inter valley scattering time on a monolayer WSe_2 will be presented and discussed in Chapter 6.

In Fig. 4.12(c) is shown the degree of circular polarization for PL spectra depicted in Fig. 4.12(a). The neutral exciton emission (X) is about 25% $\sigma(+)$ polarized, while polarization of the trion emission (X^-) is ($P_{circ} \simeq 30\%$). The circular polarization of the emission depends on the inter valley scattering rate and the radiative recombination lifetime. Our results are in good agreement with previously reported results in Refs. [Jones 2013, Wang 2014]. These results suggest that neutral and charged valley excitons have robust optical selection rules within a large neighborhood of the **K** point in the Brillouin zone and the interactions during the initial hot-carrier relaxation are not the main mechanisms causing valley depolarization.

The degree of circular polarization observed in our measurements while exciting in quasi-resonance with A-exciton is consistent with the results of [Jones 2013,

Wang 2014] in monolayer WSe_2, where P_{circ} did not change in the range of excitation from 1.85 eV to 1.93 eV. This observation is distinct from the previous valley polarization reported in monolayer MoS_2 [Mak 2012, Cao 2012], where the valley polarization was generated only when the excitation energy was within the linewidth ($\simeq$ 40 meV) of the exciton emission A. Our results suggest that monolayer WSe_2 has a valley polarization which is the most robust of all the dichalcogenides as expected due to the largest spin orbit induced spin splitting in both valence and conduction bands of any member of the dichalcogenides family.

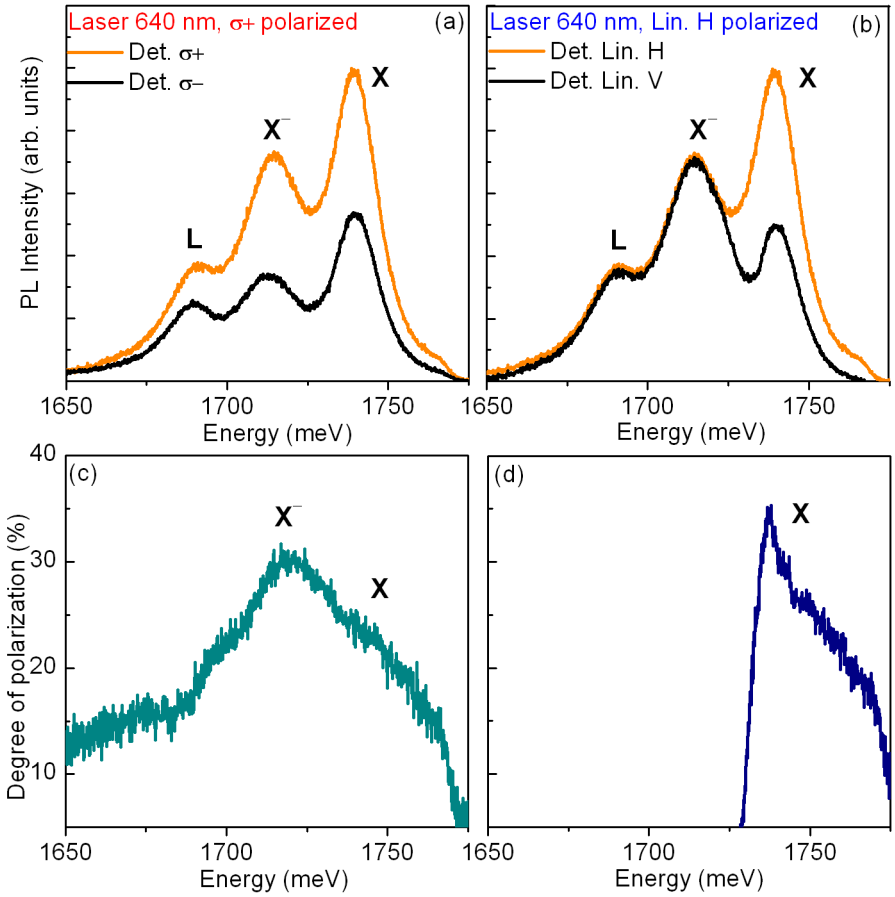

Figure 4.12: (a) and (b) Circular and linear polarization of monolayer WSe_2 PL emission at $T = 4$K. Excitation laser polarization is $\sigma(+)$ and H, respectively. (c) and (d) degree of circular and linear polarization , respectively. The charge exciton X^- and neutral exciton X emission PL peaks are marked.

We turn to the investigation of the linear polarization in steady state measurements. Fig. 4.12(b) shows the photoluminescence spectra measured under 1.93 eV horizontally (H) polarized laser excitation. The data show that the H component of X (orange curve) is much stronger than the vertically polarized (V) photoluminescence component (black curve), while the trion has equal photoluminescence

intensity for either H or V detection. As in the case of circularly resolved polarization, we define the degree of linear polarization as

$$P_{lin} = \frac{I(H_+) - I(V_-)}{I(H_+) + I(V_-)} \tag{4.4}$$

where $I(H_+)$ and $I(V_+)$ are the integrated intensity of the horizontally (H) and vertically (V) polarized photoluminescence components. In Fig. 4.12(d) one can see that neutral exciton is strongly polarized ($P_{lin} \simeq 30$ %), while trion is practically unpolarized. Linear polarization is a coherent superposition of $\sigma(+)$ and $\sigma(-)$ circular polarization. Thus, under linear polarized excitation electron-hole pairs will be simultaneously excited in both $\mathbf{K}^+$ and $\mathbf{K}^-$ and, respectively, transfer the optical coherence to valley coherence (superposition state). The fact that the neutral exciton is linearly polarized as shown in Fig. 4.12(b) and (d), independently on the incident laser polarization, is due to the preservation of the inter valley coherence in the exciton formation [Jones 2013].

The above physical mechanism is also consistent with the absence of linear polarization for the trion emission. As assumed for the discussion above, the trion charge is most likely to be negative in our samples considering the commonly observed residual n-type doping. Hence, in the case of negative trion, the are two possible configurations that in principle can emit linearly polarized photons. However, due to Coulomb (e-e) exchange interaction a small splitting may occur ($\sim$ 6 meV [Yu 2014a]) which, in principle, can destroy the valley coherence of X^- created by linear polarized excitation.

4.4 Temperature dependence of the band gap

Finally, the temperature dependance of band gap TX_2 atomically thin crystals have been investigated. The observed exciton states also show characteristic behavior consistent with 2D excitons, such as temperature-dependent line shape, peak energy and relative weight of X and trion, which further supports the excitonic nature of this monolayer system. Temperature dependance PL results for WSe_2 and WS_2 monolayer are presented in Figs. 4.13(a) and 4.14(a), respectively. One can observe that as the temperature decreases, the two PL emission lines blueshift. For monolayer WS_2 the direct gap low-energy exciton A shifts from 2.00 eV at room temperature to 2.02 eV at low temperature (T = 10K). Likewise, in monolayer WSe_2, the emission blue shifts from 1.66 eV at room temperature to 1.73 eV at T = 4K. Moreover, as the temperature increases, we observe that the trion emission signal drops due to the escaping of the electrons from their bound trion state which, together with the thermal broadening of the PL spectra, leads to an inaccurate estimation of the trion emission energy above 150 K,

The PL emission lines (L_1 and L_2), attributed to localized excitons, while prominent at low temperatures and are no longer visible for temperatures above 110 K. This feature is usually considered as an evidence of disorder-related effects, which was previously demonstrated in GaNAs/GaAs quantum wells [Buyanova 1999].

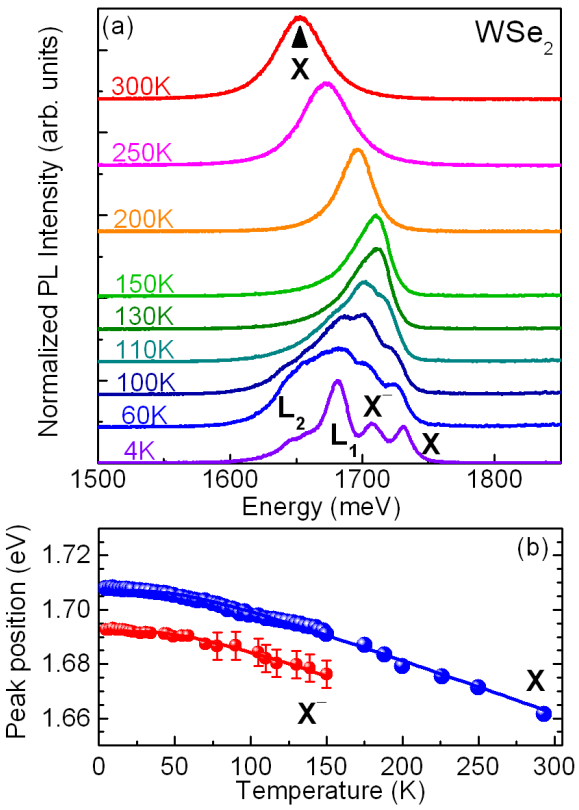

Figure 4.13: (a) Typical μPL spectra of monolayer WSe_2 measured for different temperatures. (b) Emission energy of the neutral and charged exciton as a function of temperature. X and X^- denote the emission from neutral and charged exciton. L_1 and L_2 are assigned to the localized states. Solid lines correspond to a fit using equation 4.5. Spectra are offset vertically for clarity.

In order to determine the emission energy, the PL spectra have been fitted using Gaussian functions. In Figs 4.13(b) and 4.14(b) are shown the exciton and trion emission energies as a function of temperature in monolayer WSe_2 and WS_2, respectively. The temperature dependence of the PL emission energy can be accurately reproduced using a simple model for the temperature dependence of the band gap in semiconductors proposed by [O'Donnell 1991]:

$$E(T) = E_0 - S\langle\hbar\omega\rangle\left[coth\left(\frac{\langle\hbar\omega\rangle}{2k_BT}\right) - 1\right] \tag{4.5}$$

where E_0 is the emission energy at zero temperature, S is a dimensionless coupling constant linked to electron-phonon coupling and $\langle\hbar\omega\rangle$ is the average phonon energy. The best fit to the neutral exciton is obtained with $E_0 = 2.017$ eV, $S = 0.56$ and $\langle\hbar\omega\rangle \simeq 10.4$ meV for WS_2 and $E_0 = 1.712$ eV, $S = 0.75$ and $\langle\hbar\omega\rangle \simeq 6.1$ meV for WSe_2. The smaller value of $\langle\hbar\omega\rangle$ obtained for WSe_2 monolayers can be explained

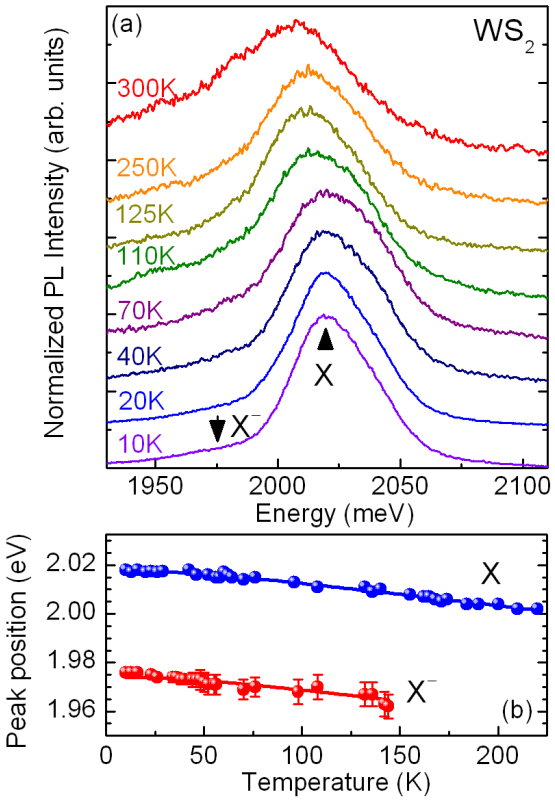

Figure 4.14: (a) Typical μPL spectra measured for different temperatures on monolayer WS_2. (b) Emission energy of the neutral and charged exciton as a function of temperature. Solid lines correspond to a fit using equation 4.5.

by the fact that Se atoms are heavier than S atoms and thus, the phonon energy decreases in diselenide compounds. The charged exciton is well fitted using the same parameters except for the zero temperature emission energy $E_0 = 1.973$ for WS_2 and $E_0 = 1.668$ for WSe_2.

4.5 Conclusion

In this chapter using μPL measurements the emission from charged and neutral exciton in an *ungated* monolayer of WS_2 and WSe_2 has been observed. The trion emission is closely linked to the n-type nature of our crystals. Using two color μPL with above and below band gap illumination it is possible to independently tune the trion/exciton intensity ratio. The below band gap excitations tunes the excess electron density in the conduction band via the dynamic photo-ionization of neutral donors. Since the photo-ionization threshold will be similar to the donor binding energy $\simeq$ 260meV this provides a possible method for the optical detection of far infrared radiation.

Chapter 5

Resonant μ-Raman scattering in monolayer WS_2

Contents

In this chapter, the results of resonant μ-Raman measurements performed on monolayer tungsten disulphide (WS_2) are presented. We start with a brief introduction to the Raman scattering processes followed by a description of the main phonon modes in bulk and monolayer WS_2 crystals. Next, we present the experimental results of resonant Raman scattering on monolayer WS_2. The main finding is the observation of a second-order Raman mode (2LA), only $4cm^{-1}$ below the first-order Raman mode E^1_{2g}. We show that the presence of the 2LA mode can pose significant problem when using Raman to assign the number of layers. We have investigated the properties of this second order Raman mode as a function of excitation power, temperature and linear polarization. Some of the results presented in this chapter have been published in Physical Review B ***89****, 245442 (2014).*

5.1 Introduction

Several experimental techniques have been employed to study electronic properties of layered materials. Among them, Raman spectroscopy has been extensively

used and, it has been shown to be a very powerful technique to determine the number of layers in graphene [Ferrari 2006, Gupta 2006] or in dichalcogenides [Gutiérrez 2013, Li 2012b, Lee 2010, Li 2013, Wang 2012]. This is because the vibrational spectra are sensitive to the crystal thickness. In particular, in dichalcogenides, the distance between two main first-order Raman peaks strongly depends on the number of layers [Lee 2010, Li 2012b, Wang 2012, Gutiérrez 2013, Li 2013]. Additionally, the excitonic transitions observed in the visible spectral range (A, B or C), coincide well with the laser lines commonly used in Raman spectroscopy. As a consequence, it is relatively easy to observe resonant Raman spectra in these materials.

Resonant Raman spectra are composed of both first and second order Raman excitations, as has been demonstrated for bulk MoS_2 [Chen 1974, Frey 1999] or WS_2 [Sourisseau 1989, Sourisseau 1991, Sekine 1980]. Recently, second order Raman modes have also been reported in monolayer WS_2 [Berkdemir 2013, Dumcenco 2011, Song 2013, Zeng 2013], MoS_2 [Li 2012a], $TaSe_2$ [Hajiyev 2013] and WSe_2 [Luo 2013]. Such resonant vibrational spectra can provide significant additional information concerning the electronic properties of the material. For example, it has been suggested that the observation of a strong second order Raman resonance involving the longitudinal acoustic phonons (2LA) in monolayer WS_2 is a signature of the monolayer nature of the sample [Berkdemir 2013].

Nevertheless, resonant Raman spectra in atomically thin dichalcogenides are relatively unexplored, and far from being fully understood. For example, in monolayer WSe_2, an additional Raman mode, separated by only a few cm^{-1} from the E^1_{2g} mode, and whose origin remains to be elucidated, was recently reported [Luo 2013]. Moreover, the inter valley scattering process involving a second-order phonon mode was suggested to be the main source of valley depolarization [Kioseoglou 2012]. For these reasons, understanding the resonant Raman processes in dichalcogenides is of great importance.

In this chapter, we present resonant Raman scattering measurements performed on a monolayer tungsten disulphide[1]. We focus on the second order Raman resonance involving the longitudinal acoustic phonon (2LA), which is separated by only $4cm^{-1}$ from the E^1_{2g} mode. We show that due to their small separation, the two modes can be undistinguishable, leading to an erroneous estimation of the separation of the E^1_{2g} and A_{1g} modes, which is normally accepted to be a robust indication of the crystal thickness. Measurements involving linear polarization show that depending on the angle between polarization of the excitation and detection the 2LA mode can even dominate over the E^1_{2g} mode or *vice versa*. Our results demonstrate that great care has to be exercised when interpreting Raman spectra taken under resonant conditions, especially if the excitation polarization is not carefully controlled. The temperature-dependence Raman measurements nicely demonstrate the overtone character of the 2LA mode.

[1] Only the 2H-polytype of WS_2 is discussed.

5.2 Raman scattering principle

5.2.1 Raman scattering effect

Light scattering techniques is a very useful tool to probe the fundamental excitations in solids, such as phonons, plasmons, *etc*, in a non-invasive way. In a typical experiment, an incident monochromatic light with an energy $\mathbf{E}_i$ impinges on a crystal. As a result of the interaction with phonons or other excitations in the crystal, the energy of the photons after scattering ($\mathbf{E}_s$) can be the same or, of either lower (Stokes) or higher (anti-Stokes) energy than the incoming photon. If $\mathbf{E}_i = \mathbf{E}_s$, the scattering process is elastic and it is called *Rayleigh scattering*. If $\mathbf{E}_i - \mathbf{E}_s$, the scattering is inelastic and it is called *Raman scattering* and the energy difference $\Delta\mathbf{E} = \mathbf{E}_i - \mathbf{E}_s$ is referred to as the *Raman shift*. During the scattering, both energy and momentum have to be conserved:

$$\mathbf{E}_i = \mathbf{E}_s \pm \mathbf{E}_q \tag{5.1}$$

$$\mathbf{k}_i = \mathbf{k}_s \pm \mathbf{k}_q \tag{5.2}$$

where $\mathbf{k}_i$, $\mathbf{k}_s$ are the momenta of the incident and scattered photon on the crystal. Here we consider only the lattice excitation (phonons), and $\mathbf{E}_q$ and $\mathbf{k}_q$ are the energy and momentum of the created and/or annihilated phonons during the inelastic scattering process, which is schematically illustrated in Figure 5.1.

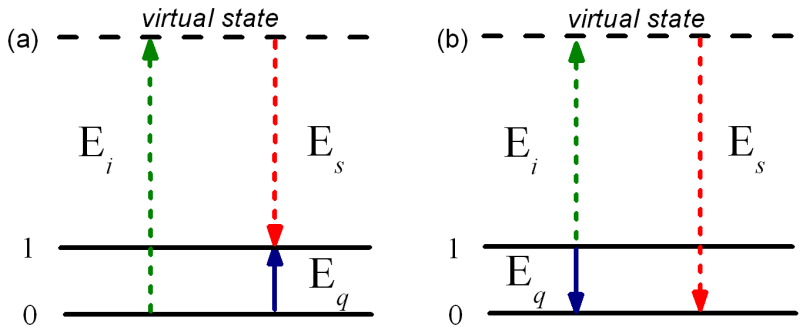

Figure 5.1: Energy-level diagram showing the states involved in Raman scattering process. (a) The incoming photon leads to annihilation (absorption) of the phonon and (b) the incoming photon looses part of its energy to create (emit) a new phonon.

If a system is initially in a state "0", then light scattering can excite the system to a higher energy state "1" by absorption (annihilation) of a phonon with an energy $\mathbf{E}_q$, as depicted in Fig. 5.1(a). In a similar way, the system can initially be in a state "1" and light scattering can serve to bring the system to a final state of lower energy "0" illustrated in Fig. 5.1(b) by creation (emission) of a phonon with energy $\mathbf{E}_q$. It is worth noticing that in contrast to the photoluminescence process, in the Raman

scattering process the intermediate states are "virtual" states because they do not have to correspond to any optical excitation of the electronic levels of the system.

5.2.2 Light-matter interaction

The light scattering can be described using classical electromagnetic theory. The polarization ($\mathbf{P}$) is induced in a crystal by an incident electromagnetic radiation $\mathbf{E}$. The relation between these two quantities is

$$\mathbf{P} = \alpha \mathbf{E} \tag{5.3}$$

where $\mathbf{E} = \mathbf{E}_i cos\omega_i t$ is the electric field of the incident light and α is the polarizability tensor of the crystal. In order to distinguish between the static polarization originating from atoms resting in equilibrium position and dynamic polarization resulting from the lattice vibrations, a Taylor expansion of polarizability is used:

$$\alpha = \alpha_i + \frac{\partial \alpha}{\partial u_j} u_j + \frac{\partial^2 \alpha}{\partial u_i \partial u_j} u_i u_j + ... \simeq \alpha_i + \alpha_1 cos\omega_q t. \tag{5.4}$$

As a consequence, the expression for the polarization induced by an electric field takes form

$$\mathbf{P} = \alpha_i \mathbf{E}_i cos\omega_i t + \alpha_1 \mathbf{E}_i [cos(\omega_i + \omega_q)t + cos(\omega_i - \omega_q)t] \tag{5.5}$$

The first term in eq. (5.5) corresponds to elastically scattered light with the same frequency as the frequency of the incident light and it corresponds to Rayleight scattering. The second and third terms correspond to inelastically scattered light and their frequencies are shifted to higher (anti-Stokes) and lower (Stokes) frequencies with respect to frequency of incident light, as schematically presented in Fig. 5.2. These two terms describe *Raman scattering* in the classical picture.

In inelastic scattering process the incoming photon induces a movement of the electrons. At different atomic positions within the vibrational mode displacement of the atom, the ability of the photon to move the electrons will be different. This is measured by the polarizability $\mathbf{P}$. Hence, the vibrational modes are often called *normal modes* and are connected to the electronic properties of the investigated material.

Classical theory predicts that Raman scattering should be weaker than Rayleigh scattering. To a first approximation, the relative Stokes and anti-Stokes intensity is determined by the Boltzmann distribution of the phonons. The excited vibrational state will be only thermally populated, and Stokes intensity will be much larger than anti-Stokes. Indeed, in Figure 5.2 are illustrated the typical Rayleigh and Raman traces, where an incident light with frequency ω_i creates Stokes and anti-Stokes components which correspond to the creation/annihilation energy of a phonon. In Raman experiments using visible light, the wavevector of the incident photon is of the order of 10^5 cm^{-1}, which will create a maximum phonon wavevector of the same order of magnitude. If we compare this value with the dimensions of the first

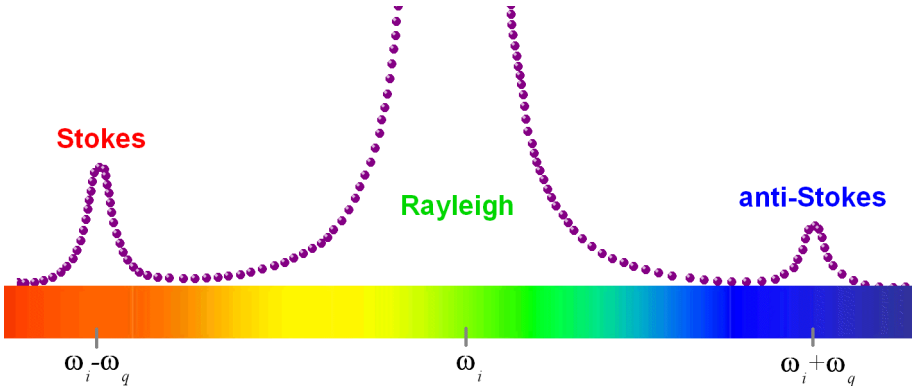

Figure 5.2: Typical Rayleigh and Raman scattering peaks in the spectrum. The intensity of the Stokes processes is typically stronger than the anti-Stokes processes.

Brillouin zone, which typically is of the order of 10^8 cm^{-1}, we can see that Raman scattering with visible light only probes phonons with small wavevectors and thus is limited to the zone-center phonons. The probability to create or annihilate a phonon depends on the phonon statistics, which is given by the Bose-Einstein distribution function. At a given temperature, the occupation number of phonons n_q with energy E_q (and wavenumber q) is given by:

$$n_q = \left[exp\left(\frac{E_q}{kT}\right) - 1 \right]^{-1} \tag{5.6}$$

where k is the Boltzmann constant and T the temperature of the phonon system. The intensity for the Stokes and anti-Stokes processes is different. For the Stokes process the matrix element for adding a phonon to the crystal is $\langle n+1|Q|n\rangle$. For the anti-Stokes process the corresponding matrix element for the annihilation of the phonon is $\langle n-1|Q|n\rangle$, where $|n\rangle$ is a many-body wavefunction and $Q_m(\omega, q)$ is the phonon coordinate or, alternatively, the amplitude of the mode of frequency ω and wave vector q [Weber W.H. 2000]. In the former case the harmonic approximation gives $\sqrt{n_q+1}$, while in the later case - $\sqrt{n_q}$. The intensity ratio between the Stokes and anti-Stokes signals can be approximated by:

$$\frac{I_{Stokes}}{I_{aStokes}} = \frac{|R_{ij}|^2 \times |\sqrt{n_q+1}|^2}{|R_{ij}|^2 \times |\sqrt{n_q}|^2} = \frac{n_q+1}{n_q} = exp\left(\frac{E_q}{kT}\right) \tag{5.7}$$

where I_{Stokes} and $I_{aStokes}$ are the intensity for the Stokes and anti-Stokes peaks. R_{ij} is the first-order Raman tensor. Since the anti-Stokes signals are typically weaker than the Stokes signals, it is common to refer to the Stokes spectra when showing Raman experimental results. All the results presented in this chapter focus on the Stokes contribution to the Raman spectrum.

5.3 Phonon modes in bulk and monolayer WS_2 crystals

This section briefly describes the main phonon modes in bulk and monolayer transition metal dichalcogenides crystals. After discussing the main normal modes in bulk and monolayer crystals[2], we continue with the Raman spectra measured under non-resonant and resonant excitations.

5.3.1 Non-resonant Raman scattering spectra

The symmetry space group of 2H-polytype TX_2 bulk crystals is $P6_3/mmc$ (point group D_{6h}). Therefore, having $N = 6$ atoms per unit cell result in 18 ($3N$) normal modes of vibration: 3 acoustic and 15 ($3N - 3$) optic. The Γ point phonons modes transform according to the following irreducible representation [Verble 1970]:

$$\Gamma = 2A_{2u} + 2E_{1u} + 2B_{2g} + 2E_{2g} + A_{1g} + E_{1g} + B_{1u} + E_{2u} \tag{5.8}$$

where the A and B modes involve an out of plane vibrational motion of the atoms and are non-degenerate, whereas the doubly degenerate E representations stand for the in plane vibrational modes.

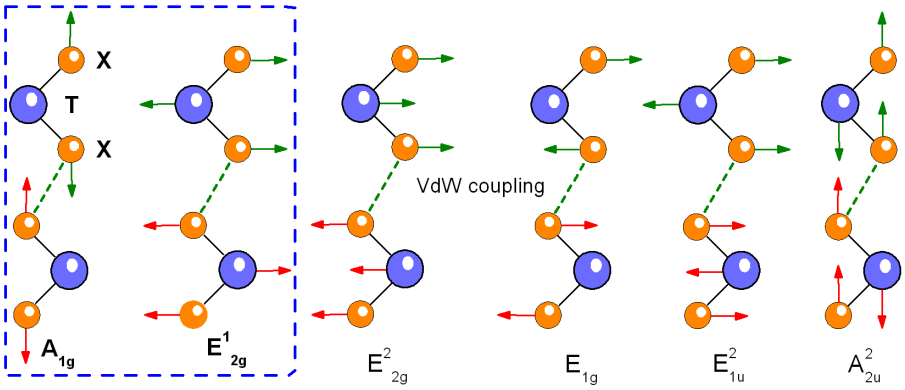

Figure 5.3: Schematic showing the normal modes of 2H-TX_2 compounds. A_{1g}, E_{1g}, E^1_{2g} and E^2_{2g} are Raman active modes, A^2_{2u} and E^2_{1u} - infrared active modes. The T symbol denotes the transition metal atoms (blue circles), while X the chalcogen atoms (orange circles). The A_{1g} and E^1_{2g} modes, enclosed by blue-dashed line, are the main modes observed typically in the Raman spectra.

The A^2_{2u} and E^2_{1u} modes are infrared active and the other ones, A^1_{2u} and E^1_{1u}, are inactive and by type are translational acoustic modes. There are four Raman active modes A_{1g}, E_{1g} and $2E_{2g}$ that can be observed in typical Raman spectra of 2H-TX_2 bulk crystals are schematically illustrated in Fig. 5.3. Finally, $2B_{2g}$ and B_{1u} are the silent modes.

In back scattering configuration[3], the E_{1g} mode, associated with an in plane

[2] Only the 2H polytype is considered.
[3] Typically used in Raman experiments.

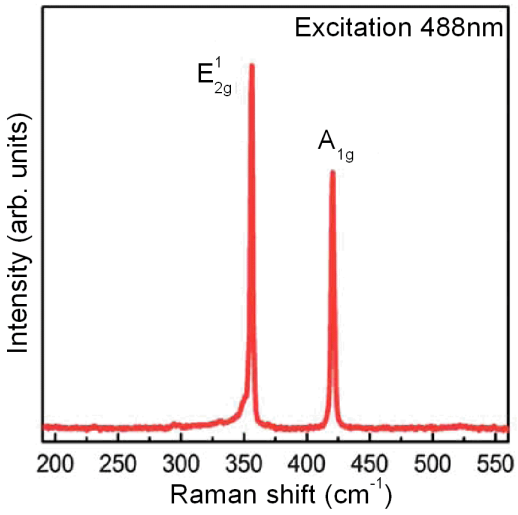

Figure 5.4: Typical non-resonant Raman spectrum of a 2H-polytype WS_2 bulk crystal at room temperature. After Sekine et al. [Sekine 1980].

motion of only chalcogen atoms, is forbidden. The E^2_{2g} is a shared mode originating from the relative motion of the atoms in different layers and is observed only in the very low frequency region (< 50 cm^{-1}). As a result, the Raman spectra of a bulk TX_2 crystals are dominated by two first order modes: E^1_{2g}, which is associated with the in plane motion of the chalcogen and transition metal atoms in opposite directions and A_{1g}, which is associated with the out of plane motion of the chalcogen atoms (see the modes enclosed by a rectangle with blue-dashed line in Fig. 5.3). Fig. 5.4 shows the typical Raman spectrum (488 nm excitation wavelength) of 2H-WS_2 bulk crystal measured at room temperature [Sekine 1980]. The Raman spectrum is dominated by two strong resonances at around 355 and 423 cm^{-1} which correspond to the frequency of the main Raman-active modes E^1_{2g} and A_{1g} in WS_2, respectively [Sekine 1980, Sourisseau 1989].

While reducing the thickness of the bulk crystal to monolayer, the symmetry is also reduced to the D_{3h} point group (space group $P6m2$). This leads to a reduction of the total number of phonons in monolayer to 9. The irreducible representations of modes at the Γ-point of Brillouin zone is:

$$\Gamma = 2A_{2u} + 2E_{2g} + A_{1g} + E_{1g} \tag{5.9}$$

where A_{2u} is an infrared active mode and A_{1g}, E_{1g} and $2E_{2g}$ are the Raman active modes. In back scattering configuration, the E_{2g} mode is forbidden. Thus, the Raman spectra in a monolayer are dominated by the same Raman-active modes E^1_{2g} and A_{1g}. Recently it has been shown that the frequencies of these two modes depend very strongly on the number of layers [Lee 2010, Plechinger 2012, Staiger 2015]. Such a dependence measured by Staiger et al. [Staiger 2015] is presented in Figure

5.5(a). It is observed that with increasing number of layers the out of plane A_{1g} mode upshifts, whereas the in plane E^1_{2g} mode softens. Evolution of the frequency of the main E^1_{2g} and A_{1g} modes with the number of layers, as well as the frequency separation between these two modes is illustrated in Figure 5.5(b). It is generally accepted that in bulk WS_2 crystals, the separation between these two modes is 66cm^{-1} and it decreases gradually with the number of layers reaching 62cm^{-1} for a monolayer, as also reported in references [Gutiérrez 2013, Berkdemir 2013, Zhao 2013]. However, due to strain, a small rigid shift of the two Raman peaks (A_{1g} and E^1_{2g}) can be observed, but with no change in the peak separation ($\omega(A_{1g}) - \omega(E^1_{2g})$), as can be observed in Fig. 5.5. Typically this change is accompanied by a small change in the emission PL maxima with changing the position of the laser spot on the sample [Conley 2013, Rice 2013].

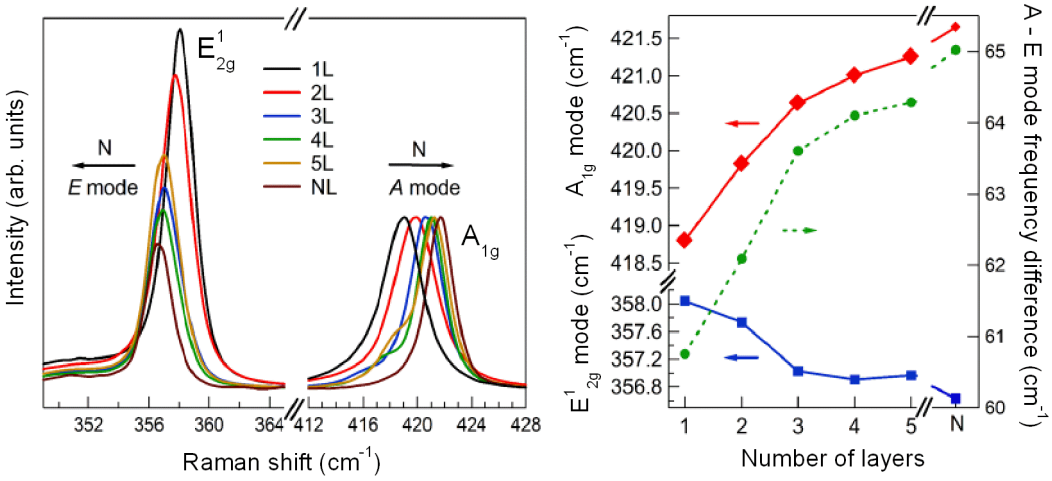

Figure 5.5: (a) Raman spectra measured for different numbers of layers starting from a monolayer up to bulk (nL) WS_2 crystals. (b) Evolution of the frequency of the main E^1_{2g} and A_{1g} modes with the number of layers. The dashed line shows the frequency separation between the E^1_{2g} and A_{1g} mode. After Staiger et al. [Staiger 2015]

The stiffening of the out of plane A_{1g} mode has been explained by the increasing interlayer interaction and subsequent rise in restoring forces on the atoms with the number of layers [Lee 2010]. In contrast, the E^1_{2g} mode anomalously softens. For the E^1_{2g} mode, the atoms move in plane and the influence of the inter layer interaction stiffening is thus expected to be smaller. The observed softening has been attributed to an enhanced dielectric screening provided by additional layers [Molina-Sanchez 2011]. Thus, the opposite frequency shifts of the A_{1g} and E^1_{2g} allow the separation between the two modes to be used as a fingerprint for the number of layers.

5.3.2 Resonant Raman scattering spectra

In some experiments the energy of the photon corresponds to the real electronic states. If the photon energy does not correspond to a real transition in the electronic band structure, the electron that absorbs the energy is said to be in a intermediate state. From there, it can couple to the lattice. However, if the photon energy used for crystal excitation corresponds to a real electronic transition in a crystal from an occupied initial state to an unoccupied final state, the Raman scattering intensity will be enhanced. Such a process is called *resonant Raman scattering*. In TX_2 materials, the excitonic transitions are placed in the visible spectral range and the observation of resonant Raman scattering is natural. For example, several experimental results on resonant Raman scattering have been reported on bulk WS_2 crystals [Sourisseau 1989, Sourisseau 1991, Sekine 1980] and their monolayer crystals counterparts [Berkdemir 2013, Staiger 2015]. Figure 5.6(a) presents the typical results of the Raman for different excitation wavelengths. Among the five wavelengths used for excitation, only the 488 nm laser line (blue line spectrum) is out-of-resonance. The two first order Raman-modes (E^1_{2g} and A_{1g}), are visible in all the spectra however, their intensity depends on excitation wavelengths. For resonant excitation, some additional modes are seen. These new modes have been assigned to a multi-phonon combinations of the first order modes (enclosed by a rectangle with blue-dashed line in Fig. 5.6(a)) [Sourisseau 1989]. Moreover, at the low energy side of E^1_{2g} peak, a shoulder is observed whose intensity is very sensitive on the excitation wavelength. This peak has been assigned to a second order longitudinal acoustic mode (2LA) and also, in combination with the first order modes which give rise to new additional modes [Sourisseau 1989].

The wavelength-dependent Raman scattering process has been explained recently in terms of a spatial confinement of the wave function which has a strong influence on these processes [Scheuschner 2015]. It has been suggested that if the Raman excitation is in resonance with the A or B exciton in few-layer TX_2, the excitation is still confined mainly to a monolayer. As a result, the bulk crystal reacts rather like an independent superposition of N single layers from a selection-rule point of view. Only when the optical excitation creates an exciton that is extended over the entire number of layers, as in resonance with the C transition, the symmetry of the bulk crystal becomes dominant and determines the selection rules. Figure 5.6(b) illustrate schematically the different regimes of optical excitations. At 1.96 eV (red arrow in 5.6(b)), the A exciton resonance is reached and the intensity of 2LA mode is stronger with respect to the intensity of E^1_{2g}. With increasing the excitation energy, from 2.33 to 2.41 eV, the B exciton is reached (green and violet arrows in 5.6(b)). At 2.46 eV (dark yellow arrow in 5.6(b)), the C exciton resonance is reached, which appears to be the first resonance which is extended over a number of layers. At excitation energies below 1.9 eV (black arrow) and above 2.5 eV (blue arrow), the resonance is lost and the Raman signal is weak. Overall, these results provide an initial understanding of the large resonance range in WS_2 crystals. This is important, since resonant Raman scattering can provide significant

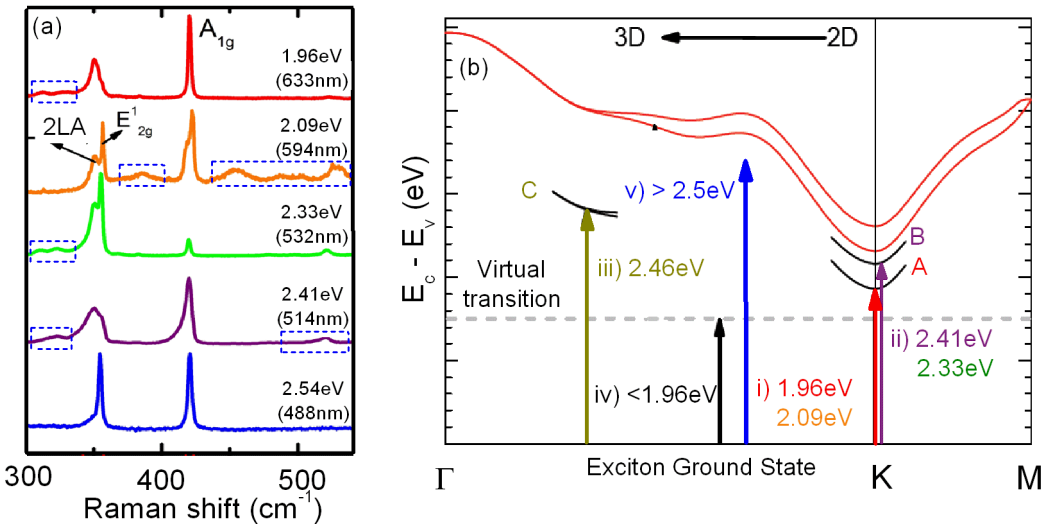

Figure 5.6: (a) Room temperature Raman spectra of bulk WS_2 crystals for five different incident photon energies [Fan 2014]. The Raman modes enclosed by a rectangle with blue-dashed line are multi-phonon combinations of the first order modes due to resonant excitation. (b) Schematic illustrating the optical absorption process for i) 1.96 and 2.09 eV, ii) 2.33 and 2.41 eV, iii) 2.46 eV, iv) <1.96 eV and v) >2.5 eV excitation energies. After Scheuschner et al. [Scheuschner 2015].

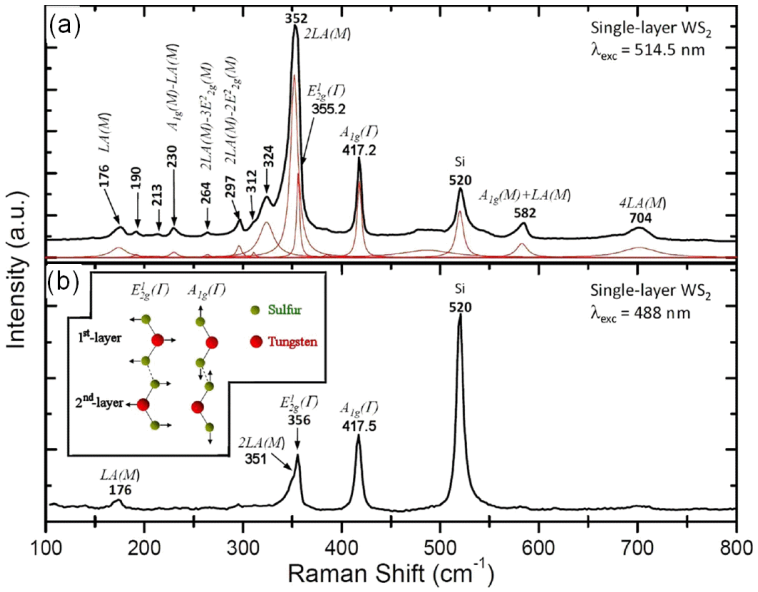

Figure 5.7: Room temperature resonant (a) and non-resonant (b) Raman spectra of monolayer WS_2 crystals [Berkdemir 2013].

additional information concerning the electronic properties in this material.

Recently, the resonant Raman scattering in a monolayer WS_2 flakes has been reported in references [Berkdemir 2013, Staiger 2015]. As in the bulk WS_2 crystals, the resonance in monolayer still occurs over a large range of wavelengths. The resonant energy range seems to be unaffected by the transition from indirect to direct gap when the crystal is thinned down to a monolayer. This suggests that the resonance is dominated by the excitonic excitations at the **K** point of the Brillouin zone, in both bulk and monolayer WS_2. One difference between the resonant spectra of the bulk and monolayer is, in fact, a stronger intensity of the overtone of the acoustic mode LA(M) when the excitation wavelength is in the vicinity of B exciton as illustrated in Fig. 5.7. It has been suggested that the observation of a strong second order Raman resonance involving the longitudinal acoustic phonons (2LA) in monolayer WS_2 is a signature of the monolayer nature of the sample [Berkdemir 2013]. However, we will see that the amplitude of the 2LA Raman mode depends on the polarization of the excitation, as well as on the temperature.

5.4 Experiment - Resonant Raman scattering in monolayer WS_2

Here we present our investigation of resonant μRaman scattering in monolayer WS_2. The monolayer samples used for measurements have been described in Chapter 3. In our resonant Raman scattering experiments, a green solid state laser, emitting at 532 nm, which is in resonance with the direct excitonic transition B (2.4 eV) was used. Typical room temperature resonant Raman spectrum of a monolayer WS_2 is presented in Fig. 5.8. Due to resonant excitation, the Raman spectrum is very rich, revealing second order peaks that are stronger than those observed in the bulk material. Figure 5.8 gives also the symmetry assignments for several peaks according to previous reports in bulk and fullerene-like WS_2 nanostructures [Sourisseau 1989, Sourisseau 1991, Staiger 2012, Berkdemir 2013]. The strong resonance around 417 cm^{-1} in Figure 5.8 corresponds to the first-order Raman modes A_{1g}. However, the peak around 353 cm^{-1} is more complicated: a peak at 351 cm^{-1} accompanied by a weaker peak at 355 cm^{-1} corresponding to the E^1_{2g} mode in monolayer WS_2. This additional peak has been assigned to a second order Raman resonance involving longitudinal acoustic phonons (2LA) and has been reported for bulk crystals and only very recently for monolayer WS_2 [Berkdemir 2013, Song 2013]. The other two Raman modes with low intensity observed at $\sim$ 300 and $\sim$ 320 cm^{-1} in Figure 5.8 could be assigned to some combinational modes which involve the first-order E_{1g} mode, which in bulk crystals is not allowed in the back scattering geometry.

Here, the resonant Raman spectra of monolayer 2H-WS_2 have been investigated mainly in the vicinity of the Raman-active E^1_{2g} phonon at 355 cm^{-1} and A_{1g} phonon at 417 cm^{-1} (see the red-dashed-rectangle in Fig. 5.8). In the following the temperature, excitation-power and polarization dependence of the resonant Raman modes are discussed.

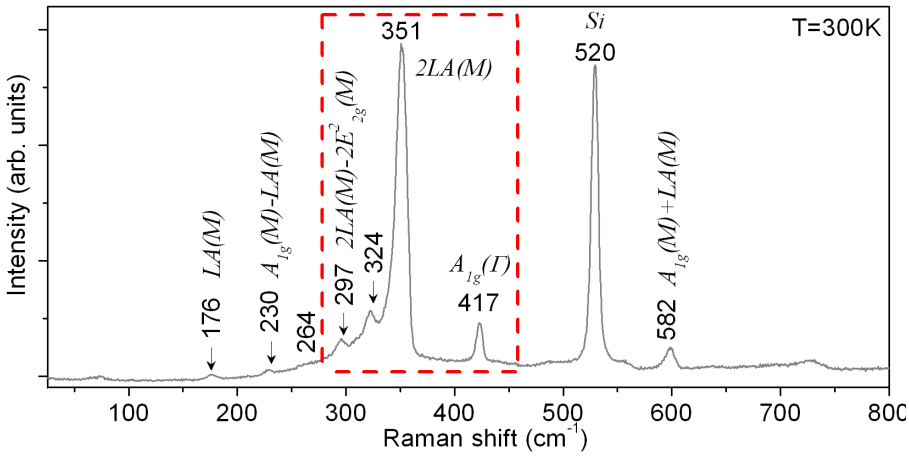

Figure 5.8: Typical room-temperature Raman spectrum from a monolayer WS_2 region using 532 nm laser excitation. The E^1_{2g}, A_{1g} and LA are are the first order Raman modes. The other assignments denote the second order Raman modes. In this chapter is investigated the resonant Raman scattering spectral range enclosed by a rectangle red-dashed line.

5.4.1 Temperature-dependence resonant Raman scattering

In Fig 5.9(a) is presented the resonant Raman spectrum taken at 300K. The resonance peak at 417 cm^{-1} corresponds to the A_{1g} mode in monolayer of tungsten disulphide [Gutiérrez 2013, Berkdemir 2013, Zhao 2013, Zeng 2013, Song 2013]. Since the Raman spectrum is now illustrated for a much smaller range, it is clearly seen that the peak around 353 cm^{-1} has a shoulder which has been previously assigned to the 2LA and E^1_{2g} modes, respectively. Although, the spectrum is slightly more complicated, the separation between A_{1g} and E^1_{2g} is still 62cm^{-1} which proves the **single layer** character of our sample. At first sight, our data suggests, in apparent agreement with calculations and measurements presented by [Berkdemir 2013], that the 2LA mode is stronger than E^1_{2g} mode for monolayer material.

Independent proof of the 2LA character of the peak at 351 cm^{-1} is provided by measurements at low temperature ($T = 4$K) presented in Fig 5.9(b). Compared to the Raman data measured at 300K, a small blue shift of the resonance frequencies is observed with decreasing temperature due to the anharmonic vibrations in the lattice in the interatomic potential energy mediated by phonon - phonon interactions [Yan 2014, Lanzillo 2013]. As the lattice expands or contracts because of temperature changes, the equilibrium positions of the atoms and consequently the interatomic forces change, which induces shifts in the phonon energies. Such a behavior of Raman peak frequencies with temperature is seen in many materials within a certain temperature range [Hart 1970, Postmus 1968]. The dominant effect of the temperature is the radical change in the intensity ratio between the E^1_{2g} and 2LA modes. At room temperature the 2LA mode dominates over the E^1_{2g} while

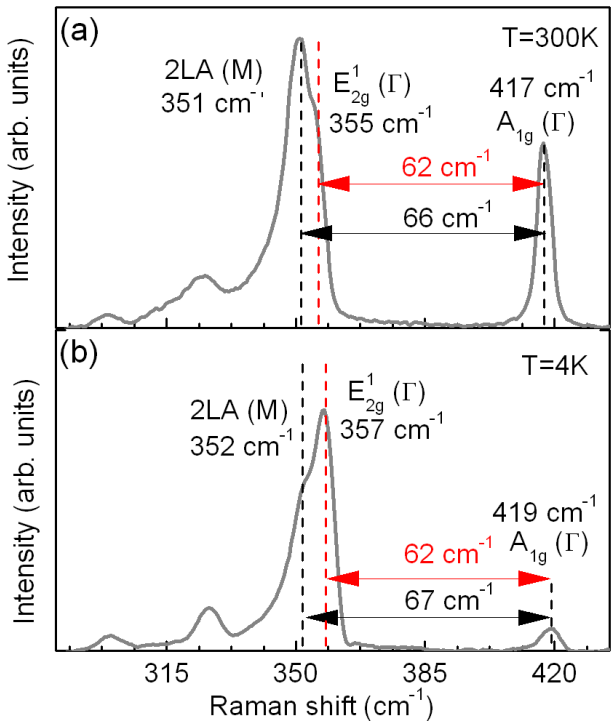

Figure 5.9: (a), (b) Typical μRaman spectra of a monolayer WS_2 measured at room and low temperature ($T = 4$K). The dashed lines indicate the position of three Raman modes: 2LA, E^1_{2g} and A_{1g}.

at low temperature the situation is reversed. As the 2LA mode is an overtone it's temperature dependence is expected to take the form

$$[n(\omega_1, T) + 1] \times [n(\omega_2, T) + 1] \tag{5.10}$$

where $n(\omega, T) = \left(\exp\left(\frac{\hbar\omega}{kT}\right) - 1\right)^{-1}$ is the phonon occupation number for a process in which phonons with frequencies ω_1, ω_2 are absorbed and created respectively [Chen 1974]. A quick estimation using the frequency of 2LA mode shows that it's intensity should decrease by 1.5 times between room temperature and 4K. This estimation is in a good agreement with our data with the assumption that the intensity of the E^1_{2g} mode is rather insensitive to temperature [Sourisseau 1991]. Our data is clearly **not consistent** with the assignment of the 351 cm^{-1} feature to a combination process whose temperature dependence would take the form similar to [Chen 1974]:

$$n(\omega_1, T) \times [n(\omega_2, T) + 1] \tag{5.11}$$

In such a scenario the resonance would simply vanish at 4K. The temperature dependence of the intensity of this resonance is therefore an independent proof of

it's 2LA character. We note that the variation of the direct gap with temperature could detune the resonant excitation and also in principle contribute to a decrease of the intensity of the 2LA overtone resonance. However, the phonon occupation is expected to dominate the temperature dependence.

5.4.2 Excitation-power dependence resonant Raman scattering

We have studied the resonant Raman scattering of 2LA, E^1_{2g} and A_{1g} modes as a function of excitation power of the laser. We start with the power-dependent measurements at low temperature ($T = 4$K). Four representative low-temperature Raman spectra collected at different laser powers are presented in Fig. 5.10(a). As the laser power increases, both of the Raman-active modes frequencies remain unchanged. This demonstrate that at low temperature the maximum power used does not heat locally the sample. However, to avoid the damage and any local heating to the sample and stay within a linear regime, the laser excitation power was kept below 0.5 mW.

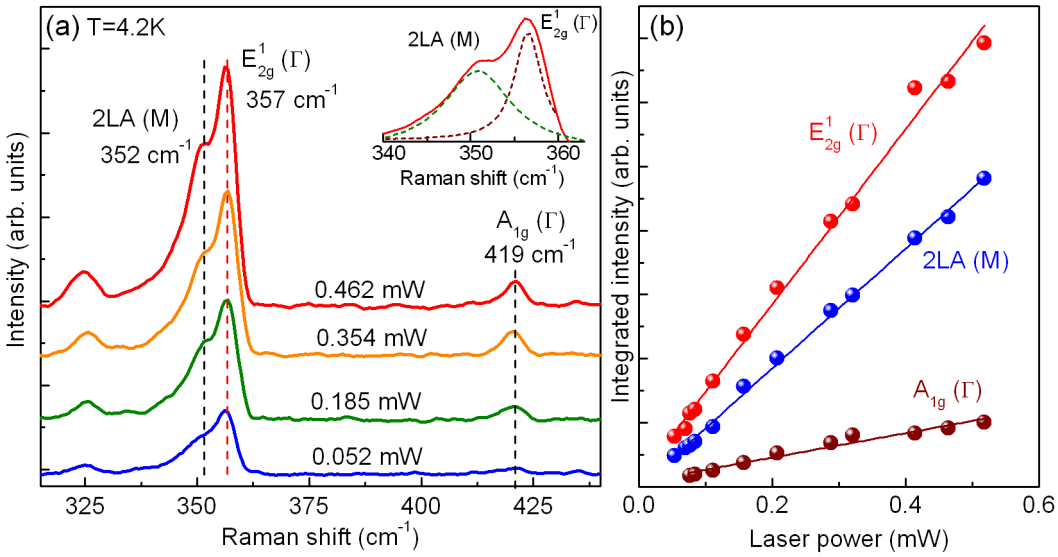

Figure 5.10: (a) Power dependence of μRaman spectra of a monolayer WS_2 measured at low temperature ($T = 4$K). Spectra are offset vertically for clarity. The dashed lines indicate the position of three Raman modes: 2LA, E^1_{2g} and A_{1g}. (b) The integrated intensity of the Raman modes at increasing excitation laser power. The lines show the results of a linear fit. In the inset is illustrated an example of the Lorentzian fitting for the 2LA and E^1_{2g} resonances at 0.462 mW excitation power.

To extract the intensity of the Raman modes a fit with a Lorentzian function was performed, as shown in the inset of the Fig. 5.10(a). Thus, the intensity of the first-order Raman-active modes, as well as of the second-order mode 2LA(M), increase linearly with the excitation power as presented in Fig. 5.10(b). A similar

linear intensity variation as a function of laser power was previously observed for ClO_4^- and A_{1g} first order bands for WS_2 bulk crystals imbedded in $KClO_4$ in order to avoid any local heating [Sourisseau 1991]. This allows us to definitively rule out the existence of a complex multi-photon processes leading to transitions originating from vibrationally and electronically excited states, since in these cases the intensity dependencies will show a saturation-like behavior [Cosse 1980].

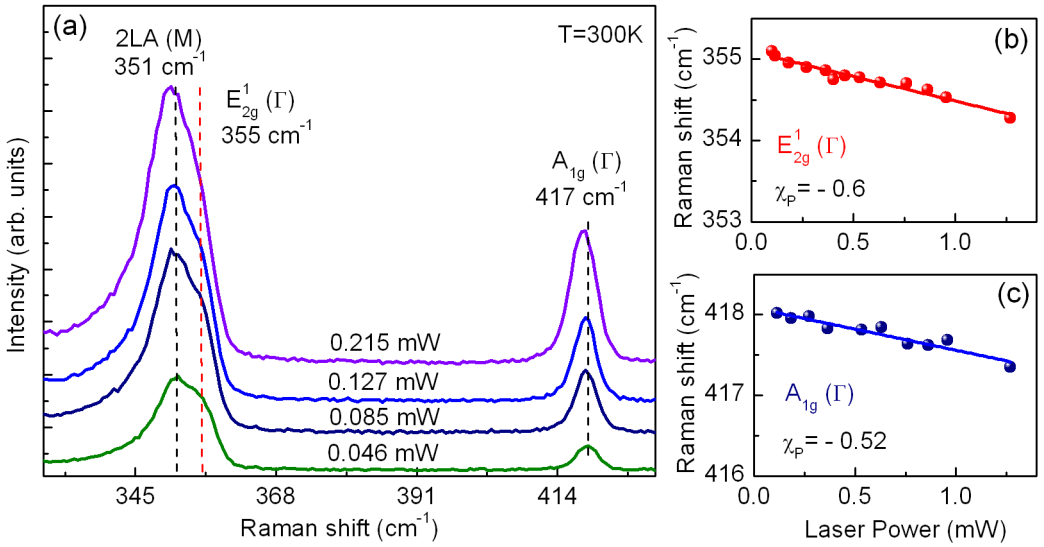

Figure 5.11: (a) Power dependence of μRaman spectra measured at room temperature ($T = 300$K). Spectra are offset vertically for clarity. The dashed lines indicate the position of three Raman modes: 2LA, E^1_{2g} and A_{1g}. (b) The Raman shifts of the modes at increasing excitation laser power. The lines show the results of a linear fit. The χ_p parameter denotes the slope of the fitting.

We have also investigated the excitation laser-power-dependent μRaman at room temperature ($T = 300$K). A strong thermal effects induced by the excitation laser power was observed in Raman spectra from substrate-supported monolayer WS_2 flakes. The characteristic Raman spectra taken for different excitation powers of the monolayer WS_2 at 300 K is shown in Fig. 5.11(a). Again, the Raman spectrum has been fitted using Lorentzian functions to extract the the intensity and position of the Raman modes. As already shown in previous subsection, at room temperature the intensity of second-order Raman mode 2LA is stronger with respect to first-order Raman mode E^1_{2g}. However, with increasing the excitation power a red-shift for both first-order Raman active modes is observed, as shown in Fig. 5.11(b) and (c). Similar behavior in the Raman frequency modes has been previously observed in a substrate-supported monolayer MoS_2 flakes [Najmaei 2012, Yan 2014]. This can be explained by local heating on the samples due to a higher temperature of the lattice using similar optical excitation powers as in low-temperature measurements.

Because of that a thermal expansion of the sample lattice and subsequently, softening of the phonon frequencies take place. The small difference in slope for out of plane (A_{1g}) and in plane (E^1_{2g}) modes presented in Fig. 5.11(b) and (c), is possibly due to a different thermal expansion coefficients of WS_2 in the two directions. Intuitively we expect that due to the large $\simeq 7$Å interlayer separation, the monolayer crystals can expand more in the out of plane than in plane direction.

5.4.3 Polarization-dependence resonant Raman scattering

In the following, we investigate the influence of the linear polarization of the excitation and detection on the intensity ratio of second-order 2LA mode to the first-order E^1_{2g} mode. μ-Raman spectra have been measured at $T = 4.2$K as a function of the relative angle θ between the linearly polarized excitation and the emission. We have performed measurements when the linear polarization of the excitation was fixed and the angle was varied in the detection and vice versa. We have verified that the results are only dependent on the angle θ; the same Raman spectra are always observed for co linearly polarized beams in excitation and detection independently of the angle of the linear polarization with respect to the sample. Also, similar spectra are observed for the cross polarized configuration. Typical results are presented in Fig 5.12(a) for frequencies in the region corresponding to the 2LA and E^1_{2g} modes and in Fig 5.12(b) for the A_{1g} mode. The spectra for different angles are shifted vertically for clarity. The spectra for co and cross polarized configuration are indicated by thick red lines. The intensity of the 2LA mode changes as a function of the angle θ. When the polarization of the excitation and detection are orthogonal, the intensity of 2LA phonon resonance reaches a minimum. For parallel configuration the 2LA mode is stronger than E^1_{2g}. For angles $0 < \theta < 90$ degrees the intensity of 2LA mode changes gradually. A similar behavior is observed for A_{1g} mode while the intensity of E^1_{2g} is constant within experimental error.

To better visualize this effect, we have extracted the intensity of the 2LA, E^1_{2g} and A_{1g} modes as a function of θ by fitting with Lorentzian functions. The intensities of the Raman peaks as a function of the angle between polarization of the excitation and detection are presented in Fig 5.13. The linear polarization in detection was fixed, either horizontal or vertical as indicated by the red arrows on Fig 5.13(a)-(b). The polarization of the excitation was then rotated through 180^0. The co and cross polarized configurations are indicated by the arrows in Fig 5.13(a)-(b). The black arrow represent the orientation of the polarization of the excitation. The data obtained for horizontal and vertical configurations are presented in Fig 5.13(a)-(b) respectively. The experimental values of the intensity of 2LA and A_{1g} modes are indicated by symbols. The data is well described by a $\cos^2\theta$ function (solid line). The minimum of the intensity of both modes for horizontally polarized detection is shifted by 90 degrees with respect to the results for the vertically polarized detection. This proves that the ratio between 2LA and E^1_{2g} depends only on the angle θ between the excitation and detection polarization. For the A_{1g} mode the oscillation of the intensity as a function of the angle θ, as well as the lack of intensity

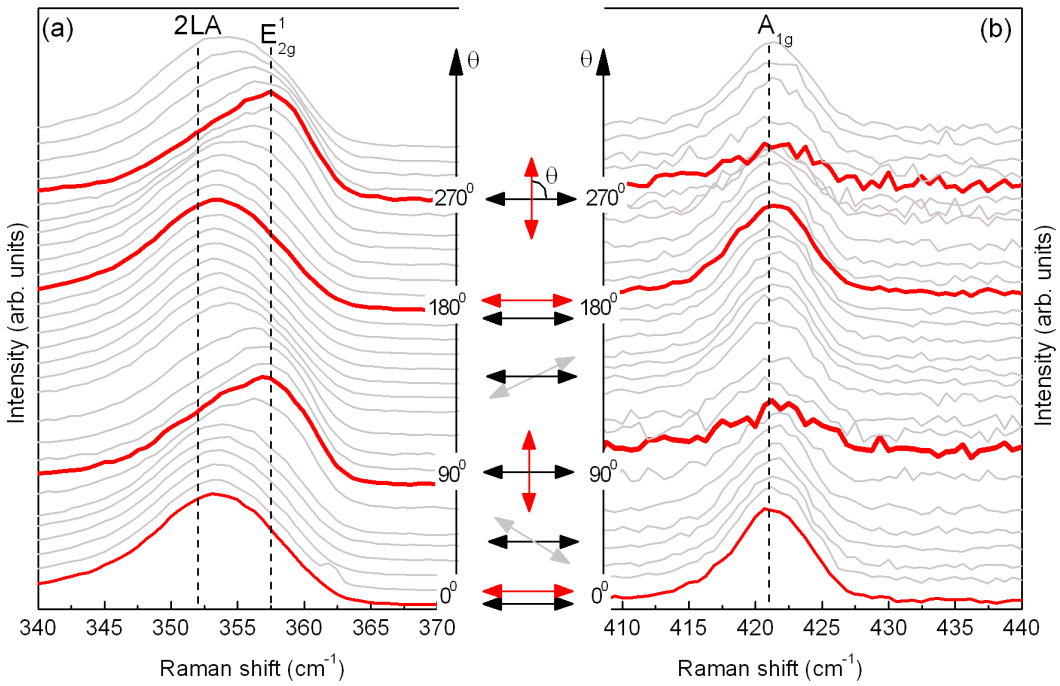

Figure 5.12: Typical results are presented in (a) for the frequency region corresponding to the 2LA and E^1_{2g} modes and in (b) for the A_{1g} mode. The spectra for different angles θ are vertically shifted for clarity. The spectra for co and cross polarized configuration are indicated by thick red lines. The orientation of the detection (red arrows) and excitation (black arrows) linear polarization are indicated for the co and cross polarization configuration.

changes of E^1_{2g} (Fig 5.13(c)) is understood and comes from the form of Raman tensors [Loudon 1964].

The in plane mode E^1_{2g} is doubly degenerate and can vibrate in x-y directions. The out of plane A_{1g} mode in non-degenerate. The Raman tensor assumes well-defined forms:

$$\alpha_j^{A_{1g}} = \begin{pmatrix} b & 0 & 0 \\ 0 & b & 0 \\ 0 & 0 & c \end{pmatrix}, \alpha_j^{E_{2g}} = \begin{pmatrix} 0 & a & 0 \\ a & 0 & 0 \\ 0 & 0 & 0 \end{pmatrix}, \begin{pmatrix} a & 0 & 0 \\ 0 & -a & 0 \\ 0 & 0 & 0 \end{pmatrix} \tag{5.12}$$

where, a, b and c are major terms in the Raman tensors of the Raman active modes with different symmetry and reflect the physics of interaction between light and crystal lattice. Due to symmetry, the other terms are negligible and are noted as 0. Using the above Raman tensors, the intensity of the Raman modes can be calculated

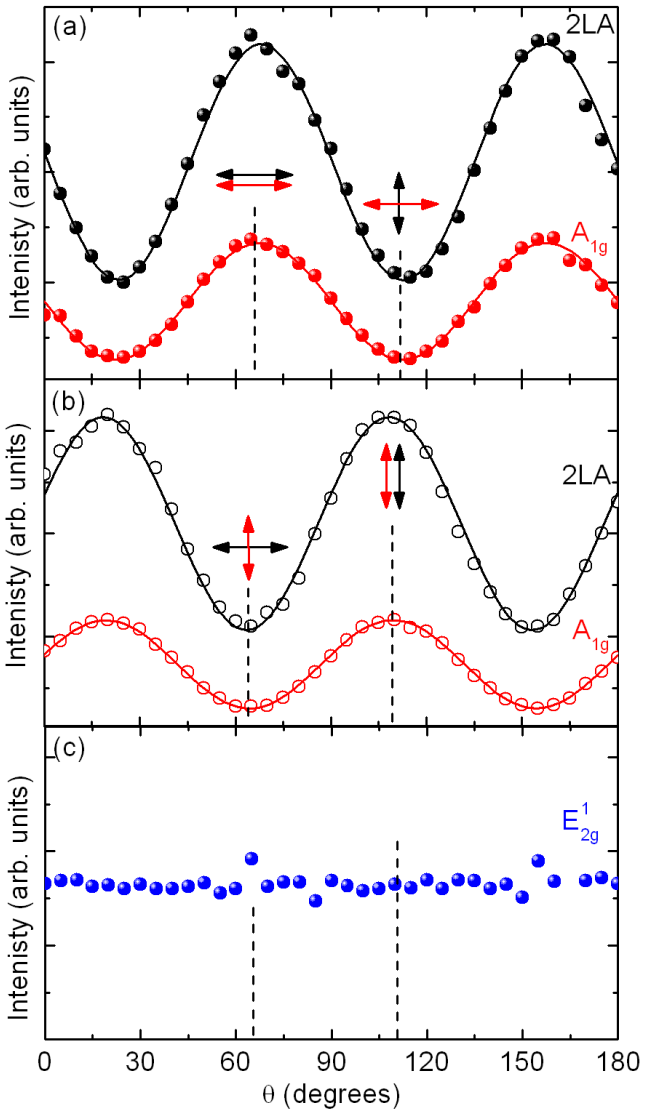

Figure 5.13: Intensity of the 2LA, A_{1g} and E^1_{2g} modes (symbols). (a), (b) represent two different experimental configurations; the linear polarization in detection was either horizontal or vertical as indicated by the red arrows. (c) illustrates the intensity dependence of E^1_{2g} mode. The black arrows indicated the excitation polarization in the co and crossed configurations.

$$I \propto |\mathbf{g}_s \cdot \alpha_j \cdot \mathbf{g}_i|^2 \tag{5.13}$$

where $\mathbf{g}_i$ and $\mathbf{g}_s$ are the polarization vectors of the incident and scattered light. Considering that the linear polarization of the excitation was fixed and the angle was varied in detection, *i.e.* is arbitrary. The polarization vectors are $\mathbf{g}_i = (1, 0, 0)$ and $\mathbf{g}_s = (cos\theta, sin\theta, 0)$, respectively. Hence, the intensity of the A_{1g} mode becomes

$$I_{A_{1g}} \propto \left| (cos\theta, sin\theta, 0) \begin{pmatrix} b & 0 & 0 \\ 0 & b & 0 \\ 0 & 0 & c \end{pmatrix} \begin{pmatrix} 1 \\ 0 \\ 0 \end{pmatrix} \right|^2 \propto |(b \cdot cos\theta)|^2 \tag{5.14}$$

Therefore, when the polarization angle θ is varied from 0 to 90 degrees, the intensity of the A_{1g} mode monotonically decreases from maximum to zero.

Similar matrix operations can be performed for E^1_{2g} Raman-active mode. Thus, we have $I_{E^1_{2g}-x} \propto a^2 sin^2\theta$, $I_{E^1_{2g}-y} \propto a^2 cos^2\theta$, $I_{E^1_{2g}} = I_{E^1_{2g}-x} + I_{E^1_{2g}-y} \propto a^2$. Therefore, the intensity of E^1_{2g} mode is independent on θ and unchanged when θ is varied from from 0 to 90 degrees, which is consistent with our experimental results. The analysis for the 2LA mode is not as straightforward as that of the A_{1g}, since the 2LA mode arises from a double resonance process. However, it is experimentally well established that the A_{1g} and 2LA modes have the same polarization dependence. For example, the polarization characteristic of 2LA mode has been determined in bulk crystals [Sourisseau 1989, Sourisseau 1991, Sekine 1980] where it was compared with the results of neutron scattering where the phonon dispersion along crystal axis was measured in the same plane as the polarization of the light. As already demonstrated by Chen *et al.* [Chen 2014] a single layer, exhibits the same polarization characteristic.

5.5 Assigning layer thickness in WS_2 flakes

Finally, we focus on the analysis of the separation between these three resonances which is crucial for layer assignment. Regardless of the temperature, the separation between A_{1g} and E^1_{2g} is 62 cm^{-1} and the separation between A_{1g} and 2LA is 66 cm^{-1}. The separation between the 2LA and E^1_{2g} modes is only 4cm^{-1} so that, any broadening of the peaks due to impurities/defects in the sample or simply a lack of resolution might lead to an incorrect determination of the frequency of the E^1_{2g} mode. As a result, the separation between A_{1g} and E^1_{2g} might be overestimated, in turn leading to an overestimation of the number of layers in the sample. To illustrate the universality of this problem, we have measured Raman spectra for several monolayer flakes in order to analyze the separation $\Delta\omega$ between different Raman features. The summary of such an analysis is presented in Fig. 5.14.

The symbols correspond to the three different combinations:

$$\Delta\omega_1 = \omega(A_{1g}) - \omega(2LA) \tag{5.15}$$

$$\Delta\omega_2 = \omega(A_{1g}) - \frac{\omega(2LA) + \omega(E^1_{2g})}{2} \tag{5.16}$$

$$\Delta\omega_3 = \omega(A_{1g}) - \omega(E^1_{2g}) \tag{5.17}$$

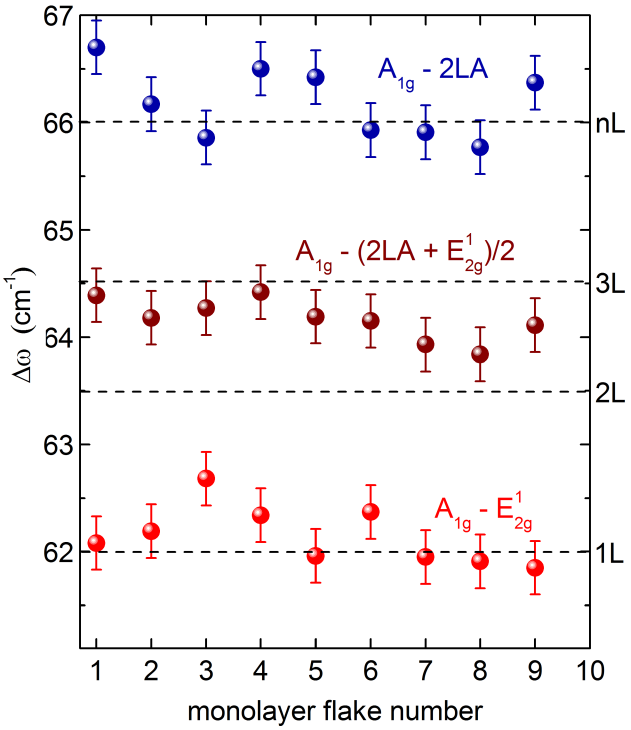

Figure 5.14: The symbols indicate the frequency difference $\Delta\omega$ between: A_{1g} and $2LA$, between A_{1g} and the average frequency of $2LA$ and E^1_{2g}, and between A_{1g} and E^1_{2g}. The dashed lines indicate the accepted values for the separation of A_{1g} and E^1_{2g} for mono-, bi -, tri-layer and bulk [Molina-Sanchez 2011, Berkdemir 2013, Zhao 2013].

The Raman splitting $\Delta\omega_3$ is generally used in the literature to determine the number of layers present. For comparison, the literature values for the separation between (A_{1g} and E^1_{2g} for mono-, bi -, tri-layer and bulk [Molina-Sanchez 2011, Berkdemir 2013, Zhao 2013] are indicated by broken lines.

For our data, in which E^1_{2g} and 2LA are clearly resolved, for all the flakes, $\Delta\omega_3$ is equal to 62cm^{-1}, demonstrating the single layer character of our flakes [Molina-Sanchez 2011, Berkdemir 2013, Zhao 2013]. However, if the modes E^1_{2g} and 2LA are not well resolved, in any analysis which neglects the possible presence of the 2LA mode the assignment of the number of layers becomes problematic. If the 2LA mode dominates over E^1_{2g} the measured difference will correspond to the $\Delta\omega_1 = \omega(A_{1g}) - \omega(2LA)$ which is approximately 66cm^{-1}, leading to the incorrect assignment of Raman from a bulk sample [Sourisseau 1989, Sourisseau 1991, Sekine 1980]. On the other hand, if the intensity of 2LA and E^1_{2g} modes are similar, the frequency of the Raman features will correspond to the average of the two peaks. The measured frequency difference $\omega(A_{1g}) - (\omega(2LA) + \omega(E^1_{2g}))/2 \simeq 64\text{cm}^{-1}$ then correspond to the bi- or tri-layer system [Molina-Sanchez 2011, Berkdemir 2013, Zhao 2013].

This poses a significant problem for the correct assignment of the number of layers especially since the relative intensity between between E^1_{2g} and 2LA depends on several parameters, including the temperature and the excitation wavelength (2LA is only observed for resonant excitation) as shown for bulk crystals [Sourisseau 1991, Sourisseau 1989].

5.6 Conclusion

In this chapter, we have studied the Raman spectra of monolayer WS_2. We focused on properties of three features: the E^1_{2g} and A_{1g} first order Raman modes, and the second order 2LA mode visible under resonant conditions. The presence of the 2LA Raman mode complicates the determination of the number of layers in WS_2 flakes. Thankfully, the assignment of a monolayer from the E^1_{2g}-A_{1g} separation remains robust. However, mono layers can be incorrectly assigned to bi-layer, tri-layer or even bulk crystals depending on the intensity of the 2LA mode. All our data has been taken using 532nm excitation, nevertheless, our conclusions should apply to other excitation wavelengths. Sourisseau *et al.* [Sourisseau 1989, Sourisseau 1991] studied in detail the dependence of the intensity of 2LA mode as a function of excitation wavelength. They have shown, that whenever the laser is in resonance with the excitonic transition (A, B or C) both the 2LA and the A_{1g} modes are enhanced. Thus, these conclusions and analysis will be valid whenever the 2LA mode is present in the Raman spectrum, in other words whenever the laser is in resonance with one of the excitonic transitions. The evolution of the intensity ratio of the 2LA and E^1_{2g}-A_{1g} modes with polarization prescribes using the intensity of the 2LA mode to identify a monolayer, unless the polarization angle between excitation and detection is carefully controlled, which is rarely the case. As many Raman characterizations are frequently performed close to resonant excitation, and without controlling the polarization angle, considerable care should be exercised when analyzing these spectra.

Chapter 6

Valley dynamics of excitons in monolayer WSe_2

Contents

In this chapter, the preliminary results of low-temperature time-resolved photoluminescence measurements to probe the dynamics of neutral and charged excitons in monolayer WSe_2 are presented. We find that the dynamics of charged and neutral excitons are independent due to the direct generation of charged excitons following a photon absorption under quasi resonant excitation. Time-resolved circularly-polarized μPL provides a direct access to the inter valley scattering of excitons. Using a rate equations model, compatible with the recent theory of valley depolarization based on electron-hole exchange, we evaluate the inter valley scattering time. Finally, the results of power-dependent valley dynamics are discussed.

6.1 Introduction

One of the first results on two-dimensional monolayer dichalcogenides that has triggered such a popularity of the dichalcogenides was the discovery of a valley polarization, which can be manipulated using circularly polarized light. Steady-state polarization-resolved photoluminescence suggest a polarization decay time $\tau_{\mathrm{iv}} > 1\mathrm{ns}$ [Mak 2012, Zeng 2012]. The polarization decay time reflects the stability of valley-polarized states and thus, is important for development of novel valleytronics devices. The degree of circular polarization P_{circ} is determined by the initially created polarization P_0, the exciton photoluminescence decay τ and inter valley scattering time τ_{iv} [Mak 2012]:

$$P_{circ} = \frac{P_0}{1 + \tau/\tau_{\mathrm{iv}}}$$

It is not clear to what extent the inter valley scattering time τ_{iv} value evaluated from steady-state PL measurements [Mak 2012] is close to the genuine value, since it was not directly measured but roughly estimated assuming the exciton lifetime to be >50ps and the degree of circular polarization to be 100%. Because in most of the monolayer dichalcogenides samples reported in the literature to date these parameters, exciton lifetime and degree of circular polarization, are much smaller [Kioseoglou 2012, Cao 2012, Jones 2013, Wang 2013], a detailed understanding of the exciton spin dynamics and valley/spin relaxation processes is crucial.

Using time-resolved techniques several groups have studied the exciton dynamics in monolayer transition metal dichalcogenides. In particular, polarization resolved pump-probe spectroscopy revealed the decay of the circular dichroism occurring on a timescale in the range between a few and almost 100 ps [Wang 2013, Mai 2014a, Mai 2014b, Zhu 2014]. The proposed mechanism underlying the loss of valley polarization is the long range electron-hole exchange interaction, which couples the bright exciton states [Mai 2014b, Yu 2014b, Glazov 2014].

In this chapter, we investigate the exciton dynamics and inter valley exciton relaxation in monolayer WSe_2 *via* time- and polarization-resolved photoluminescence measurements. We start with the analysis of the trion dissociation energy and discuss the possible trion formation scenarios. Then, we show that the valley polarization created with a pulsed, quasi-resonant, circularly polarized excitation decays due to the transfer of the excitons and trions between the valleys. The respective inter valley scattering times extracted using a rate equation model demonstrate that the scattering of trions occurs faster than for the neutral excitons.

6.2 Time-resolved μPL in monolayer WSe_2

Here we present our investigation of time-resolved μPL in monolayer WSe_2. In our time-resolved μPL measurements, the PL was excited using a femtosecond pulses generated by a tunable frequency-doubled OPO emitting at $\lambda = 670$nm (E=1850 meV), which is close to resonance with the direct excitonic transition A. This translates into $E_k \approx 120$meV excess kinetic energy. The excess kinetic energy plays an important role according to the recent theory of valley depolarization in monolayer dichalcogenides [Yu 2014b]. Under quasi resonant excitation, the excitons are generated with a non-zero center-of-mass momentum resulting from the excess energy E_k and thus, an efficient depolarization takes place due to the long-range exchange interaction. The circular degree of polarization is therefore strongly dependent on the excitation energy [Kioseoglou 2012].

Figure 6.1(a) shows steady-state μPL spectrum for WSe_2 monolayer which subsequently was measured in the time-resolved set-up. The emission from trion (X^-) dominates over the exciton (X) emission due to the excess carriers which are photoionized from the neutral donors. The dynamic response of neutral exciton depends on concentration of excess carriers, which in our samples changes under external illumination. For example, by changing the excitation power we can tune

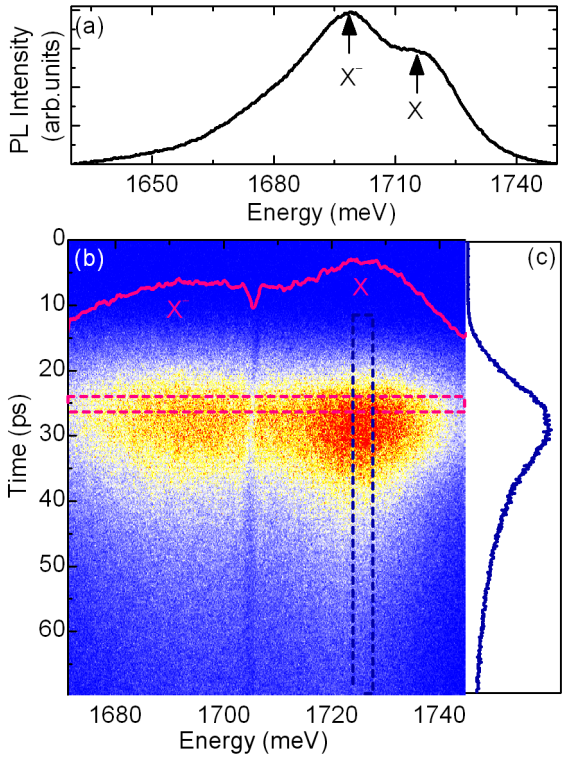

Figure 6.1: (a) Steady state μPL spectra of a WSe_2 monolayer measured at $T = 4$ K. (b) Streak camera image of time-resolved μPL showing different emission times for neutral exciton (X) and trion (X^-). (c) Vertical cross-section shows the rise- and decay-time of the neutral exciton.

the trion/exciton intensity ratio. In the range of the excitation powers used in our experiment, the density of photo excited free carriers (estimated from the change in the trion dissociation energy) can be tuned between 0 and 3×10^{12} cm^{-2}. In Figure 6.1(b) is sketched the time-resolved μPL spectrum measured at $T = 4$K (on the same flake) using the streak camera. The spectrum is obtained by taking a cross section at a certain time illustrated here in the streak PL image by the red-dashed rectangle. The time-evolution of a particular wavelength or spectrum can be obtained by taking the cross section at a particular wavelength region. Figure 6.1(c) shows the time evolution of photoluminescence for the neutral exciton (X) for the cross section indicated by a blue-dashed rectangle.

In Figure 6.2, we plot the experimental photoluminescence decays (symbols) for neutral exciton and trion at low excitation power summed over the two detection polarizations. To extract the decay times, we fit the measured signals with a convolution of a bi-exponential decay and a Gaussian laser temporal profile. The fitted long decay time is the same for the exciton and trion and equal to $t_{\text{long}} = 75 \pm 5$ ps. A similar decay time has been previously observed and attributed to a phonon

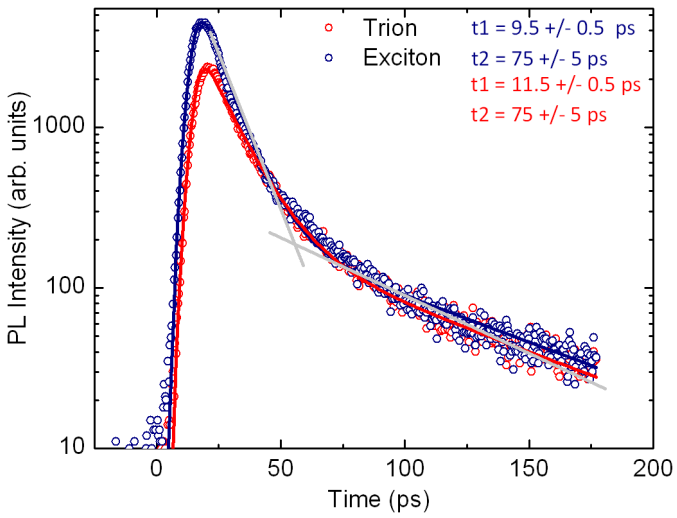

Figure 6.2: Temporal evolution of the exciton and trion emission for a WSe_2 monolayer. Blue (red) points denote the experimental data. The solid lines are the result of fitting with a bi-exponential decay convoluted with a Gaussian laser temporal profile. The straight gray lines show the time ranges for the short and long decays.

scattering process. Our time-resolved μPL measurements have been performed at low temperature and thus, allows us to rule out this process. However, we believe that the t_{long} is due to a transfer process of excitons from localized and/or dark states, which is in agreement with the results of Wang et al. [Wang 2014]. The short decays, which is attributed to inter valley scattering, are $t_{\text{X}} = 9.5 \pm 0.5$ ps and $t_{\text{T}} = 11.5 \pm 0.5$ ps, for the exciton and trion, respectively.

6.2.1 Polarization-resolved valley dynamics

Among all the scattering mechanisms present in traditional semiconductors, of particular interest for 2D monolayer dichalcogenides physics is the inter valley scattering mechanism. In order to analyze the inter valley scattering we have performed time-resolved measurements using circularly polarized excitation and detection. Typical circular polarization results for neutral and charged exciton are presented in Fig. 6.3. Due to contrasting selection rules, by using σ^+ (σ^-) polarized light, we excite electron-hole pairs only in **K**+ (**K-**) valley. Circularly polarized detection is used to discriminate the emission from each valley. The results for $\sigma^{\pm}$ polarized detection are shown in Fig.6.3(a) and (b) for the exciton and trion, respectively using σ^- excitation. Independently on the polarization of the excitation we observe a similar trend for co and cross polarized emission. It is clearly seen in Fig.6.3 that for both PL signals the co-polarized emission is stronger than the counter-polarized one. This is an indication of the valley selective optical dichroism [Xu 2014, Cao 2012, Mak 2012, Zeng 2012]. After fitting the measured signals with

a convolution of a bi-exponential decay and a Gaussian laser temporal profile we obtained aproximately the same decay time for the exciton and trion.

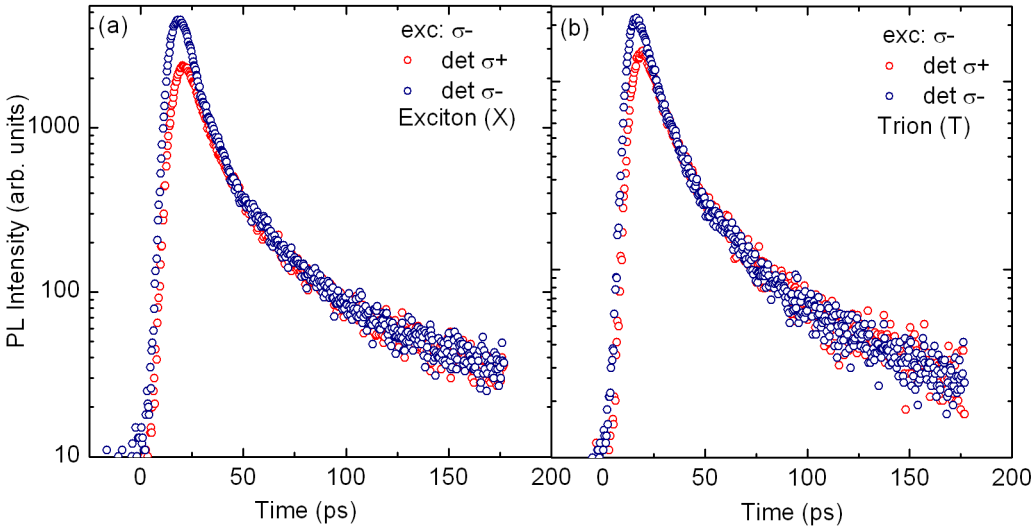

Figure 6.3: (a) and (b) Temporal evolution of the neutral exciton and trion PL excited with a σ^- circularly polarized laser for a WSe_2 monolayer. Blue (red) points denote σ^- (σ^+) polarized PL signal.

The roughly equal decay rates of the exciton and trion PL could point to a specific hierarchy of the recombination times and the trion formation time. In the case of quantum wells, the dominant trion formation scenario involves an exciton binding the additional charge [Vanelle 2000]. As demonstrated for quantum wells under quasi resonant excitation [Kossacki 2002], if the trion radiative rate is much faster than both the trion formation and exciton recombination, both complexes exhibit the same PL decay with a characteristic rate $1/\tau_{\mathrm{decay,X}} = 1/t_f + 1/t_{\mathrm{rad,X}}$, where t_f and $t_{\mathrm{rad,X}}$ are the trion formation time and the exciton radiative recombination time, respectively. Thus, the exciton dynamics govern the temporal behavior of both emissions. In such a case, the decay of the optically induced circular polarization would also exhibit the same decay time for the exciton and trion. However, as seen in Fig. 6.4(a), this is not the case. We therefore conclude that the trion formation in WSe_2 does not involve the exciton state and the complex is formed in a *tri-molecular process*. Indeed, such a mechanism proved to be important in quantum wells with a large concentration of free carriers [Portella-Oberli 2009]. As we know from our power-dependent μPL measurements the density of excess carriers in our WSe_2 sample is large, the above discussion allows us to conclude that the fitted values of t_{X} and t_{T} represent, respectively, the exciton and trion decay times related to radiative recombination or transfer of excitons to the non-radiative states. Thus, in principle the value of 10 ps sets the lower limit for the intrinsic ra-

diative recombination time, in agreement with other reports on WSe_2 [Wang 2014] and other dichalcogenides [Korn 2011, Lagarde 2014]. However, recent calculations show that the intrinsic exciton lifetime in WSe_2 at 4 K is equal to about 4 ps and increases sharply with temperature [Palummo 2015]. Taking into account that exciton lifetime $1/\tau = 1/\tau_r + 1/\tau_{nr}$, we conclude that the initial PL decay is mostly due to radiative recombination.

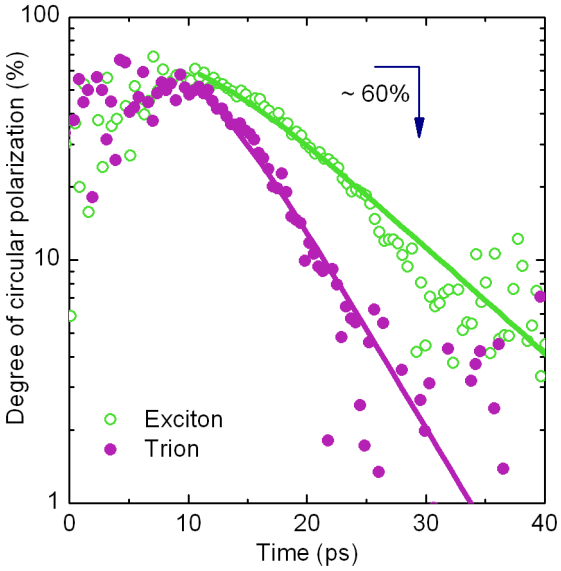

Figure 6.4: Temporal dependence of the circular polarization of exciton and trion PL for the short time range. Lines: results of fitting of a rate equations model. The fitted parameters, respectively for the exciton and trion PL, are: $p = 0.81; 0.78$, $t_{\mathrm{rec}} = 9; 11$ ps, and $t_{\mathrm{iv}} = 20; 11$ ps.

To extract the inter-valley scattering dynamics, we analyze the degree of circular polarization of the time-resolved PL signal defined as $P_{circ} = (I_{\sigma^+} - I_{\sigma^-})/(I_{\sigma^+} + I_{\sigma^-})$, where $I^{\pm}$ are the intensities of the PL signal in $\sigma^{\pm}$ polarizations. The temporal dependence of P_{circ}, plotted as symbols in Figure 6.4, shows that during the arrival of the excitation pulse, the P_{circ} is approximately constant, with a value of about 60%. P_{circ} starts to decay after a delay of about 10 ps. The decay is non-exponential and quicker for the trion than for the neutral exciton, and after about 35 ps, P_{circ} vanishes. Note that the scattered points seen in Fig.6.4 suggesting a non-zero background actually result from the logarithmic scale.

6.2.2 Rate equation model

Here we consider as an example, the case of $\sigma(-)$ excitation. Since the excitation is quasi resonant and $\sigma(-)$ polarized, due to the valley contrasting selection rules, the excitons are formed uniquely in the **K-** valley. However, since the excitons are created with a non-zero center-of-mass momentum k resulting from the

excess energy (shown in Fig.6.5 as E_k), an efficient depolarization process governed by the long-range exchange interaction takes place. Namely, the long-range electron-hole exchange, which can be treated as a source of an effective, momentum-dependent magnetic field $\mathbf{\Omega}$ [Yu 2014b], induces a precession of the valley pseudospin around $\mathbf{\Omega}$ and momentum scattering events result in valley relaxation by the mechanism proposed for quantum well excitons [Maialle 1993]. Since $\mathbf{\Omega} \sim k$ [Yu 2014b], the PL circular polarization exhibits a strong dependence on the excitation energy [Kioseoglou 2012, Wang 2015]. In particular, for the values of E_k from our experiments, an initial depolarization time of the order of 10 fs is expected [Yu 2014b]. After thermalization and subsequent cooling, which occur during the first 0.5 ps after excitation, the average k value of the exciton population is reduced and, consequently, the valley depolarization is slowed down.

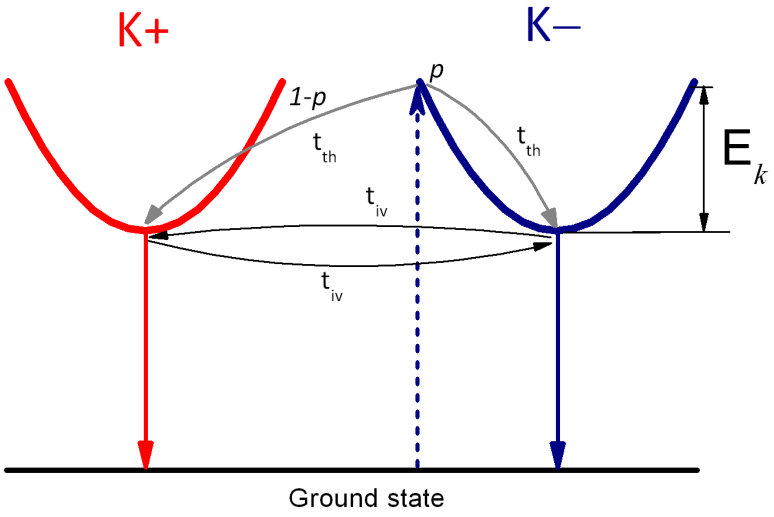

Figure 6.5: Schematic illustration of the rate equation model. Valley selective excitation is denoted by the dashed arrow. Thermalization and initial depolarization of high momentum excitons is marked by grey arrows. $E_k \approx 120$meV is the excess kinetic energy after exciting with 1850 meV. Inter valley scattering and recombination is denoted as thin and thick arrows, respectively.

In order to reproduce the measured temporal dependence of P_{circ} and to phenomenologically extract the valley scattering times, we employ a rate equation model schematically depicted in Fig. 6.5. The excitons created with the excess kinetic energy thermalize with a characteristic time t_{th}. The initial, fast depolarization process is accounted for by introducing a probability $p \lesssim 1$ of finding an exciton at the bottom of the **K-** valley. This parameter controls the initial value of P_{circ}. The thermalized excitons then recombine with a characteristic time t_{rec} or scatter to the neighboring valley with a time t_{iv}. Since the electron-hole exchange couples only bright exciton states [Yu 2014b], only two states are involved in the inter-valley

scattering, *i.e.* we neglect the dark configurations with parallel electron and hole spins. We recall that in the case of the negative charged exciton, there are six bright spin/valley configurations split by both electron-hole and electron-electron exchange interactions (see Fig.1.12). Since the splitting between the ground and the first excited trion configuration is about 6 meV [Yu 2014a], which is an order of magnitude larger than the thermal energy, we assume that only the ground configuration is populated and neglect the higher energy states.

Solving a set of three coupled, linear differential rate equations allow us to extract the expressions for the population of excitons in the **K**+ and **K-** valleys (n_{K^-} and n_{K^-}). The rate equations for the neutral exciton populations at the **K**+ and **K-** valleys are as follow:

$$\frac{dn_{\mathrm{x}}}{dt} = -\frac{n_{\mathrm{x}}}{t_{\mathrm{th}}}, \tag{6.1}$$

$$\frac{dn_{K^-}}{dt} = p\frac{n_{\mathrm{x}}}{t_{\mathrm{th}}} - \frac{n_{K^-}}{t_{\mathrm{rec}}} - \frac{n_{K^-}}{t_{\mathrm{iv}}} + \frac{n_{K^+}}{t_{\mathrm{iv}}}, \tag{6.2}$$

$$\frac{dn_{K^+}}{dt} = (1-p)\frac{n_{\mathrm{x}}}{t_{\mathrm{th}}} - \frac{n_{K^+}}{t_{\mathrm{rec}}} - \frac{n_{K^+}}{t_{\mathrm{iv}}} + \frac{n_{K^-}}{t_{\mathrm{iv}}}. \tag{6.3}$$

Here n_{x}, denotes the initially created excitons with the a non-zero center-of-mass momentum k resulting from the excess energy E_k. Under the assumption that $n_{\mathrm{x}}(t=0) = N_0$ and $n_{K^-}(t=0) = n_{K^+}(t=0) = 0$, where N_0 is the initial photo generated exciton population.

Introducing the obtained expressions for n_{K^-} and n_{K^-} in the relation for the degree of polarization yields

$$P_{circ} = \frac{exp\,(t/t_{\mathrm{rec}})\,(exp\,(t\,(-2/t_{\mathrm{iv}} - 1/t_{\mathrm{rec}} + 1/t_{\mathrm{th}})) - 1)\,(2\times p - 1)t_{\mathrm{iv}}(t_{\mathrm{rec}} - t_{\mathrm{th}})}{(exp\,(t/t_{\mathrm{rec}}) - exp\,(t/t_{\mathrm{th}}))\,(2\times t_{\mathrm{rec}}\times t_{\mathrm{th}} + t_{\mathrm{iv}}\times(t_{\mathrm{th}} - t_{\mathrm{rec}}))}$$

which we use to fit the measured data of the P_{circ} temporal dependence (Fig.6.4).

In a similar manner, the rate equations for the charged excitons population are obtained. As argued above, the dynamics of charged and neutral excitons are independent, which allows us to treat the valley depolarization of trions independently of neutral excitons. For this reason, we apply the model separately to the exciton and trion P_{circ}. The value of t_{rec} is taken from the fitting of the temporal decays (see Fig. 6.3(a) and (b)). Thus, there are three fitting parameters: p, t_{th}, and t_{iv}. Results of the fitting are presented as lines in Fig. 6.4. We find that the inter-valley scattering time for trions is significantly shorter than for excitons. Namely, for the exciton PL polarization shown in Fig. 6.4(a) we obtain $t_{\mathrm{iv}} = 20 \pm 2$ ps and for the trion $t_{\mathrm{iv}} = 11 \pm 2$ ps. On the other hand, the fitting yields very similar values of p= 0.81 and 0.78 for the exciton and trion, respectively. These results indicate that the initial depolarization dynamics occurring at high k are not very different for hot excitons and trions, while they notably differ at low k, *i.e.* for cold exciton and trion populations. This allows us to conclude that this slow depolarization process is responsible for different circular polarizations observed for the exciton and trion

PL signal. We suppose that the faster trion depolarization originates from the rich structure of trion states, mixed by both electron-hole and electron-electron exchange [Jones 2013].

6.3 Excitation-power dependence valley dynamics

We have also studied the time-resolved μPL measurements of neutral exciton and charged exciton as a function of excitation power of the laser. Four representative low-temperature experimental time-resolved μPL spectra collected at laser powers tuned from 0.3 to 3.6 mW are shown in Fig. 6.6. Similar behavior for both neutral and charged exciton can be observed in the power-dependent time-resolved spectra. As the laser power increases, both neutral and charged excitons decay times becomes shorter. In order to extract the quantitative values of the decay lifetimes, the experimental time-resolved PL curves has been fitted using two-exponential decay functions. For this temporal resolution we concentrate on the short-lived decay component. The fitting results for neutral and charged exciton at different powers showed that the short-lived components of the decay differ by $\approx$ 1ps. This difference is considered to be within the experimental uncertainties. Nevertheless, the overall change with increasing the excitation power is above this uncertainty. Thus, in Figure 6.7 we plot the overall power-dependence for both the neutral and charged exciton. It is observed that with increasing the excitation power, the short-lived component of the decay decreases down to the temporal resolution of our experiment for the highest used excitation power of 3.6 mW.

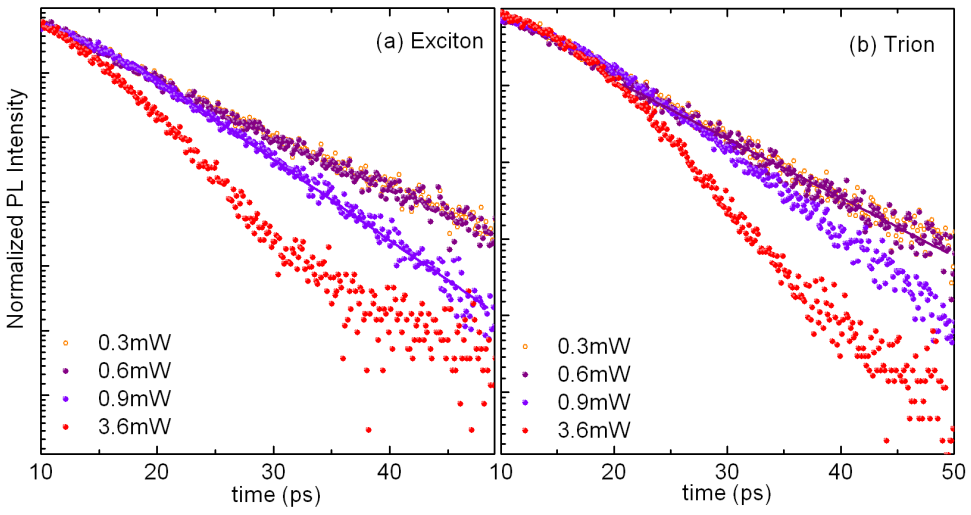

Figure 6.6: Time-resolved power dependence of neutral exciton (a) and charged exciton (b) decay times in monolayer WSe_2 measured at $T = 4$K. The lines show the results of a linear fit.

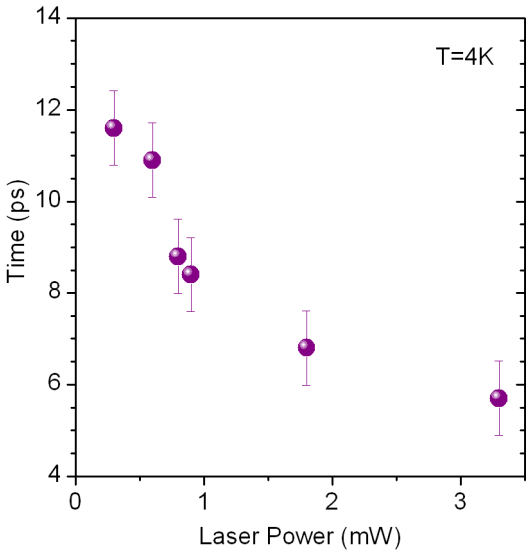

Figure 6.7: Extracted decay times for the exciton as a function of excitation power in monolayer WSe_2 measured at $T = 4$K.

Recent transient reflection spectroscopy studies on monolayer transition metal dichalcogenides suggested that the exciton dynamics is dominated by exciton-exciton annihilation [Mouri 2013, Sun 2014, Shin 2014]. Our excitation-power dependence exciton dynamics data reflect a similar behavior in which the decay times decrease with power; however, in order to confirm this hypothesis further studies are required.

6.4 Conclusion

In this chapter, we have studied time- and polarization-resolved PL in monolayer WSe_2. Although being excited in quasi resonance, a significant number of free carriers is created in our samples due to the photo ionization of the donor states. As a consequence, both charged and neutral excitons are well resolved in the PL spectrum. In the time-resolved PL measurements we observe two decays: (i) a short decay which we attribute to inter valley scattering and for the exciton and trion are $t_X = 9.5\pm0.5$ ps and $t_T = 11.5\pm0.5$ ps, respectively; and (ii) a long decay t_{long} which is due to a transfer process of excitons from localized and/or dark states. Moreover, our time-resolved PL measurements strongly suggest that the charged excitons are formed in a tri-molecular process, *i.e.*, from free independent carriers. The inter valley scattering dynamics is monitored by the PL circular polarization. Immediately after the valley selective excitation, the polarization is lower than 100% owing to an ultra fast valley depolarization of X with high center-of-mass momentum. After thermalization, the inter valley scattering slows down and the polarization decays on a timescale of 10 ps, while the X^- decays roughly twice faster.

Chapter 7

Magneto-optical study of monolayer and bulk WSe_2

Contents

In this chapter, the results of low-temperature magneto-optical studies of monolayer and bulk WSe_2 crystals are presented. Monolayer flakes were studied using micro-photoluminescence technique in dc magnetic field up to 30T. The macro-transmission through thin bulk crystals was measured in the pulsed magnetic field up to 65T. High magnetic fields data reveal the very different nature of carriers in monolayer and bulk transition metal dichalcogenides. We demonstrate that in monolayer, the carriers behave as massive Dirac fermions that can be described using a single particle picture Dirac-like Hamiltonian. In contrast, in bulk crystals the optical absorption measurements show a distinctly excitonic behavior which is best described within the 3D hydrogen model. Some of the results presented in this chapter have been accepted for publication in Nano Letters ***15 (7)****, 4387 (2015).*

7.1 Introduction

Recent theoretical and experimental studies have clearly demonstrated that the electronic properties of bulk dichalcogenides differ significantly from those of a 2D monolayer of the same material [Mak 2010, Splendiani 2010, Wang 2012, Xu 2014]. This behavior has been explained through the lowering of crystal symmetry while thinning down to the monolayer limit. The bulk dichalcogenides crystals exhibit an inversion symmetry, with the inversion center between the layers, which is explicitly

broken in 2D monolayers. This leads to **different optical selection rules** and electronic properties in bulk and monolayer systems. As in the case of recently studied boron nitride (BN), monolayer transition metal dichalcogenides host **2D massive Dirac fermions**[1] [Castro Neto 2009, Rose 2013]. Understanding the carrier nature is critical both for the elucidation of the underlying many-body physics in such materials and for their use in electronic, photonic and valleytronic devices. Using spectroscopic tools in high magnetic fields, such as micro-photoluminescence and inter-band optical absorption, it is possible to probe the nature of carriers. Although measuring magnetic field effects in monolayers is not entirely straightforward experimentally, progress is being made in this respect [Li 2014, Aivazian 2015, MacNeill 2015, Srivastava 2015]. However, direct evidence of the very different nature of the carriers in bulk and 2D monolayer transition metal dichalcogenides crystals is still lacking.

The first magneto-spectroscopy measurements on bulk layered transition metal dichalcogenides date from the late sixties. Evans and coworkers, have investigated the $n \geq 2$ excitons in MoS_2 in a weak magnetic field up to 2.7T and found a small diamagnetic shift in the studied crystals [Evans 1967]. Later, Neville et al. have studied the $n = 1$ level of the A-exciton and determined the Zeeman splitting. However, the diamagnetic shift in magnetic fields up to 10T was too small to be measured accurately [Neville 1976]. More recently, Goto et al. have performed measurements in high magnetic field up to 150T [Goto 2000]. All the published magneto-spectroscopy measurements to date concern bulk MoS_2 crystals. To the best of our knowledge, there is no published data for tungsten dichalcogenides (WS_2, WSe_2) bulk crystals.

Here, we present an experimental investigation of excitons in monolayer and bulk WSe_2 in high magnetic fields. We show that in monolayer both the exciton and the trion exhibits a splitting which originates from the lifting of the valley degeneracy by a magnetic field. Moreover, we show that magnetic field has little effect on the valley polarization of the neutral exciton, whereas it can significantly influence the valley polarization of the trion. The linear evolution of the energy of the exciton and trion features in magnetic field is described using a Dirac-like Hamiltonian for massive Dirac fermions. In bulk crystals, we see 3D excitonic behavior with absorption to the 1s and 2s hydrogen like states. Both states show a spin (Zeeman) splitting accompanied by a small diamagnetic shift at low magnetic fields.

WSe_2 is a representative member of the transition metal dichalcogenides family that includes MoS_2, $MoSe_2$, and WS_2, all of which share similar properties with respect to atomic and electronic structure. The advantage of WSe_2 for this study is the large spin-orbit splitting between the A and B excitons being of the order of 400 meV [Zeng 2013, Jones 2013, Wang 2014]. In addition, the electronic transitions in the WSe_2 samples exhibit narrow spectral features, permitting the identification and analysis of different excitonic states and detailed quantitative comparison with theoretical predictions.

[1] Dirac fermions is the name given to particles obeying the Dirac equation

7.2 Dichalcogenides in high magnetic field

To provide insight into the origin of the effects of magnetic fields in monolayer and bulk WSe_2 crystals, we first consider two theoretical models used to interpret the magneto-optical spectroscopy results. First, the massive Dirac fermion model for the carriers in 2D monolayer dichalcogenides, proposed by Rose et al. [Rose 2013], is presented. This is followed by a discussion of the hydrogen model previously used to describe the excitons in layered bulk, such as GaSe and PbI_2 [Miura 2007].

7.2.1 Massive Dirac model for monolayer crystals

A monolayer of dichalcogenides is very similar to graphene except that the two carbon atoms, that correspond to the A and B sublattices, are now transition metal (Mo, W) and chalcogen (S, Se) atoms. As a results, the 2D monolayer dichalcogenides do not have inversion symmetry. The dispersion relations of both the valence and conduction bands can be found at the **K**(+) and **K**(-) points of the hexagonal-shaped first Brillouin zone, which are parabolic at low energies and linear at high energies. The carriers in a direct gap monolayer at the vicinity of **K**($\pm$) points can be described by a simple tight binding Hamiltonian [Xiao 2012]. The carriers behave as massive Dirac fermions with a moderate spin-orbit coupling. The corresponding low energy Hamiltonian reads:

$$\hat{H} = \hbar v_F(\xi q_x \sigma_x + q_y \sigma_y) + \Delta\sigma_z \tag{7.1}$$

where v_F is the Fermi velocity (which replace the speed of light and, here is a constant independent of the carrier density), ξ labels the **K**(+) and **K**(-) valley and Δ is a half of the band gap which is also so-called "mass gap"; σ_x, σ_y and σ_z are the Pauli matrices. Unlike graphene, the $\Delta\sigma_z$ term is nonzero because of the broken inversion symmetry.

The Hamiltonian for a monolayer of dichalcogenides subjected to a magnetic field is obtain using the Peierls substitution $q \to q - eA/h$, where A is the magnetic vector potential in the Landau gauge [Rose 2013]. The energy of the carriers in the conduction and valence bands in a magnetic field perpendicular to the layer, *i.e.* the Landau level energies at **K**($\pm$) are:

$$E_\lambda^{\pm K} = \lambda\sqrt{\Delta^2 + n\varepsilon^2}, \tag{7.2}$$

where $\lambda = \pm 1$ designates the conduction/valence band, n is the Landau level index, and the characteristic magnetic energy $\varepsilon = \sqrt{2}\hbar v_F/\ell_B$. Here, v_F is the Fermi velocity and $\ell_B = (\hbar/eB)^{1/2}$ is the magnetic length which represents the radius of the cyclotron orbit of the ground state. As in graphene, in the transition metal dichalcogenides monolayer the selections rules for dipole allowed optical transitions are $\Delta n = \pm 1$, *i.e.* the Landau level index changes by one (see Fig. 7.1). In this case spin is conserved and any spin splitting of the Landau levels will not give rise to a splitting of the optical transition. Therefore, the splitting observed in magnetic

field measurements is due to the valley splitting which is generally referred to as a *valley Zeeman effect* [Xiao 2012, Li 2014, Srivastava 2015, Aivazian 2015].

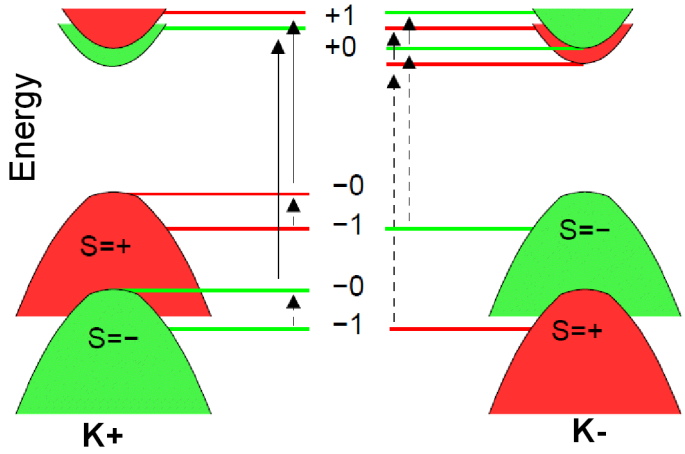

Figure 7.1: Schematic showing possible optical transition of massive Dirac fermions in a magnetic field together with the dipole allowed $0 \rightarrow 1$ and $1 \rightarrow 0$ transitions which select the valley involved (solid lines are Landau levels, solid arrows indicate the transitions). The red and green colors show the two pairs of massive Dirac cones separated by spin-orbit coupling. After Rose et al.[Rose 2013]

According to the massive Dirac fermion model [Rose 2013], the $n = 0$ level is special and there is a single $n = 0$ Landau level per valley. For both spin levels, the $n = 0$ Landau level is fixed at the top of the valence band for the $\mathbf{K}+$ valley and at the bottom of the conduction band for the $\mathbf{K}-$ valley. This is direct consequence of the fact that electrons behave as Dirac massive fermions in these systems. Figure 7.1 illustrates the possible optical transition of massive Dirac fermions in a magnetic field. The $n > 0$ Landau levels always occur in pairs with one in each valley in both the conduction and valence bands. Thus, in a magnetic field resonant $\sigma^{\pm}$ excitation selects $0 \rightarrow 1$ or $1 \rightarrow 0$ optical transitions, respectively, and therefore selecting the valley as in the zero magnetic field case.

7.2.2 Hydrogen model for layered bulk crystals

Layered semiconductor crystals such as GaSe, PbI_2 as well as TX_2 dichalcogenides, show prominent exciton effects due to the large exciton binding energy [Miura 2007]. This also reflects the large effective masses of electrons and holes compared to III-V semiconductors. An exciton is a quasi-particle in which an electron and hole are bound with each other by Coulomb interaction. The energy states of excitons resemble those of a hydrogen atom.

The difference between the exciton states in transition metal dichalcogenides and those of hydrogen atom is that the positively charged particles (holes) have a comparable mass with that of the negatively charged particles (electrons), and they

move around together in the crystal. Thus, the Hamiltonian of exciton states in a magnetic field is represented by [Knox 1963]

$$\hat{H} = \frac{1}{2m_e^*}\left(p_e + e\mathbf{A}(r_e)\right)^2 + \frac{1}{2m_h^*}\left(p_h + e\mathbf{A}(r_h)\right)^2 - \frac{e^2}{4\pi\kappa\varepsilon_0 r} = -\frac{\hbar^2}{2m_e^*}\nabla_e^2 - \frac{\hbar^2}{2m_h^*}\nabla_h^2$$

$$- \frac{e^2}{4\pi\kappa\varepsilon_0 r} + \frac{ie\hbar}{m_e^*}\mathbf{A}(r_e)\nabla_e - \frac{ie\hbar}{m_h^*}\mathbf{A}(r_h)\nabla_h + \frac{e^2}{2m_e^*}\mathbf{A}(r_e)^2 + \frac{e^2}{2m_h^*}\mathbf{A}(r_h)^2 \qquad (7.3)$$

where m_e^* and m_h^*, r_e and r_h are effective masses and position coordinate of electrons and holes. As both electrons and holes are mobile, the motion of the center of gravity should be included in the kinetic equations. Using a canonical transformation

$$\Psi(\rho, r) = exp\left(i\left[\mathbf{K} - \frac{e}{\hbar}\mathbf{A}(r)\right]\rho\right)F(r)$$

with the wave vector of the center-of-mass motion $\mathbf{K}$ of excitons we obtain:

$$\hat{H} = [\frac{\hbar^2}{2\mu}\nabla^2 - \frac{e^2}{4\pi\varepsilon r} + ie\hbar\left(\frac{1}{m_e^*} - \frac{1}{m_h^*}\right)\mathbf{A}(r)\cdot\nabla$$
$$+ \frac{e^2}{2\mu}\mathbf{A}(r)^2 - \frac{2e\hbar}{m_e^* + m_h^*}\mathbf{A}(r)\cdot\mathbf{K}]F(r) \qquad (7.4)$$

where $\mu = m_e m_h/(m_e + m_h)$ is a reduced mass of excitons and $F(r)$ is an eigenfunction.

Here, the first term represents the kinetic energy of the relative motion of electrons and holes, the second term the Coulomb potential energy between the electrons and holes, the third term the Zeeman energy of the envelope function which is zero for s-states, the fourth term the diamagnetic energy. The fifth term can be converted to the Lorentz force acting on the motion of the exciton and considered to be an effective electric field. This term is in ordinary cases very small, because of the small wave vector of the incident light to create excitons.

In addition to the orbital terms expressed in Equation 7.3, there is a spin Zeeman term

$$\hat{H}_z = g_e\mu_B s_e B + g_h\mu_B s_h B$$

where g_e, g_h, s_e, s_h are g-factors and the spins of electrons and holes. As a consequence, the degeneracy of the electronic levels is lifted (spin Zeeman splitting). As the dominant terms in Equation 7.4 are just the first and the second terms, the Hamiltonian for exciton states in a magnetic field is reduced to a problem similar to that for hydrogen atom.

There is no analytical solution for the hydrogen atom in a magnetic field. However, there are numerical calculations for the hydrogen energy levels in high magnetic field, see *e.g.* ref. [Makado 1986]. Nevertheless, for the analysis of magneto-spectroscopy data in semiconductor structures, such as quantum wells and quantum

dots, usually a simplified analytical solution can be used to describe the exciton. The evolution of the 1s and 2s exciton states in a magnetic field is phenomenologically well described by the same equation as for the ground state of a harmonic oscillator in perpendicular magnetic field:

$$\Delta E = -\frac{\hbar\omega_0}{2} + \frac{\hbar}{2}\sqrt{\omega_0^2 + \omega_c^2} \pm \frac{1}{2} g_s \mu_B B \tag{7.5}$$

Here ω_0 is the harmonic trap frequency, which controls the diamagnetic shift and $\omega_c = eB/m^*$ is the cyclotron energy. The Zeeman splitting is introduced through the second term in Eq. 7.5, where g_s is the effective g-factor. The first term is added simply for convenience so that $\Delta E = 0$ when $B = 0$.

7.3 Monolayer and bulk WSe_2 spectroscopy at B=0T

The aim of our work was to compare the character of the carriers in both bulk and monolayer WSe_2 crystals at the **K** point of the Brillouin zone. Optically this can be done by probing the exciton properties at the **K** point in these two systems. In monolayer, where the band gap becomes direct at the **K** point, the resulting strong photoluminescence emission can be used. In bulk, with an indirect band gap at the **Γ** and **T** points of the Brillouin, there is no emission at the **K** point. Therefore, the only access to A and B excitons at the **K** point in bulk crystals is *via* inter band absorption.

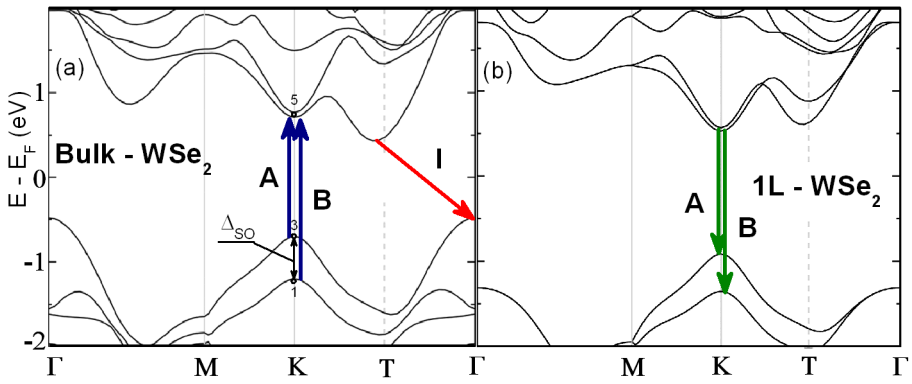

Figure 7.2: WSe_2 electronic band structure illustrating the (a) indirect and direct transition in bulk and (a) direct transition in monolayer dichalcogenides. The red arrow (left side) depicts the indirect transition (I) in bulk crystals. The blue (left side) and black arrows (right side) indicate the direct transitions (A and B) in both bulk and monolayer crystals. After Roldan et al. [Roldán 2014].

Figure 7.2 schematically illustrates the indirect (I) and direct transitions (A and B) in bulk and monolayer WSe_2 crystals. We restrict our analysis to the spectral range in the vicinity of A-exciton, which, according to [Coehoorn 1987], is the

ground state of an excitonic series (A) [Evans 1967, Neville 1976] connected with the transitions from $\mathbf{K}_1$ spin-orbit split valence band to a $\mathbf{K}_5$ conduction band.

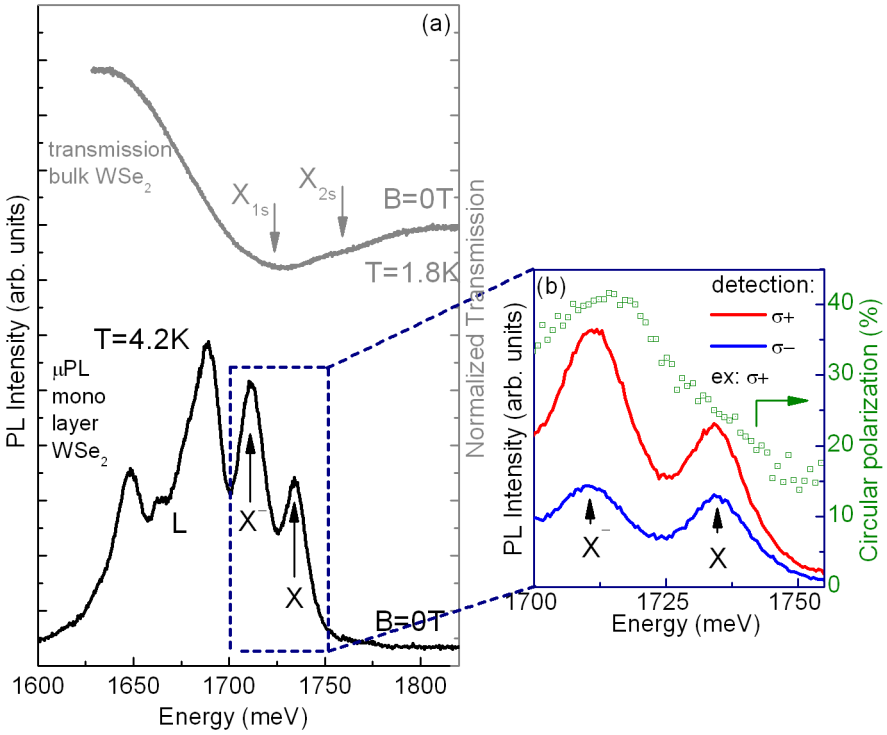

Figure 7.3: (a) Typical low temperature μPL (black color) of monolayer and transmission (gray color) spectra of bulk WSe_2. The spectra are shifted vertically for clarity. (b) Polarization resolved μPL showing the exciton and trion emission. σ^+ was used for excitation. Two spectra are shown corresponding to σ^+ and σ^- detection. The right axis indicates the degree of circular polarization (symbols) in the region of the exciton and trion emission.

We start our discussion by presenting the μPL and transmission spectrum of monolayer and bulk WSe_2 crystals. Figure 7.3(a) shows a comparison of these spectra. In both spectra we observe a strong resonance around 1730 meV which corresponds well to the energy of 1s ($n = 1$) state of the A-exciton, previously reported for monolayer [Zeng 2013, Zhao 2013, Jones 2013, Wang 2014] and bulk WSe_2 [Beal 1976, Zeng 2013]. The slightly higher energy of the A exciton emission observed in monolayer layer WSe_2 (compared to bulk transmission) is in agreement with previous studies [Zeng 2013, Zhao 2013]. On the higher energy side of the 1s resonance in the transmission spectra we observed an additional resonance. The detail analysis in magnetic field shows that it originates from the 2s ($n = 2$) exciton level, previously reported in reflectance measurements [Beal 1976]. As we have already discussed in Chapter 4, the WSe_2 monolayer exhibits several PL emission

lines that originate from the negatively charged and neutral excitons (labeled as X^- and X in Fig. 7.3). The other PL peaks labeled as "L", below the trion emission, have been assigned to localized (bound exciton) states, previously reported in WSe_2 and MoS_2 [Wang 2014, Zhu 2014, Mak 2012].

We have also verified the degree of circular polarization of the emission from monolayer WSe_2 using polarization resolved excitation and detection. The polarization is defined as $P = (I_{\sigma^+} - I_{\sigma^-})/(I_{\sigma^+} + I_{\sigma^-})$ where $I_{\sigma^\pm}$ is the intensity of the emission. For the exciton we found a circular polarization $P_{circ} = 25\%$ and for the charged exciton $P_{circ} = 40\%$. This is not surprising, as our circular excitation at $\lambda = 640$nm (E=1.93 eV) was relatively close to the exciton resonance (~ 200 meV above neutral exciton emission). Our results are in good agreement with those previously reported for WSe_2 [Jones 2013]. We will see that the degree of circular polarization depends on the magnetic field value.

7.4 Magnetic field experimental results

Let us discuss now the optical response of monolayer and bulk WSe_2 in the **presence of magnetic field**. In both μPL and transmission measurements, the magnetic field was applied in the Faraday configuration. Typical low temperature μPL spectra of monolayer WSe_2 measured in *dc* magnetic fields up to 30T are presented in Fig 7.4(a). The results of the absorption measurements through the thin layers of bulk WSe_2 measured in pulsed magnetic fields up to 65T are presented in Fig 7.4(b) using σ^+ and σ^- detection. The photoluminescence was excited using σ^+ polarization while for the transmission unpolarized white light was used for the excitation.

Already, the raw data reveals that in both bulk and monolayer crystals the polarization resolved measurements indicate a splitting of the exciton transition in magnetic field. For monolayer, the exciton splitting is of the order of ~ 8 meV at 30 T, whereas for the bulk the splitting of the same neutral exciton transition is ~ 5 meV at 65 T. This suggest a very different physical origin of the splitting due to the markedly different optical selection rules in bulk and monolayer WSe_2.

7.4.1 Monolayer WSe_2 crystals magneto-μPL analysis

The PL spectra presented in Fig. 7.4 have been fitted using two Gaussian functions to extract the integrated intensity and energy of the excitonic resonances. The results of analysis for magnetic field measurements performed on monolayer WSe_2 are presented in Fig. 7.6. Both the exciton and trion emission shifts linearly to higher energy with increasing magnetic field showing a pronounced splitting which also evolves linearly with magnetic field.

We recall that in monolayer dichalcogenides, the $n \neq 0$ Landau levels always occur in pairs with one in each valley in both the conduction and valence bands. The $n = 0$ level is different and there is a single $n = 0$ Landau level per valley. For both spin levels, the $n = 0$ Landau level in the **K**+ valley is fixed at the top of the

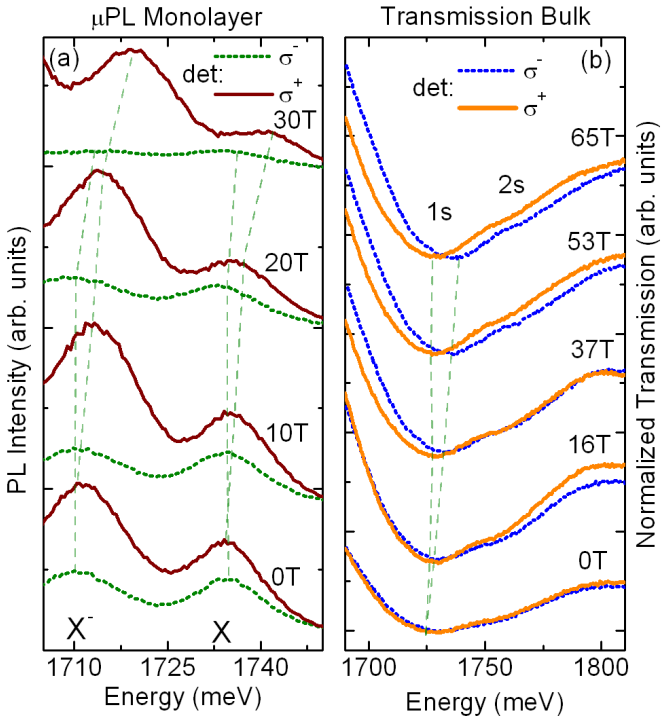

Figure 7.4: Typical low temperature spectra at various magnetic fields of (a) μPL from monolayer WSe_2 and (b) absorption of the thin WSe_2 bulk crystal, using σ^+ and σ^- detection. For the PL shown here σ^+ polarized light was used for excitation while the white light for the optical absorption measurements was unpolarized. The dashed lines are drawn as a guide for eye showing the evolution of exciton features with magnetic field. The spectra have been shifted vertically for clarity.

valence band, whereas in the **K**− valley is located at the bottom of the conduction band [Rose 2013]. Thus, in a magnetic field resonant $\sigma^{\pm}$ excitation selects $0 \rightarrow 1$ or $1 \rightarrow 0$ optical transitions, respectively, and therefore selecting the valley as in the zero magnetic field case as schematically presented in Figure 7.6.

The observed splitting of the transitions is included in the magnetic Hamiltonian simply as a phenomenological valley splitting $\pm\frac{1}{2}g_v\mu_B B$ where g_v is the effective valley g-factor:

$$E_{\lambda}^{\pm K} = \lambda\sqrt{\Delta^2 + n\varepsilon^2} \pm \frac{1}{2}g_v\mu_B B, \tag{7.6}$$

In the literature the splitting of the transition is often described, using a slightly different language, in terms of a two band tight binding model in which the atomic d-orbitals form the conduction and valence bands [Aivazian 2015, Srivastava 2015]. This first contribution to the magnetic moment of charged particles is called **intracellular** component and originates from the hybridization of the d_{xy} and $d_{x^2-y^2}$-orbitals which provide the electrons in the valence band with an in plane angular

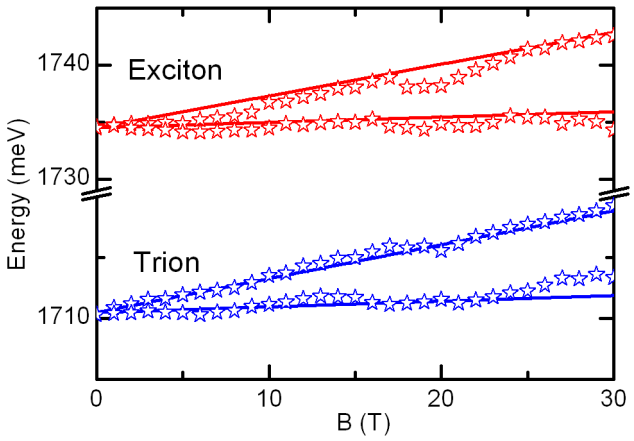

Figure 7.5: Magnetic field dependence of the energy of the polarization resolved exciton emission in monolayer WSe_2 measured at $T = 4.2$ K. The solid lines are fits to the data using the Hamiltonian for massive Dirac fermions.

momentum $m\hbar$ with $m = \pm 2$ according to the valley index. This is included in our model by the second term in Equation 7.6. The other component which contributes to the magnetic moment is called **intercellular** component. This originates from the phase winding of the Bloch functions and, in our case, it is expressed by the first term of Equation 7.6.

The solid lines in figure 7.5 are the transitions energies calculated from the energies of the $0 \rightarrow 1$ and $1 \rightarrow 0$ transitions from Equation 7.6 with a Fermi velocity $v_F = 0.51 \times 10^6$ m/s and an effective valley g-factor $g_v = 4$. The measured value of $\hbar v_F = 3.36$Å eV suggests $t = 1.02$ eV which is roughly 15% less than the effective hopping integral predicted from first principle band structure calculations [Xiao 2012, Rose 2013]. We have included excitonic effects simply by subtracting the exciton (trion) binding energy from the calculated transition energy. The parameter set provides a reasonable fit to both the exciton and trion emission data. The transition energies evolve linearly with magnetic field which can be understood as follows: The band gap of WSe_2 is large so that for the magnetic fields of interest here $\Delta^2 \gg \varepsilon^2$ and the orbital contribution to the Landau level energy is well approximated by a Taylor expansion

$$E_n = \pm\sqrt{\Delta^2 + 2n\hbar eBv_F^2} = \pm\Delta\sqrt{1 + \frac{2n\hbar eBv_F^2}{\Delta^2}} \simeq \pm\left(\Delta + \frac{n\hbar eBv_F^2}{\Delta}\right) \qquad (7.7)$$

The last term can be associated with the cyclotron energy $n\hbar\omega_c$. Thus, the carriers behave as massive Dirac fermions with an effective mass $m^* = \Delta/v_F^2 \simeq 0.7m_e$ where m_e is the free electron mass. Note, that this result can also be obtained by comparison with the Klein-Gordon equation $E^2 = m^2c^4 + p^2c^2$ replacing the speed of light with the Fermi velocity. For this reason $\Delta \equiv mc^2$ is often referred to as the "mass gap".

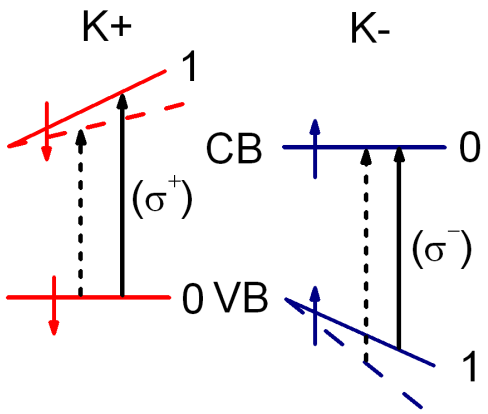

Figure 7.6: Schematic showing the dipole allowed $0 \rightarrow 1$ and $1 \rightarrow 0$ transitions which select the valley involved (solid lines are Landau levels, solid arrows indicate the transitions). Spin is conserved so that the Zeeman energy (not shown here) does not split the transition. Any asymmetry of the electron/hole Dirac cones, which modifies the energy of the $n = 1$ Landau levels, would split the transition as indicated by the dashed lines/arrows.

The observed splitting is asymmetric due to the orbital (Landau level) contribution which is always positive. The low energy peak almost does not move in magnetic field as the orbital and valley contributions are of similar size but of opposite sign. Li et al. [Li 2014] observe a symmetric splitting in MoS_2 in fields up to 10T, albeit with a somewhat smaller valley splitting of 0.12meV/T. As it is unlikely that the Fermi velocity in MoS_2 is significantly smaller than found here for WSe_2, this may suggest that the orbital contribution is quenched in their measurements, either due to the higher temperature used ($T = 10$ K) or increased disorder in their sample ($\omega_c\tau < 1$).

The valley splitting observed in our data ($g_v = 4.0 \pm 0.5$) agrees perfectly with the splitting of $4\mu_B B$ observed in the data of Srivastava and co-workers [Srivastava 2015]. A factor of two lower value ($\simeq 2\mu_B B$) has been the published recently by Aivazian and co-workers [Aivazian 2015]. In the tight binding model, the valley magnetic moment due to the self rotation of the wave packet gives no contribution to the splitting provided the electron and hole masses are identical. Aivazian *et al.* [Aivazian 2015] invoked different electron and hole masses to correctly predict the observed splitting in their samples. Similarly, in our Hamiltonian any asymmetry of the electron and hole Dirac cones would lead to a splitting of the $0 \rightarrow 1$ and $1 \rightarrow 0$ transitions (see Figure 7.6). However, as our data corresponds to the expected splitting of $4\mu_B B$, this suggest that electron-hole asymmetry in WSe_2 is small and makes no significant contribution to the observed valley splitting.

7.4.2 Bulk WSe_2 crystals magneto-optical analysis

For bulk WSe_2 crystals, the dipole selection rules are $\Delta n = 0$ [Neville 1976]. The observed splitting of the optical transitions will be a spin (Zeeman) splitting and is included in the theoretical model as a $\pm\frac{1}{2}g_s\mu_B B$ term. Figure 7.7 illustrates the scheme of the energy levels and excitonic transitions in magnetic field in bulk WSe_2 crystals. Thus, in a magnetic field the circularly polarized light $\sigma^{\pm}$ will select $0 \rightarrow 0$ optical transitions of the electron-hole pairs with an opposite spin, as shown schematically in figure 7.7.

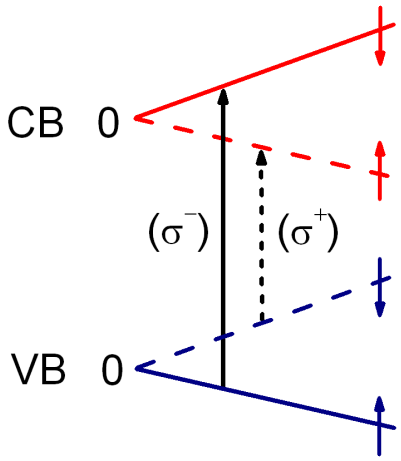

Figure 7.7: Schematic showing the energy levels and dipole allowed excitonic transitions observed in high magnetic fields measurements.

The energy of the polarization resolved exciton features in transmission for bulk WSe_2 shown in figure 7.8 clearly shows signs of excitonic effects with quadratic diamagnetic shift at low magnetic fields which becomes more linear at high fields. The diamagnetic shift in the A-exciton peak is caused by deformation of the relative motion of the electron and hole in the exciton due to the Lorentz forces. At low magnetic fields, such deformation can be treated as a perturbation. For the ground state, with an s-envelope wave function and angular momentum of $l = 0$, the deformation can be described as an combination of the p-envelope functions with $l = 1$ [Klingshirn 2005]. As a consequence, the exciton angular momentum becomes proportional to the magnetic field B. The energy of the magnetic dipole in a magnetic field is also proportional to magnetic field B, resulting in an overall quadratic dependence of the excitonic energy with respect to magnetic field in the low magnetic field region. Thus, the evolution of the data in magnetic field can be well described using

$$\Delta E_{\uparrow\downarrow} = -\frac{\hbar\omega_0}{2} + \frac{\hbar}{2}\sqrt{\omega_0^2 + \omega_c^2} \pm \frac{1}{2}g_s\mu_B B \tag{7.8}$$

where $\hbar\omega_0$ is an energy which controls the diamagnetic shift, $\hbar\omega_c = eB/m^*$ is the cyclotron energy and m^* is the reduced exciton mass, g_s is the effective g-factor.

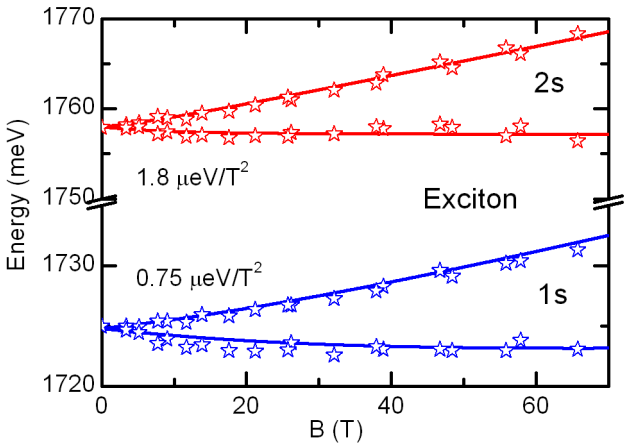

Figure 7.8: Magnetic field dependence of transmission in bulk WSe_2 measured at $T = 1.8$ K. The solid lines are fits to the data using Equation 7.8 to model the diamagnetic (quadratic) shift at low magnetic fields followed by a linear Landau like behavior at high magnetic fields.

Neglecting spin for the moment, at high magnetic field $\omega_c^2 \gg \omega_0^2$ and the energy is well approximated by $\hbar\omega_c/2$. At low fields when $\omega_0^2 \gg \omega_c^2$ to first order a Taylor expansion gives the diamagnetic shift

$$\Delta E = -\frac{\hbar\omega_0}{2} + \frac{\hbar\omega_0}{2}\sqrt{1+\frac{\omega_c^2}{\omega_0^2}} = -\frac{\hbar\omega_0}{2} + \frac{\hbar\omega_0}{2}\left(1+\frac{1}{2}\frac{\omega_c^2}{\omega_0^2}\right) \simeq \frac{\hbar\omega_c^2}{4\omega_0}$$

introducing the relation for ω_c gives

$$\Delta E \simeq \frac{\hbar e^2 B^2}{4\omega_0 m^{*2}} = e^2 a_0^2 B^2 \tag{7.9}$$

Here we have defined a length $a_0 = \sqrt{\hbar/4m^{*2}\omega_0}$ which can be identified with the effective Bohr radius in the hydrogen model [Walck 1998]. The solid lines in figure 7.8 are the transition energies calculated using Equation 7.8. For the 1s absorption, we use an effective mass $m^* = 0.7m_e$ as in monolayer WSe_2, an effective g-factor $g_s = 2.3$ and $\hbar\omega_0 = 8$ meV giving a diamagnetic shift at low magnetic fields of $\Delta E \approx 0.9\mu\text{V/T}^2$. The effective Bohr radius is $a_0 \approx 1.8$ nm from which we can obtain a rough estimate of the exciton binding energy in the hydrogen model

$$E_B = \frac{e^2}{8\pi\varepsilon_r\varepsilon_0 a_0} \approx 56 \text{ meV} \tag{7.10}$$

using a dielectric constant $\varepsilon_r \simeq 7$ for bulk 2H-WSe_2 [Beal 1976]. This value agrees well with the exciton binding energy of $\simeq 55$ meV determined directly from the $n = 1, 2, 3$ hydrogen series of levels in reflectance measurements on bulk 2H-WSe_2 crystals [Beal 1976]. A similar binding energy ($\simeq 56$ meV) has been reported [Goto 2000]

in high magnetic field measurements up to 150 T on bulk MoS_2, however with a much smaller diamagnetic shift $\simeq 0.2\mu eV/T^2$. The approximately four fold smaller diamagnetic shift is however, fully consistent with our data on WSe_2 when the smaller Bohr radius (1.28 nm) and smaller reduced exciton mass ($0.4m_e$) in MoS_2 are taken into account [Goto 2000]. From Equation 7.9, the diamagnetic shift in MoS_2 is expected to be ~ 0.57 times smaller due to the effective mass and ~ 0.5 times smaller due to the square of the Bohr radius.

For completeness, we have also fitted the 2s data using the same effective mass $m^* = 0.7m_e$, a slightly larger effective g-factor $g_s = 2.8$, and $\hbar\omega_0 = 2$ meV. The diamagnetic shift $\Delta E \approx 3.4\mu V/T^2$ is larger due to the more delocalized nature of the 2s wave function which extends over ≈ 3.7 nm. The obtained value of effective Bohr radius for the 2s ($n = 2$) exciton level is roughly two times less than the value predicted by hydrogen model [Pelant 2012].

7.5 Magnetic field dependent valley polarization

In monolayer WSe_2 the circular polarization $\sigma^{\pm}$ of the excitation allows us to selectively pump the **K**+ or **K**− valley. The circular polarization of the emission then depends on the inter valley scattering rate and the radiative recombination lifetime. In the absence of inter valley scattering the emission would be 100% polarized. The degree of circular polarization P_{circ} for the exciton and trion emission has been obtained by fitting the spectra for each value of magnetic field.

We have analyzed data for all four possible combinations of the circular polarization of the excitation and detection. Typical polarization resolved μPL spectra measured at 30 T for σ^+ and σ^- excitation are presented in Fig. 7.9(a) and (b) respectively. Note that the direction of the magnetic field was the same for all measurements. The required polarization combination was selected by rotating the excitation and detection polarization optics located outside of the cryostat. As in zero field, the 30 T raw data clearly shows that both neutral and charge exciton exhibits a significant degree of circular polarization.

The full magnetic field dependence of calculated degree of circular polarization of the neutral and charged exciton calculated using Equation 4.3 is presented in Fig. 7.9(c),(d) respectively. Both neutral and charged exciton shows a valley polarization in zero magnetic field, although we are not exciting exactly at the resonance. This is not surprising since it has been shown that WSe_2, which has the largest spin orbit induced spin splitting in both valence and the conduction bands of any member of the TX_2 family, has a valley polarization which is the most robust of all the transition metal dichalcogenides [Jones 2013]. For the exciton the degree of the circular polarization remains almost unchanged with the magnetic field suggesting that magnetic field has little influence on the inter valley exciton scattering rate. On the other hand the degree of polarization of the trion is strongly influenced with the polarization of the σ^+ excited emission (pumping **K**+ valley) increasing strongly, accompanied by an equally strong reduction in the degree of polarization for σ^-

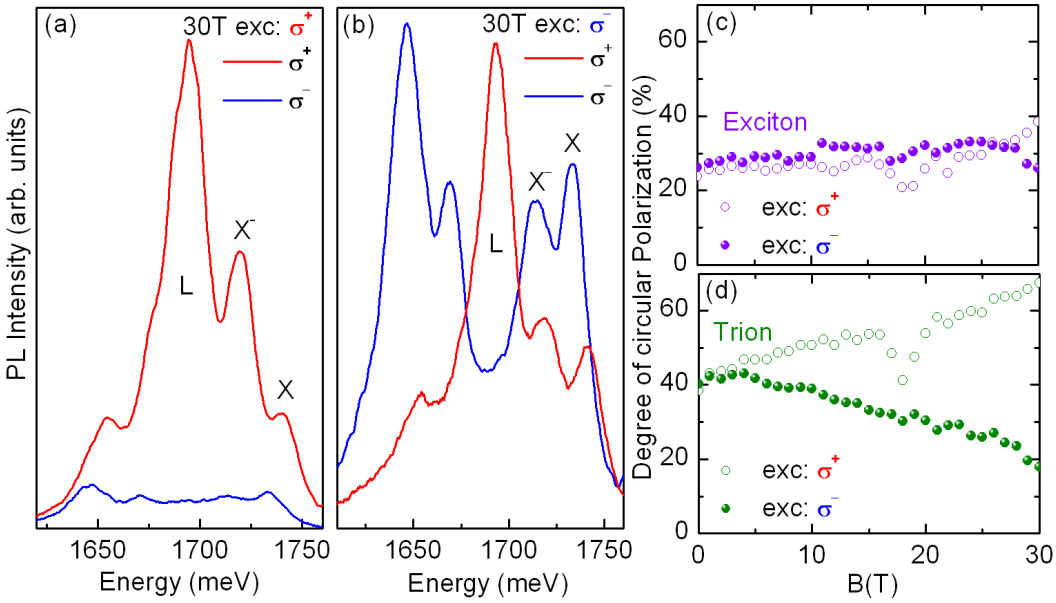

Figure 7.9: (a),(b) Typical μPL spectra in monolayer WSe_2 excited σ^+ and σ^- polarized laser, respectively. The red/blue lines denote the detection in σ^+ and σ^- respectively. (c),(d) degree of circular polarization $P = (I_{\sigma+} - I_{\sigma-})/(I_{\sigma+} + I_{\sigma-})$ of the neutral and charged exciton, respectively. The open symbols denote σ^+ excitation and symbols correspond to the σ^- polarization of the excitation.

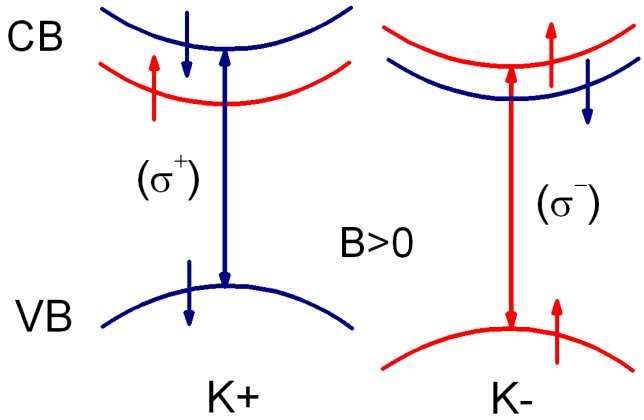

Figure 7.10: Simple picture showing the evolution of energy levels in conduction and valence band at the **K**+ and **K**− points of the Brillouin zone in magnetic field.

excitation (pumping **K**− valley). This suggests, that although the magnetic field does not modify the inter valley exciton scattering rate, it can nevertheless modify the probability for trion formation, most likely via its influence on the excess electron population of the spin orbit split spin levels in the conduction band for each valley. Figure 7.10 illustrates the polarization, σ^+ (blue) and σ^- (red), selection rules and energy shifts of inter band optical transitions in the **K**+ and **K**− valley in momentum space under an applied magnetic field. Spin up and down states are indicated by short arrows.

The evolution of the exciton and trion polarization reported here is somewhat different from previous investigations of WSe_2 monolayers [Aivazian 2015] and $MoSe_2$ monolayers [MacNeill 2015], which might be due to the low magnetic fields employed ($B \leq 7$ T). For example, in our data, the true behavior of the trion polarization is only revealed for magnetic fields $B \geq 5$ T. Additionally, the polarization depends sensitively upon the exact excitation used, together with sample dependent parameters such as the valley scattering rate. Nevertheless, the trion polarized-resolved photoluminescence in a magnetic field confirms the theoretical prediction that the inter valley trion is more stable than the intra valley trion due to exchange interaction. This provides important information about the valley character of the trion in monolayers.

7.6 Conclusion

In this chapter, we have investigated monolayer and bulk WSe_2 in high magnetic fields up to $B = 65$ T using optical spectroscopy. In monolayer WSe_2, the exciton emission exhibits a splitting which originates from lifting of the valley degeneracy by the magnetic field. The linear evolution of the energy of the exciton features in magnetic field can be described using a Dirac-like Hamiltonian for massive Dirac fermions with a Fermi velocity of 0.51×10^6m/s and an effective valley g-factor $g_v = 4$ for an assumed effective spin $s = 1/2$ system. The measured value of $\hbar v_F = 3.36$Å eV suggests $t = 1.02$ eV which is roughly 15% less than the effective hopping integral predicted from first principle band structure calculations [Xiao 2012, Rose 2013]. In contrast, in bulk WSe_2 where the inversion symmetry is restored, transmission measurements show that the exciton exhibits a spin (Zeeman) splitting and the exciton 1s and 2s features show a small diamagnetic shift which allows us to determine the exciton binding energy of around 56 meV within the three dimensional hydrogen model. In two dimensions, the binding energy is enhanced by at most a factor of four, so the predicted 2D exciton binding energy ($4 \times 56 \approx 224$ meV) is significantly less than the established value of 370 meV in monolayer WSe_2 [Beal 1976]. This suggests that dielectric screening (image charge), due to the very different dielectric environment outside of the material [Lin 2014, Chernikov 2014], significantly enhances the exciton binding energy in monolayer transition metal dichalcogenides.

Chapter 8

Conclusions

Two dimensional (2D) systems have attracted renewed interest since the discovery of graphene (Nobel Prize in Physics in 2010). Currently the research field of single layer truly 2D materials is highly competitive with a large number of groups around the world working on this topic. As the isolation of a monolayer of different dichalcogenides is recent, many electronic properties are still unknown. This work reports new experimental results in this field; the nature of carriers in monolayer and bulk dichalcogenides WS_2 and WSe_2 have been probed by means of optical spectroscopy in high magnetic field.

Micro-photoluminescence (μPL) experiments on monolayer WS_2 and WSe_2 show, that the trion emission is enhanced in our *ungated* samples due to the n-type nature of the crystals. Two color μPL experiments using above and below band gap illumination demonstrate that the trion/exciton intensity ratio can be independently tuned. The below band gap excitation tunes the excess electron density in the conduction band *via* the dynamic photo-ionization of neutral donors. This is a direct evidence that we can control the density of carriers in a 2D system by optical means. Moreover, since the photo-ionization threshold will be similar to the donor binding energy $\simeq$ 260meV this provides a possible method for the optical detection of far infrared radiation.

Raman scattering in monolayer WS_2 shows that under resonant conditions, a second order longitudinal acoustic mode (2LA) is observed at only 4cm^{-1} below the first order E^1_{2g} mode. These two Raman modes can be undistinguishable due to their small separation, leading to an erroneous estimation of the separation of the E^1_{2g} and A_{1g} modes, which is normally accepted to be a robust indication of the crystal thickness. Measurements involving linear polarization show that depending on the angle between polarization of the excitation and detection the 2LA mode can even dominate over the E^1_{2g} mode or *vice versa*. Thus, monolayers can be incorrectly assigned to bi-layer, tri-layer or even bulk crystals depending on the intensity of the 2LA mode. These results demonstrate that great care has to be exercised when interpreting Raman spectra taken under resonant conditions, especially if the excitation polarization is not carefully controlled.

The valley dynamics in monolayer WSe_2 has been probed with the use of a time-resolved method. The emission and polarization resolved dynamics of neutral and charged excitons in μPL have been investigated, with temporal resolution down to a few picoseconds. The exciton inter valley scattering between the $\mathbf{K}+$ and $\mathbf{K}-$ valleys is found to be of the order of several picoseconds. Possible origins for the fast inter valley scattering time include the long-range exchange interaction between an

electron and a hole in the exciton. Confirmation of this hypothesis requires further studies.

Magneto-spectroscopy experiments reveal marked differences between the nature of carriers in monolayer and bulk dichalcogenides. In monolayer WSe_2, the exciton emission exhibits a splitting which originates from lifting of the valley degeneracy by the magnetic field. The linear evolution of the energy of the exciton features in magnetic field can be described using a Dirac-like Hamiltonian for massive Dirac fermions with a Fermi velocity of 0.51×10^6m/s, which is twice less than in graphene (1.03×10^6m/s) and slightly smaller than in monolayer MoS_2 (0.85×10^6m/s). The measured Fermi velocity can be used to estimate the effective hopping integral t of the tight binding Hamiltonian $t = 1.02$ eV, which is roughly 15% less than the predicted effective hopping integral.

In contrast, in bulk WSe_2 where the inversion symmetry is restored, transmission measurements show that the exciton exhibits a spin (Zeeman) splitting and the exciton 1s and 2s features show a small diamagnetic shift which allows us to determine the exciton binding energy of around 56 meV within the 3D hydrogen model. In two dimensions, the binding energy is enhanced by at most a factor of four, so the predicted 2D exciton binding energy ($4 \times 56 \approx 224$ meV) is significantly less than the established value of 370 meV in monolayer WSe_2. This suggests that dielectric screening (image charge), due to the very different dielectric environment outside of the material, significantly enhances the exciton binding energy in monolayer transition metal dichalcogenides.

Finally, we have demonstrated the ability to tune of the valley degree of freedom in monolayer transition metal dichalcogenides using a magnetic field. The trion polarized-resolved photoluminescence in a magnetic field confirms the theoretical prediction that the inter valley trion is more stable than the intra valley trion due to exchange interaction. This provides important information about the valley character of the trion in monolayers. Moreover, the manipulation of the valley degree of freedom in monolayer transition metal dichalcogenides opens up new opportunities to understand and explore the valley physics in these materials. Future experiments in this area will probably focus on creation of quantum bits in the excited coherent states at the $\mathbf{K}+$ and $\mathbf{K}-$ valleys, and the generation of a steady state valley-spin current.

Appendix A

Publications

Publications based on the results of this thesis:

1. **A. A. Mitioglu**, L. Klopotowski, D. K. Maude, G. Deligeorgis, S. Anghel, L. Kulyuk, and P. Plochocka
"Intervalley scattering of excitons and trions in monolayer WSe_2 under strong excitation"
Submitted to 2D Materials

2. **A. A. Mitioglu**, P. Plochocka, A. Granados del Aguila, P. C. M. Christianen, G. Deligeorgis, S. Anghel, L. Kulyuk, and D. K. Maude
"Optical investigation of monolayer and bulk tungsten diselenide (WSe_2) in high magnetic fields"
Nano Letters **15 (7)**, 4387 (2015)

3. **A. A. Mitioglu**, P. Plochocka, G. Deligeorgis, S. Anghel, L. Kulyuk, and D. K. Maude
"Second-order resonant Raman scattering in single-layer tungsten disulfide WS_2"
Physical Review B **89**, 245442 (2014)

4. **A. A. Mitioglu**, P. Plochocka, J. N. Jadczak, W. Escoffier, G. L. J. A. Rikken, L. Kulyuk, and D. K. Maude
"Optical manipulation of the exciton charge state in single-layer tungsten disulfide"
Physical Review B **88**, 245403 (2013)

Further publications:

1. Atsuhiko Miyata, **Anatolie Mitioglu**, Paulina Plochocka, Oliver Portugall, Jacob Tse-Wei Wang, Samuel D. Stranks, Henry J. Snaith, Robin J. Nicholas
"Direct measurement of the exciton binding energy and effective masses for charge carriers in organic-inorganic tri-halide perovskites"
Nature Physics **11**, 582 (2015)

2. F. Iacovella, P. Trinsoutrot, **A. A. Mitioglu**, V. Conedera, M. Pierre, B. Raquet, M. Goiran, H. Vergnes, B. Caussat, P. Plochocka, and W. Escoffier
"Magneto-transport properties of a random distribution of few-layer graphene patches"
Journal of Applied Physics **116**,193705 (2014)

3. J. Jadczak, P. Plochocka, **A. A. Mitioglu**, I. Breslavetz, M. Royo , A. Bertoni , G. Goldoni, T. Smolenski, P. Kossacki, A. Kretinin, Hadas Shtrikman, and D. K. Maude
   "Unintentional high-density p-type modulation doping of a GaAs/AlAs core/multi-shell nanowire"
   Nano Letters **14**, 2807 (2014)

4. P. Plochocka, **A. A. Mitioglu**, D. K. Maude, G. L. J. A. Rikken , A Granados del Aguila, P. C. M. Christianen, P. Kacman, and Hadas Shtrikman
   "High magnetic field reveals the nature of excitons in a single GaAs/AlAs core/shell nanowire"
   Nano Letters **13**, 2442 (2013)

5. A. S. Cuharuc, L. L. Kulyuk, R. I. Lascova, **A. A. Mitioglu**, A. I. Dikusar
   "Electrochemical characterization of PbS quantum dots capped with oleic acid and PbS thin films - a comparative study"
   Surface Engineering and Applied Electrochemistry **48**, 193 (2012)

Bibliography

[Aivazian 2015] G. Aivazian, Z. Gong, A. M Jones, R.-L. Chu, J. Yan, D. G Mandrus, C. Zhang, D. Cobden, W. Yao and X. Xu. *Magnetic Control of Valley Pseudospin in Monolayer WSe_2*. Nature Physics, vol. 11, page 148, 2015. (Cited on pages 18, 90, 92, 97, 99 and 104.)

[Albe 2002] Karsten Albe and Andreas Klein. *Density-functional-theory calculations of electronic band structure of single-crystal and single-layer WS_2*. Phys. Rev. B, vol. 66, page 073413, Aug 2002. (Cited on page 37.)

[Alem 2009] Nasim Alem, Rolf Erni, Christian Kisielowski, Marta D. Rossell, Will Gannett and A. Zettl. *Atomically thin hexagonal boron nitride probed by ultrahigh-resolution transmission electron microscopy*. Phys. Rev. B, vol. 80, page 155425, Oct 2009. (Cited on page 33.)

[Ballif 1996] C. Ballif, M. Regula, P.E. Schmid, M. Remskar, R. Sanjinés and F. Lee C. Levy. *Preparation and characterization of highly oriented, photoconducting WS_2 thin films*. Applied Physics A, vol. 62, no. 6, pages 543–546, 1996. (Cited on page 3.)

[Ballif 1999] C. Ballif, M. Regula and F. Levy. *Optical and electrical properties of semiconducting WS_2 thin films: From macroscopic to local probe measurements*. Solar Energy Materials and Solar Cells, vol. 57, no. 2, pages 189 – 207, 1999. (Cited on pages 6 and 7.)

[Baugher 2014] B. W. H. Baugher, H. O. H. Churchill, Y. Yang and P. Jarillo-Herrero. *Optoelectronic devices based on electrically tunable p-n diodes in a monolayer dichalcogenide*. Nature Nanotechnology, vol. 9, pages 262–267, April 2014. (Cited on page 2.)

[Beal 1976] A R Beal and W Y Liang. *Excitons in 2H-WSe_2 and 3R-WS_2*. Journal of Physics C: Solid State Physics, vol. 9, no. 12, page 2459, 1976. (Cited on pages 7, 10, 95, 101 and 104.)

[Berkdemir 2013] Ayse Berkdemir, Humberto R. Gutiérrez, Andrés R. Botello-Méndez, Néstor Perea-López, Ana Laura Elías, Chen-Ing Chia, Bei Wang, Vincent H. Crespi, Florentino López-Urías, Jean-Christophe Charlier, Humberto Terrones and Mauricio Terrones. *Identification of individual and few layers of WS_2 using Raman Spectroscopy*. Scientific Reports, vol. 3, page 1755, 2013. (Cited on pages 58, 64, 65, 66, 67, 68 and 76.)

[Berkelbach 2013] Timothy C. Berkelbach, Mark S. Hybertsen and David R. Reichman. *Theory of neutral and charged excitons in monolayer transition metal dichalcogenides*. Phys. Rev. B, vol. 88, page 045318, Jul 2013. (Cited on page 12.)

[Bordas 1976] J. Bordas. *Some Aspects of Modulation Spectroscopy in Layer Materials.* In PeterA. Lee, editeur, Optical and Electrical Properties, volume 4 of *Physics and Chemistry of Materials with Layered Structures*, pages 145–229. Springer Netherlands, 1976. (Cited on page 10.)

[Buyanova 1999] I. A. Buyanova, W. M. Chen, G. Pozina, J. P. Bergman, B. Monemar, H. P. Xin and C. W. Tu. *Mechanism for low-temperature photoluminescence in GaNAs/GaAs structures grown by molecular-beam epitaxy.* Applied Physics Letters, vol. 75, no. 4, pages 501–503, 1999. (Cited on page 54.)

[Cao 2012] Ting Cao, Gang Wang, Wenpeng Han, Huiqi Ye, Chuanrui Zhu, Junren Shi, Qian Niu, Pingheng Tan, Enge Wang Baoli Liu and Ji Feng. *Valley-selective circular dichroism of monolayer molybdenum disulphide.* Nature Communications, vol. 3, page 887, 2012. (Cited on pages 15, 17, 53, 80 and 82.)

[Cappelluti 2013] E. Cappelluti, R. Roldán, J. A. Silva-Guillén, P. Ordejón and F. Guinea. *Tight-binding model and direct-gap/indirect-gap transition in single-layer and multilayer MoS_2.* Phys. Rev. B, vol. 88, page 075409, Aug 2013. (Cited on page 9.)

[Castro Neto 2009] A. H. Castro Neto, F. Guinea, N. M. R. Peres, K. S. Novoselov and A. K. Geim. *The electronic properties of graphene.* Rev. Mod. Phys., vol. 81, pages 109–162, Jan 2009. (Cited on page 90.)

[Chang 1996] Ming-Che Chang and Qian Niu. *Berry phase, hyperorbits, and the Hofstadter spectrum: Semiclassical dynamics in magnetic Bloch bands.* Phys. Rev. B, vol. 53, pages 7010–7023, Mar 1996. (Cited on page 13.)

[Chen 1974] J.M. Chen and C.S. Wang. *Second order Raman spectrum of MoS_2.* Solid State Communications, vol. 14, no. 9, pages 857 – 860, 1974. (Cited on pages 58 and 69.)

[Chen 2014] Yanfeng Chen, Dumitru O. Dumcenco, Yiming Zhu, Xin Zhang, Nannan Mao, Qingliang Feng, Mei Zhang, Jin Zhang, Ping-Heng Tan, Ying-Sheng Huang and Liming Xie. *Composition-dependent Raman modes of $Mo_{1-x}W_xS_2$ monolayer alloys.* Nanoscale, vol. 6, pages 2833–2839, 2014. (Cited on page 75.)

[Chernikov 2014] Alexey Chernikov, Timothy C. Berkelbach, Heather M. Hill, Albert Rigosi, Yilei Li, Ozgur Burak Aslan, David R. Reichman, Mark S. Hybertsen and Tony F. Heinz. *Exciton Binding Energy and Nonhydrogenic Rydberg Series in Monolayer WS_2.* Phys. Rev. Lett., vol. 113, page 076802, Aug 2014. (Cited on pages 10, 11, 12, 43 and 104.)

[Coehoorn 1987] R. Coehoorn, C. Haas and R. A. de Groot. *Electronic structure of $MoSe_2$, MoS_2, and WSe_2. II. The nature of the optical band gaps.* Phys. Rev. B, vol. 35, pages 6203–6206, Apr 1987. (Cited on pages 1 and 94.)

[Conley 2013] Hiram J. Conley, Bin Wang, Jed I. Ziegler, Richard F. Haglund, Sokrates T. Pantelides and Kirill I. Bolotin. *Bandgap Engineering of Strained Monolayer and Bilayer MoS_2*. Nano Letters, vol. 13, no. 8, pages 3626–3630, 2013. (Cited on pages 38, 40 and 64.)

[Cosse 1980] C. Cosse, M. Fouassier, T. Mejean, M. Tranquille, D. P. DiLella and M. Moskovits. *Dititanium and divanadium*. The Journal of Chemical Physics, vol. 73, no. 12, pages 6076–6085, 1980. (Cited on page 71.)

[Cunningham 2012] Graeme Cunningham, Mustafa Lotya, Clotilde S. Cucinotta, Stefano Sanvito, Shane D. Bergin, Robert Menzel, Milo S. P. Shaffer and Jonathan N. Coleman. *Solvent Exfoliation of Transition Metal Dichalcogenides: Dispersibility of Exfoliated Nanosheets Varies Only Weakly between Compounds*. ACS Nano, vol. 6, no. 4, pages 3468–3480, 2012. PMID: 22394330. (Cited on page 2.)

[Deslippe 2009] Jack Deslippe, Mario Dipoppa, David Prendergast, Marcus V. O. Moutinho, Rodrigo B. Capaz and Steven G. Louie. *Electron Hole Interaction in Carbon Nanotubes: Novel Screening and Exciton Excitation Spectra*. Nano Letters, vol. 9, no. 4, pages 1330–1334, 2009. (Cited on page 12.)

[Dumcenco 2011] D. O. Dumcenco, Y.-C. Su, Y.-P. Wang, K.-Y. Chen, Y.-S. Huang, C.-H. Ho and K.-K. Tiong. *Polarization Dependent Raman Active Modes Study of the $Mo_{1-x}W_xS_2$ Mixed Layered Crystals*. Chinese Journal of Physics, vol. 3, page 270, 2011. (Cited on page 58.)

[Eda 2011] Goki Eda, Hisato Yamaguchi, Damien Voiry, Takeshi Fujita, Mingwei Chen and Manish Chhowalla. *Photoluminescence from Chemically Exfoliated MoS_2*. Nano Letters, vol. 11, no. 12, pages 5111–5116, 2011. (Cited on page 1.)

[Evans 1967] B L Evans and P A Young. *Exciton spectra in thin crystals: the diamagnetic effect*. Proceedings of the Physical Society, vol. 91, no. 2, page 475, 1967. (Cited on pages 90 and 95.)

[Fan 2014] Jia-He Fan, Po Gao, An-Min Zhang, Bai-Ren Zhu, Hua-Ling Zeng, Xiao-Dong Cui, Rui He and Qing-Ming Zhang. *Resonance Raman scattering in bulk 2H-MX_2 (M=Mo, W; X=S, Se) and monolayer MoS_2*. Journal of Applied Physics, vol. 115, no. 5, pages –, 2014. (Cited on page 66.)

[Ferrari 2006] A. C. Ferrari, J. C. Meyer, V. Scardaci, C. Casiraghi, M. Lazzeri, F. Mauri, S. Piscanec, D. Jiang, K. S. Novoselov, S. Roth and A. K. Geim. *Raman Spectrum of Graphene and Graphene Layers*. Phys. Rev. Lett., vol. 97, page 187401, Oct 2006. (Cited on pages 36 and 58.)

[Frey 1999] Gitti L. Frey, Reshef Tenne, Manyalibo J. Matthews, M. S. Dresselhaus and G. Dresselhaus. *Raman and resonance Raman investigation of MoS_2*

nanoparticles. Phys. Rev. B, vol. 60, pages 2883–2892, Jul 1999. (Cited on page 58.)

[Geim 2013] A. K. Geim and I. V. Grigorieva. *Van der Waals heterostructures.* Nature, no. 499, pages 419–425, July 2013. (Cited on page 2.)

[Georgiou 2013] T. Georgiou, R. Jalil, B. D. Belle, L. Britnell, R. V. Gorbachev, S. V. Morozov, Y.-J. Kim, A. Gholinia, S. J. Haigh, O. Makarovsky, L. Eaves, L. A. Ponomarenko, A. K. Geim, K. S. Novoselov and A. Mishchenko. *Vertical field-effect transistor based on graphene-WS_2 heterostructures for flexible and transparent electronics.* Nature Nanotechnology, vol. 8, pages 100–103, February 2013. (Cited on page 2.)

[Glazov 2014] M. M. Glazov, T. Amand, X. Marie, D. Lagarde, L. Bouet and B. Urbaszek. *Exciton fine structure and spin decoherence in monolayers of transition metal dichalcogenides.* Phys. Rev. B, vol. 89, page 201302, May 2014. (Cited on page 80.)

[Goto 2000] T Goto, Y Kato, K Uchida and N Miura. *Exciton absorption spectra of MoS_2 crystals in high magnetic fields up to 150 T.* Journal of Physics: Condensed Matter, vol. 12, no. 30, page 6719, 2000. (Cited on pages 90, 101 and 102.)

[Graf 2007] D. Graf, F. Molitor, K. Ensslin, C. Stampfer, A. Jungen, C. Hierold and L. Wirtz. *Spatially Resolved Raman Spectroscopy of Single- and Few-Layer Graphene.* Nano Letters, vol. 7, no. 2, pages 238–242, 2007. PMID: 17297984. (Cited on page 36.)

[Gupta 2006] A. Gupta, G. Chen, P. Joshi, S. Tadigadapa and Eklund. *Raman Scattering from High-Frequency Phonons in Supported n-Graphene Layer Films.* Nano Letters, vol. 6, no. 12, pages 2667–2673, 2006. PMID: 17163685. (Cited on page 58.)

[Gutiérrez 2013] Humberto R. Gutiérrez, Nestor Perea-Lopez, Ana Laura Elias, Ayse Berkdemir, Bei Wang, Ruitao Lv, Florentino Lou J.pez-Urias, Vincent H. Crespi, Humberto Terrones and Mauricio Terrones. *Extraordinary Room-Temperature Photoluminescence in Triangular WS_2 Monolayers.* Nano Letters, vol. 13, no. 8, pages 3447–3454, 2013. (Cited on pages 37, 58, 64 and 68.)

[Hajiyev 2013] Parviz Hajiyev, Chunxiao Cong, Caiyu Qiu and Ting Yu. *Contrast and Raman spectroscopy study of single- and few-layered charge density wave material: 2H-$TaSe_2$.* Scientific Reports, vol. 3, page 2593, 2013. (Cited on page 58.)

[Hart 1970] T. R. Hart, R. L. Aggarwal and Benjamin Lax. *Temperature Dependence of Raman Scattering in Silicon.* Phys. Rev. B, vol. 1, pages 638–642, Jan 1970. (Cited on page 68.)

[He 2014] Keliang He, Nardeep Kumar, Liang Zhao, Zefang Wang, Kin Fai Mak, Hui Zhao and Jie Shan. *Tightly Bound Excitons in Monolayer WSe_2*. Phys. Rev. Lett., vol. 113, page 026803, Jul 2014. (Cited on pages 10 and 12.)

[Huard 2000] V. Huard, R. T. Cox, K. Saminadayar, A. Arnoult and S. Tatarenko. *Bound States in Optical Absorption of Semiconductor Quantum Wells Containing a Two-Dimensional Electron Gas*. Phys. Rev. Lett., vol. 84, pages 187–190, Jan 2000. (Cited on page 43.)

[Jariwala 2013] Deep Jariwala, Vinod K. Sangwan, Chung-Chiang Wu, Pradyumna L. Prabhumirashi, Michael L. Geier, Tobin J. Marks, Lincoln J. Lauhon and Mark C. Hersam. *Gate-tunable carbon nanotube MoS_2 heterojunction p-n diode*. Proceedings of the National Academy of Sciences, vol. 110, no. 45, pages 18076–18080, 2013. (Cited on page 2.)

[Jin 2013] Wencan Jin, Po-Chun Yeh, Nader Zaki, Datong Zhang, Jerzy T. Sadowski, Abdullah Al-Mahboob, Arend M. van der Zande, Daniel A. Chenet, Jerry I. Dadap, Irving P. Herman, Peter Sutter, James Hone and Richard M. Osgood. *Direct Measurement of the Thickness-Dependent Electronic Band Structure of MoS_2 Using Angle-Resolved Photoemission Spectroscopy*. Phys. Rev. Lett., vol. 111, page 106801, Sep 2013. (Cited on page 8.)

[Jones 2013] A. M. Jones, H. Yu, N. J. Ghimire, S. Wu, G. Aivazian, J. S. Ross, B. Zhao, J. Yan, D. G. Mandrus, D. Xiao, W. Yao and X. Xu. *Optical generation of excitonic valley coherence in monolayer WSe_2*. Nature Nanotechnology, vol. 8, pages 634–638, September 2013. (Cited on pages 11, 12, 18, 40, 41, 49, 51, 52, 53, 54, 80, 87, 90, 95, 96 and 102.)

[Kam 1982] K. K. Kam and B. A. Parkinson. *Detailed photocurrent spectroscopy of the semiconducting group VIB transition metal dichalcogenides*. The Journal of Physical Chemistry, vol. 86, no. 4, pages 463–467, 1982. (Cited on page 6.)

[Kheng 1993] K. Kheng, R.T. Cox, Y. Merle d'Aubigné, F. Bassani, K. Saminadayar and S. Tatarenko. *Observation of negatively charged excitons X^- in semiconductor quantum wells*. Phys. Rev. Lett., vol. 71, page 1752, 1993. (Cited on page 10.)

[Kioseoglou 2012] G. Kioseoglou, A. T. Hanbicki, M. Currie, A. L. Friedman, D. Gunlycke and B. T. Jonker. *Valley polarization and intervalley scattering in monolayer MoS_2*. Applied Physics Letters, vol. 101, no. 22, page 221907, 2012. (Cited on pages 15, 58, 80 and 85.)

[Klein 2001] A. Klein, S. Tiefenbacher, V. Eyert, C. Pettenkofer and W. Jaegermann. *Electronic band structure of single-crystal and single-layer WS_2 Influence of interlayer van der Waals interactions*. Phys. Rev. B, vol. 64, page 205416, Nov 2001. (Cited on page 40.)

[Klingshirn 2005] Claus Klingshirn. Semiconductor optics. Advanced texts in physics. Springer, 2nd édition, 2005. (Cited on page 100.)

[Knox 1963] Robert S Knox. Theory of excitons. Solid state physics lt; New York, NY, 1955; Supplement, 5. Academic Pr, 2. print édition, 1963. (Cited on page 93.)

[Knox 1983] R.S. Knox. *Introduction to Exciton Physics*. In Baldassare Di Bartolo, editeur, Collective Excitations in Solids, volume 88 of *NATO Advanced Science Institute Series*, pages 183–245. Springer US, 1983. (Cited on page 10.)

[Korn 2011] T. Korn, S. Heydrich, M. Hirmer, J. Schmutzler and C. Schüller. *Low-temperature photocarrier dynamics in monolayer MoS_2*. Applied Physics Letters, vol. 99, no. 10, page 102109, 2011. (Cited on pages 36 and 84.)

[Kossacki 1999] P. Kossacki, J. Cibert, D. Ferrand, Y. Merle d'Aubigné, A. Arnoult, A. Wasiela, S. Tatarenko and J. A. Gaj. *Neutral and positively charged excitons: A magneto-optical study of a p-doped $Cd_{1-x}Mn_xTe$ quantum well.* Phys. Rev. B, vol. 60, page 16018, 1999. (Cited on page 43.)

[Kossacki 2002] P. Kossacki, V. Ciulin, M. Kutrowski, J.-D. Ganière, T. Wojtowicz and B. Deveaud. *Formation Time of Negatively Charged Excitons in CdTe-Based Quantum Wells.* physica status solidi (b), vol. 229, no. 2, pages 659–663, 2002. (Cited on page 83.)

[Kossacki 2004] P. Kossacki, H. Boukari, M. Bertolini, D. Ferrand, J. Cibert, S. Tatarenko, J. Gaj, B. Deveaud, V. Ciulin and M. Potemski. *Photoluminescence of p-doped quantum wells with strong spin splitting.* Phys. Rev. B, vol. 70, page 195337, Nov 2004. (Cited on page 43.)

[Kozawa 2014] D. Kozawa, R. Kumar, A. Carvalho, A. Kiran Kumar, W. Zhao, S. Wang, M. Toh, R. M. Ribeiro, A. H. Castro Neto, K. Matsuda and G. Eda. *Photocarrier relaxation pathway in two-dimensional semiconducting transition metal dichalcogenides.* Nature Communications, vol. 5, page 4543, 2014. (Cited on page 6.)

[Kuc 2015] Agnieszka Kuc and Thomas Heine. *The electronic structure calculations of two-dimensional transition-metal dichalcogenides in the presence of external electric and magnetic fields.* Chem. Soc. Rev., pages –, 2015. (Cited on page 3.)

[Lagarde 2014] D. Lagarde, L. Bouet, X. Marie, C. R. Zhu, B. L. Liu, T. Amand, P. H. Tan and B. Urbaszek. *Carrier and Polarization Dynamics in Monolayer MoS_2*. Phys. Rev. Lett., vol. 112, page 047401, Jan 2014. (Cited on page 84.)

[Lanzillo 2013] Nicholas A. Lanzillo, A. Glen Birdwell, Matin Amani, Frank J. Crowne, Pankaj B. Shah, Sina Najmaei, Zheng Liu, Pulickel M. Ajayan, Jun

Lou, Madan Dubey, Saroj K. Nayak and Terrance P. O'Regan. *Temperature-dependent phonon shifts in monolayer MoS_2.* Applied Physics Letters, vol. 103, no. 9, page 093102, 2013. (Cited on page 68.)

[Lee 2010] Changgu Lee, Hugen Yan, Louis E. Brus, Tony F. Heinz, James Hone and Sunmin Ryu. *Anomalous Lattice Vibrations of Single- and Few-Layer MoS_2.* ACS Nano, vol. 4, no. 5, pages 2695–2700, 2010. PMID: 20392077. (Cited on pages 58, 63 and 64.)

[Lee 2015] B. Lee, J. Park, G. H. Han, H.-S. Ee, C. H. Naylor, W. Liu, A. T. C. Johnson and R. Agarwal. *Fano resonance and spectrally modified photoluminescence enhancement in monolayer MoS_2 integrated with plasmonic nanoantenna array.* ArXiv e-prints, March 2015. (Cited on page 2.)

[Levy-Clement 1992] C. Levy-Clement and R. Tenne. *Modification of Surface Properties of Layered Compounds by Chemical and (Photo)Electrochemical Processes.* In A. Aruchamy, editeur, Photoelectrochemistry and Photovoltaics of Layered Semiconductors, volume 14 of *Physics and Chemistry of Materials with Low-Dimensional Structures*, pages 155–194. Springer Netherlands, 1992. (Cited on page 3.)

[Li 2012a] Hong Li, Qing Zhang, Chin Chong Ray Yap, Beng Kang Tay, Teo Hang Tong Edwin, Aurelien Olivier and Dominique Baillargeat. *From Bulk to Monolayer MoS_2: Evolution of Raman Scattering.* Advanced Functional Materials, vol. 22, no. 7, pages 1385–1390, 2012. (Cited on page 58.)

[Li 2012b] Song-Lin Li, Hisao Miyazaki, Haisheng Song, Hiromi Kuramochi, Shu Nakaharai and Kazuhito Tsukagoshi. *Quantitative Raman Spectrum and Reliable Thickness Identification for Atomic Layers on Insulating Substrates.* ACS Nano, vol. 6, no. 8, pages 7381–7388, 2012. (Cited on page 58.)

[Li 2013] Hai Li, Gang Lu, Yanlong Wang, Zongyou Yin, Chunxiao Cong, Qiyuan He, Lu Wang, Feng Ding, Ting Yu and Hua Zhang. *Mechanical Exfoliation and Characterization of Single- and Few-Layer Nanosheets of WSe_2, TaS_2, and $TaSe_2$.* Small, vol. 9, no. 11, pages 1974–1981, 2013. (Cited on pages 33 and 58.)

[Li 2014] Yilei Li, Jonathan Ludwig, Tony Low, Alexey Chernikov, Xu Cui, Ghidewon Arefe, Young Duck Kim, Arend M. van der Zande, Albert Rigosi, Heather M. Hill, Suk Hyun Kim, James Hone, Zhiqiang Li, Dmitry Smirnov and Tony F. Heinz. *Valley Splitting and Polarization by the Zeeman Effect in Monolayer $MoSe_2$.* Phys. Rev. Lett., vol. 113, page 266804, Dec 2014. (Cited on pages 90, 92 and 99.)

[Lieth 1977] R. M. A. Lieth. Preparation and crystal growth of materials with layered structures. Springer Netherlands, 1977. (Cited on page 32.)

[Lin 2014] Yuxuan Lin, Xi Ling, Lili Yu, Shengxi Huang, Allen L. Hsu, Yi-Hsien Lee, Jing Kong, Mildred S. Dresselhaus and Tomás Palacios. *Dielectric Screening of Excitons and Trions in Single-Layer MoS_2.* Nano Letters, vol. 14, no. 10, pages 5569–5576, 2014. (Cited on pages 12 and 104.)

[Loudon 1964] D. Loudon. *The Raman effect in crystals.* Adv. Phys., vol. 13, page 423, 1964. (Cited on page 73.)

[Luo 2013] Xin Luo, Yanyuan Zhao, Jun Zhang, Minglin Toh, Christian Kloc, Qihua Xiong and Su Ying Quek. *Effects of lower symmetry and dimensionality on Raman spectra in two-dimensional WSe_2.* Phys. Rev. B, vol. 88, page 195313, Nov 2013. (Cited on page 58.)

[MacNeill 2015] David MacNeill, Colin Heikes, Kin Fai Mak, Zachary Anderson, Andor Kormányos, Viktor Zólyomi, Jiwoong Park and Daniel C. Ralph. *Breaking of Valley Degeneracy by Magnetic Field in Monolayer $MoSe_2$.* Phys. Rev. Lett., vol. 114, page 037401, Jan 2015. (Cited on pages 90 and 104.)

[Mai 2014a] Cong Mai, Andrew Barrette, Yifei Yu, Yuriy G. Semenov, Ki Wook Kim, Linyou Cao and Kenan Gundogdu. *Many-Body Effects in Valleytronics: Direct Measurement of Valley Lifetimes in Single-Layer MoS_2.* Nano Letters, vol. 14, no. 1, pages 202–206, 2014. PMID: 24325650. (Cited on page 80.)

[Mai 2014b] Cong Mai, Yuriy G. Semenov, Andrew Barrette, Yifei Yu, Zhenghe Jin, Linyou Cao, Ki Wook Kim and Kenan Gundogdu. *Exciton valley relaxation in a single layer of WS_2 measured by ultrafast spectroscopy.* Phys. Rev. B, vol. 90, page 041414, Jul 2014. (Cited on page 80.)

[Maialle 1993] M. Z. Maialle, E. A. de Andrada e Silva and L. J. Sham. *Exciton spin dynamics in quantum wells.* Phys. Rev. B, vol. 47, pages 15776–15788, Jun 1993. (Cited on page 85.)

[Mak 2010] Kin Fai Mak, Changgu Lee, James Hone, Jie Shan and Tony F. Heinz. *Atomically Thin MoS_2: A New Direct-Gap Semiconductor.* Phys. Rev. Lett., vol. 105, page 136805, Sep 2010. (Cited on pages 1, 2, 5, 7, 8, 33, 36 and 89.)

[Mak 2012] K. F. Mak, K. He, J. Shan and T. F. Heinz. *Control of valley polarization in monolayer MoS_2 by optical helicity.* Nature Nanotechnology, vol. 7, pages 494–498, 2012. (Cited on pages 15, 17, 53, 79, 80, 82 and 96.)

[Mak 2013] Kin Fai Mak, Keliang He, Changgu Lee, Gwan Hyoung Lee, James Honeand Tony F. Heinz and Jie Shan. *Tightly bound trions in monolayer MoS_2.* Nature Materials, vol. 12, page 207, 2013. (Cited on pages 40 and 41.)

[Makado 1986] P C Makado and N C McGill. *Energy levels of a neutral hydrogen-like system in a constant magnetic field of arbitrary strength.* Journal of Physics C: Solid State Physics, vol. 19, no. 6, page 873, 1986. (Cited on page 93.)

[Miura 2007] Noboru Miura. Physics of semiconductors in high magnetic fields. Oxford University Press, 2007. (Cited on pages 91 and 92.)

[Molina-Sanchez 2011] A. Molina-Sanchez and L. Wirtz. *Phonons in single-layer and few-layer MoS_2 and WS_2*. Phys. Rev. B, vol. 84, page 155413, Oct 2011. (Cited on pages 64 and 76.)

[Mouri 2013] Shinichiro Mouri, Yuhei Miyauchi and Kazunari Matsuda. *Tunable Photoluminescence of Monolayer MoS_2 via Chemical Doping*. Nano Letters, vol. 13, no. 12, pages 5944–5948, 2013. PMID: 24215567. (Cited on pages 40 and 88.)

[Najmaei 2012] S. Najmaei, Z. Liu, P. M. Ajayan and J. Lou. *Thermal effects on the characteristic Raman spectrum of molybdenum disulfide (MoS_2) of varying thicknesses*. Applied Physics Letters, vol. 100, no. 1, pages –, 2012. (Cited on page 71.)

[Najmaei 2014] Sina Najmaei, Adnen Mlayah, Arnaud Arbouet, Christian Girard, Jean Leotin and Jun Lou. *Plasmonic Pumping of Excitonic Photoluminescence in Hybrid MoS_2 Au Nanostructures*. ACS Nano, vol. 8, no. 12, pages 12682–12689, 2014. PMID: 25469686. (Cited on page 2.)

[Neville 1976] R. A. Neville and B. L. Evans. *The Band Edge Excitons in 2H-MoS_2*. physica status solidi (b), vol. 73, no. 2, pages 597–606, 1976. (Cited on pages 90, 95 and 100.)

[Novoselov 2005] K. S. Novoselov, D. Jiang, F. Schedin, T. J. Booth, V. V. Khotkevich, S. V. Morozov and A. K. Geim. *Two-dimensional atomic crystals*. Proceedings of the National Academy of Sciences of the United States of America, vol. 102, no. 30, pages 10451–10453, 2005. (Cited on pages 2 and 33.)

[O'Donnell 1991] K. P. O'Donnell and X. Chen. *Temperature dependence of semiconductor band gaps*. Applied Physics Letters, vol. 58, no. 25, pages 2924–2926, 1991. (Cited on page 55.)

[Palummo 2015] Maurizia Palummo, Marco Bernardi and Jeffrey C. Grossman. *Exciton Radiative Lifetimes in Two-Dimensional Transition Metal Dichalcogenides*. Nano Letters, vol. 0, no. 0, page null, 2015. (Cited on page 84.)

[Pamplin 1979] Brian Pamplin. Progress in crystal growth and characterization of materials. 1979. (Cited on page 31.)

[Peimyoo 2014] Namphung Peimyoo, Weihuang Yang, Jingzhi Shang, Xiaonan Shen, Yanlong Wang and Ting Yu. *Chemically Driven Tunable Light Emission of Charged and Neutral Excitons in Monolayer WS_2*. ACS Nano, vol. 8, no. 11, pages 11320–11329, 2014. PMID: 25317839. (Cited on page 40.)

[Pelant 2012] Ivan Pelant and Jan Valenta. Luminescence spectroscopy of semiconductors. Oxford University Press, 2012. (Cited on page 102.)

[Pikus 1971] G.-E Pikus and G.-L. Bir. *Exchange Interaction in Excitons in Semiconductors.* JETP, vol. 33, page 108, May 1971. (Cited on page 18.)

[Plechinger 2012] G. Plechinger, S. Heydrich, J. Eroms, D. Weiss, C. Schäller and T. Korn. *Raman spectroscopy of the interlayer shear mode in few-layer MoS_2 flakes.* Applied Physics Letters, vol. 101, no. 10, pages –, 2012. (Cited on page 63.)

[Plochocka 2004] P. Plochocka, P. Kossacki, W. Maślana, J. Cibert, S. Tatarenko, C. Radzewicz and J. A. Gaj. *Femtosecond Study of the Interplay between Excitons, Trions, and Carriers in (Cd,Mn)Te Quantum Wells.* Phys. Rev. Lett., vol. 92, page 177402, Apr 2004. (Cited on page 45.)

[Portella-Oberli 2009] M. T. Portella-Oberli, J. Berney, L. Kappei, F. Morier-Genoud, J. Szczytko and B. Deveaud-Plédran. *Dynamics of Trion Formation in $In_xGa_{1-x}As$ Quantum Wells.* Phys. Rev. Lett., vol. 102, page 096402, Mar 2009. (Cited on page 83.)

[Pospischil 2014] A. Pospischil, M. M. Furchi and T. Mueller. *Solar-energy conversion and light emission in an atomic monolayer p-n diode.* Nature Nanotechnology, vol. 9, pages 257–261, April 2014. (Cited on page 2.)

[Postmus 1968] C. Postmus, J. R. Ferraro and S. S. Mitra. *Pressure Dependence of Infrared Eigenfrequencies of KCl and KBr.* Phys. Rev., vol. 174, pages 983–987, Oct 1968. (Cited on page 68.)

[Prasad 1993] S.V. Prasad and J.S. Zabinski. *Tribology of tungsten disulphide (WS_2): characterization of wear-induced transfer films.* Journal of Materials Science Letters, vol. 12, no. 18, pages 1413–1415, 1993. (Cited on page 3.)

[Qiu 2013] Diana Y. Qiu, Felipe H. da Jornada and Steven G. Louie. *Optical Spectrum of MoS_2: Many-Body Effects and Diversity of Exciton States.* Phys. Rev. Lett., vol. 111, page 216805, Nov 2013. (Cited on page 11.)

[Radisavljevic 2011] B. Radisavljevic, A. Radenovic, J. Brivio, V. Giacometti and A. Kis. *Single-layer MoS_2 transistors.* Nature Nanotechnology, vol. 6, pages 147–150, December 2011. (Cited on page 2.)

[Ramasubramaniam 2012] Ashwin Ramasubramaniam. *Large excitonic effects in monolayers of molybdenum and tungsten dichalcogenides.* Phys. Rev. B, vol. 86, page 115409, Sep 2012. (Cited on page 43.)

[Reshak 2003] Ali Hussain Reshak and S. Auluck. *Calculated optical properties of 2H-MoS_2 intercalated with lithium.* Phys. Rev. B, vol. 68, page 125101, Sep 2003. (Cited on page 3.)

[Rice 2013] C. Rice, R. J. Young, R. Zan, U. Bangert, D. Wolverson, T. Georgiou, R. Jalil and K. S. Novoselov. *Raman-scattering measurements and first-principles calculations of strain-induced phonon shifts in monolayer MoS_2.* Phys. Rev. B, vol. 87, page 081307, Feb 2013. (Cited on pages 38, 40 and 64.)

[Roldán 2014] Rafael Roldán, Jose A. Silva-Guillén, M. Pilar López-Sancho, Francisco Guinea, Emmanuele Cappelluti and Pablo Ordejón. *Electronic properties of single-layer and multilayer transition metal dichalcogenides MX_2 (M = Mo, W and X = S, Se).* Annalen der Physik, vol. 526, no. 9-10, pages 347–357, 2014. (Cited on pages 5, 6, 8, 9 and 94.)

[Rose 2013] Félix Rose, M. O. Goerbig and Frédéric Piéchon. *Spin- and valley-dependent magneto-optical properties of MoS_2.* Phys. Rev. B, vol. 88, page 125438, Sep 2013. (Cited on pages 90, 91, 92, 97, 98 and 104.)

[Ross 2013] Jason S. Ross, Sanfeng Wu, Hongyi Yu, Nirmal J. Ghimire, Aaron M. Jones, Grant Aivazian, Jiaqiang Yan, David G. Mandrus, Di Xiao and Xiaodong Yao Wang Xu. *Electrical control of neutral and charged excitons in a monolayer semiconductor.* Nature Communications, vol. 4, page 1474, 2013. (Cited on pages 40 and 45.)

[Ross 2014] J. S. Ross, P. Klement, A. M. Jones, N. J. Ghimire, J. Yan, D. G. Mandrus, T. Taniguchi, K. Watanabe, K. Kitamura, W. Yao, D. H. Cobden and X. Xu. *Electrically tunable excitonic light-emitting diodes based on monolayer WSe_2 p-n junctions.* Nature Nanotechnology, vol. 9, pages 268–272, April 2014. (Cited on page 2.)

[Ruppert 2014] Claudia Ruppert, Ozgur Burak Aslan and Tony F. Heinz. *Optical Properties and Band Gap of Single- and Few-Layer $MoTe_2$ Crystals.* Nano Letters, vol. 14, no. 11, pages 6231–6236, 2014. (Cited on page 33.)

[Scheuschner 2015] N. Scheuschner, R. Gillen, M. Staiger and J. Maultzsch. *Newly observed first-order resonant Raman modes in few-layer MoS_2.* ArXiv e-prints, March 2015. (Cited on pages 65 and 66.)

[Schmidt 2013] Peer Schmidt, Michael Binnewies, Robert Glaum and Marcus Schmidt. *Advanced Topics on Crystal Growth.* 2013. (Cited on page 32.)

[Schutte 1987] W.J. Schutte, J.L. De Boer and F. Jellinek. *Crystal structures of tungsten disulfide and diselenide.* Journal of Solid State Chemistry, vol. 70, no. 2, pages 207 – 209, 1987. (Cited on page 36.)

[Sekine 1980] T. Sekine, T. Nakashizu, K. Toyoda, K. Uchinokura and E. Matsuura. *Raman scattering in layered compound 2H-WS_2.* Solid State Communications, vol. 35, no. 4, pages 371 – 373, 1980. (Cited on pages 58, 63, 65, 75 and 76.)

[Shang 2015] Jingzhi Shang, Xiaonan Shen, Chunxiao Cong, Namphung Peimyoo, Bingchen Cao, Mustafa Eginligil and Ting Yu. *Observation of Excitonic Fine Structure in a 2D Transition-Metal Dichalcogenide Semiconductor*. ACS Nano, vol. 9, no. 1, pages 647–655, 2015. (Cited on pages 12 and 40.)

[Shin 2014] MinJu Shin, DongHak Kim and D. Lim. *Photoluminescence saturation and exciton decay dynamics in transition metal dichalcogenide monolayers*. Journal of the Korean Physical Society, vol. 65, no. 12, pages 2077–2081, 2014. (Cited on page 88.)

[Song 2013] Jeong-Gyu Song, Jusang Park, Wonseon Lee, Taejin Choi, Hanearl Jung, Chang Wan Lee, Sung-Hwan Hwang, Jae Min Myoung, Jae-Hoon Jung, Soo-Hyun Kim, Clement Lansalot-Matras and Hyungjun Kim. *Layer-Controlled, Wafer-Scale, and Conformal Synthesis of Tungsten Disulfide Nanosheets Using Atomic Layer Deposition*. ACS Nano, vol. 7, no. 12, pages 11333–11340, 2013. (Cited on pages 58, 67 and 68.)

[Sourisseau 1989] C. Sourisseau, M. Fouassier, M. Alba, A. Ghorayeb and O. Gorochov. *Resonance Raman, inelastic neutron scattering and lattice dynamics studies of 2H-WS_2*. Materials Science and Engineering: B, vol. 3, no. 1ï¿½2, pages 119 – 123, 1989. (Cited on pages 58, 63, 65, 67, 75, 76 and 77.)

[Sourisseau 1991] C. Sourisseau, F. Cruege, M. Fouassier and M. Alba. *Second-order Raman effects, inelastic neutron scattering and lattice dynamics in 2H-WS_2*. Chemical Physics, vol. 150, no. 2, pages 281 – 293, 1991. (Cited on pages 58, 65, 67, 69, 71, 75, 76 and 77.)

[Splendiani 2010] Andrea Splendiani, Liang Sun, Yuanbo Zhang, Tianshu Li, Jonghwan Kim, Chi-Yung Chim, Giulia Galli and Feng Wang. *Emerging Photoluminescence in Monolayer MoS_2*. Nano Letters, vol. 10, no. 4, pages 1271–1275, 2010. PMID: 20229981. (Cited on pages 1, 2, 8, 37 and 89.)

[Srivastava 2015] A. Srivastava, M. Sidler, A. V. Allain, D. S. Lembke, A. Kis and A. Imamoglu. *Valley Zeeman Effect in Elementary Optical Excitations of a Monolayer WSe_2*. Nature Physics, 2015. (Cited on pages 18, 40, 90, 92, 97 and 99.)

[Staiger 2012] Matthias Staiger, Peter Rafailov, Konstantin Gartsman, Hagen Telg, Matthias Krause, Gal Radovsky, Alla Zak and Christian Thomsen. *Excitonic resonances in WS_2 nanotubes*. Phys. Rev. B, vol. 86, page 165423, Oct 2012. (Cited on page 67.)

[Staiger 2015] M. Staiger, R. Gillen, N. Scheuschner, O. Ochedowski, F. Kampmann, M. Schleberger, C. Thomsen and J. Maultzsch. *Splitting of the monolayer out-of-plane A'_1 Raman mode in few-layer WS_2*. ArXiv e-prints, March 2015. (Cited on pages 63, 64, 65 and 67.)

[Sun 2014] Dezheng Sun, Yi Rao, Georg A. Reider, Gugang Chen, Yumeng You, Louis Brezin, Avetik R. Harutyunyan and Tony F. Heinz. *Observation of Rapid Exciton Exciton Annihilation in Monolayer Molybdenum Disulfide.* Nano Letters, vol. 14, no. 10, pages 5625–5629, 2014. PMID: 25171389. (Cited on page 88.)

[Tanaka 2005] Kenichiro Tanaka, Takayuki Takahashi, Takashi Kondo, Tsutomu Umebayashi, Keisuke Asai and Kazuhiro Ema. *Image charge effect on two-dimensional excitons in an inorganic organic quantum-well crystal.* Phys. Rev. B, vol. 71, page 045312, Jan 2005. (Cited on page 12.)

[Vanelle 2000] E. Vanelle, M. Paillard, X. Marie, T. Amand, P. Gilliot, D. Brinkmann, R. Lévy, J. Cibert and S. Tatarenko. *Spin coherence and formation dynamics of charged excitons in CdTe/CdMgZnTe quantum wells.* Phys. Rev. B, vol. 62, pages 2696–2705, Jul 2000. (Cited on page 83.)

[Verble 1970] J. L. Verble and T. J. Wieting. *Lattice Mode Degeneracy in MoS_2 and Other Layer Compounds.* Phys. Rev. Lett., vol. 25, pages 362–365, Aug 1970. (Cited on page 62.)

[Walck 1998] S. N. Walck and T. L. Reinecke. *Exciton diamagnetic shift in semiconductor nanostructures.* Phys. Rev. B, vol. 57, pages 9088–9096, Apr 1998. (Cited on page 101.)

[Wang 2012] Qing Hua Wang, Kourosh Kalantar-Zadeh, Andras Kis, Jonathan N. Coleman and Michael S. Strano. *Electronics and optoelectronics of two-dimensional transition metal dichalcogenides.* Nature Nanotechnology, vol. 7, page 699, 2012. (Cited on pages 33, 58 and 89.)

[Wang 2013] Qinsheng Wang, Shaofeng Ge, Xiao Li, Jun Qiu, Yanxin Ji, Ji Feng and Dong Sun. *Valley Carrier Dynamics in Monolayer Molybdenum Disulfide from Helicity Resolved Ultrafast Pump Probe Spectroscopy.* ACS Nano, vol. 7, no. 12, pages 11087–11093, 2013. PMID: 24224951. (Cited on page 80.)

[Wang 2014] G. Wang, L. Bouet, D. Lagarde, M. Vidal, A. Balocchi, T. Amand, X. Marie and B. Urbaszek. *Valley dynamics probed through charged and neutral exciton emission in monolayer WSe_2.* Phys. Rev. B, vol. 90, page 075413, Aug 2014. (Cited on pages 40, 41, 49, 52, 53, 82, 84, 90, 95 and 96.)

[Wang 2015] Haining Wang, Changjian Zhang and Farhan Rana. *Ultrafast Dynamics of Defect-Assisted Electron Hole Recombination in Monolayer MoS_2.* Nano Letters, vol. 15, no. 1, pages 339–345, 2015. PMID: 25546602. (Cited on page 85.)

[Weber W.H. 2000] Merlin R Weber W.H. Raman scattering in materials science. Material Science 42. Shpringer, 1st édition, 2000. (Cited on page 61.)

[Wildervanck 1970] J. C. Wildervanck. *Chalcogenides of Molybdenum, Tungsten, Technetium and Rhenium.* PhD thesis, Univ. of Groningen, 1970. (Cited on page 32.)

[Wilson 1969] J. A. Wilson and A. D. Yoffe. *The transition metal dichalcogenides discussion and interpretation of the observed optical, electrical and structural properties.* Advances in Physics, vol. 18, pages 193–335, May 1969. (Cited on pages 3 and 7.)

[Xiao 2012] Di Xiao, Gui-Bin Liu, Wanxiang Feng, Xiaodong Xu and Wang Yao. *Coupled Spin and Valley Physics in Monolayers of MoS_2 and Other Group-VI Dichalcogenides.* Phys. Rev. Lett., vol. 108, page 196802, May 2012. (Cited on pages 2, 14, 15, 91, 92, 98 and 104.)

[Xu 2014] X. Xu, W. Yao, D. Xiao and T. F. Heinz. *Spin and pseudospins in layered transition metal dichalcogenides.* Nature Physics, vol. 10, pages 343–350, May 2014. (Cited on pages 2, 13, 14, 82 and 89.)

[Yafet 1963] Y. Yafet. *g Factors and Spin-Lattice Relaxation of Conduction Electrons.* volume 14 of *Solid State Physics*, pages 1 – 98. Academic Press, 1963. (Cited on page 13.)

[Yan 2014] Rusen Yan, Jeffrey R. Simpson, Simone Bertolazzi, Jacopo Brivio, Michael Watson, Xufei Wu, Andras Kis, Tengfei Luo, Angela R. Hight Walker and Huili Grace Xing. *Thermal Conductivity of Monolayer Molybdenum Disulfide Obtained from Temperature-Dependent Raman Spectroscopy.* ACS Nano, vol. 8, no. 1, pages 986–993, 2014. (Cited on pages 68 and 71.)

[Yao 2008] Wang Yao, Di Xiao and Qian Niu. *Valley-dependent optoelectronics from inversion symmetry breaking.* Phys. Rev. B, vol. 77, page 235406, Jun 2008. (Cited on page 12.)

[Ye 2014] Z. Ye, T. Cao, K. O'Brien, H. Zhu, X. Yin, Y. Wang, S. G. Louie and X. Zhang. *Probing excitonic dark states in single-layer tungsten disulphide.* Nature, vol. 513, pages 214–218, September 2014. (Cited on page 11.)

[Yu 2014a] H. Yu, G.-B. Liu, P. Gong, X. Xu and W. Yao. *Dirac cones and Dirac saddle points of bright excitons in monolayer transition metal dichalcogenides.* Nature Communications, vol. 5, page 3876, May 2014. (Cited on pages 18, 54 and 86.)

[Yu 2014b] T. Yu and M. W. Wu. *Valley depolarization due to intervalley and intravalley electron-hole exchange interactions in monolayer MoS_2.* Phys. Rev. B, vol. 89, page 205303, May 2014. (Cited on pages 80 and 85.)

[Zaslow 1967] B. Zaslow and Melvin E. Zandler. *Two-Dimensional Analog to the Hydrogen Atom.* American Journal of Physics, vol. 35, no. 12, pages 1118–1119, 1967. (Cited on page 10.)

[Zeng 2012] H. Zeng, J. Dai, W. Yao, D. Xiao and X. Cui. *Valley polarization in MoS_2 monolayers by optical pumping.* Nature Nanotechnology, vol. 7, pages 490–493, August 2012. (Cited on pages 15, 17, 79 and 82.)

[Zeng 2013] Hualing Zeng, Gui-Bin Liu, Junfeng Dai, Yajun Yan, Bairen Zhu, Ruicong He, Lu Xie, Shijie Xu, Xianhui Chen, Wang Yao and Xiaodong Cui. *Optical signature of symmetry variations and spin-valley coupling in atomically thin tungsten dichalcogenides.* Scientific Reports, vol. 3, page 1608, 2013. (Cited on pages 9, 58, 68, 90 and 95.)

[Zhan 2012] Yongjie Zhan, Zheng Liu, Sina Najmaei, Pulickel M. Ajayan and Jun Lou. *Large-Area Vapor-Phase Growth and Characterization of MoS_2 Atomic Layers on a SiO_2 Substrate.* Small, vol. 8, no. 7, pages 966–971, 2012. (Cited on page 2.)

[Zhang 2014] Y. Zhang, T.-R. Chang, B. Zhou, Y.-T. Cui, H. Yan, Z. Liu, F. Schmitt, J. Lee, R. Moore, Y. Chen, H. Lin, H.-T. Jeng, S.-K. Mo, Z. Hussain, A. Bansil and Z.-X. Shen. *Direct observation of the transition from indirect to direct bandgap in atomically thin epitaxial $MoSe_2$.* Nature Nanotechnology, vol. 9, pages 111–115, February 2014. (Cited on pages 2 and 8.)

[Zhao 2013] Weijie Zhao, Zohreh Ghorannevis, Leiqiang Chu, Minglin Toh, Christian Kloc, Ping-Heng Tan and Goki Eda. *Evolution of Electronic Structure in Atomically Thin Sheets of WS_2 and WSe_2.* ACS Nano, vol. 7, no. 1, pages 791–797, 2013. (Cited on pages 9, 37, 40, 64, 68, 76 and 95.)

[Zhu 2014] C. R. Zhu, K. Zhang, M. Glazov, B. Urbaszek, T. Amand, Z. W. Ji, B. L. Liu and X. Marie. *Exciton valley dynamics probed by Kerr rotation in WSe_2 monolayers.* Phys. Rev. B, vol. 90, page 161302, Oct 2014. (Cited on pages 80 and 96.)

Probing the electronic properties of bulk and monolayer crystals of dichalcogenides using magneto-spectroscopy.

Abstract: Layered compounds involving transition metals from group VI and chalcogens (the so-called dichalcogenides) are promising candidates for exploring atomically thin structures. Bulk crystals are semiconductors with an indirect gap in the near infrared spectral range. In contrast, monolayer dichalcogenides are 2D semiconductors with a direct gap in the *visible spectral range*. Moreover, the inversion symmetry breaking together with strong spin-orbit coupling in monolayer dichalcogenides leads to valley contrasted optical selection rules. As a consequence, the population of each valley can be controlled by the circular polarization of light. Therefore, monolayer dichalcogenides have been proposed as a building block for valleytronics. However, for applications an understanding of the electronic properties is crucial.

In this thesis, we have studied tungsten dichalcogenides (WS_2 and WSe_2) by means of steady-state μ-photoluminescence (μPL) and Raman spectroscopy, optical interband absorption and time-resolved μPL techniques in the visible spectral range combined with high magnetic fields.

We demonstrate that the ratio between the trion and exciton emission can be tuned by varying the power of the laser used for excitation of the μPL in *ungated* monolayer WS_2 and WSe_2 samples. Moreover, the intensity of the trion emission can be independently tuned using additional sub band gap illumination. This is a direct evidence that we can control the density of carriers in a 2D system.

We have investigated the resonant Raman scattering in a WS_2 monolayer. We observe a second order longitudinal acoustic mode (2LA) at only $4cm^{-1}$ below the first order E^1_{2g} mode. We demonstrate, that depending on the intensity ratio and the respective line widths of these two peaks, any analysis which neglects the presence of the 2LA mode can lead to a potentially incorrect assignment for the number of layers.

The valley dynamics in monolayer WSe_2 has been probed by monitoring the emission and polarization dynamics of neutral and charged excitons in μPL. We demonstrate that the exciton inter valley scattering between the K+ and K- valleys is in the order of several picoseconds.

Finally, using magneto-spectroscopy studies, we reveal the very different nature of carriers in monolayer and bulk dichalcogenides. We demonstrate that in monolayer WSe_2, the carriers behave as massive Dirac fermions, while in bulk WSe_2 we observe a distinctly excitonic behavior which is best described within the hydrogen model.

Keywords: Dichalcogenides, monolayer, bulk, massive Dirac fermions, Fermi velocity, valley splitting.

Etude des propriétés électroniques de monocristaux massifs et monocouches de dichalcogénures par magnéto-spectroscopie.

Résumé: Les composés stratifiés dits "dichalcogénures" impliquant des métaux de transition du groupe VI et des chalcogénes sont des candidats prometteurs pour l'étude des propriétés électroniques de structures atomiquement minces. Tandis que les monocristaux massifs sont des semi-conducteurs à gap indirect dans la plage spectrale du proche infrarouge, la monocouche possède un gap direct dans le domaine du visible. Dans cette dernière, la brisure de symétrie d'inversion et la présence d'un fort couplage spin-orbite mènent à différentes règles de sélection optique pour chaque vallée du semi-conducteur. Ainsi, dans chaque vallée, la population de porteurs de charge peut être modulée par la polarisation circulaire de la lumière, faisant des monocouches des candidats potentiels pour l'électronique de vallée. Cependant, avant toute application, la compréhension de leurs propriétés électroniques est cruciale.

Dans cette thèse, nous avons étudié les propriétés électroniques de WS_2 et WSe_2 par μ-photoluminescence (μ-PL), spectroscopie Raman, absorption optique inter bande et μ-PL résolue en temps combinées avec des champs magnétiques intenses.

Nous montrons que l'émission de l'exciton par rapport au trion dans les monocouches de WS_2 et WSe_2 est fonction de la puissance du laser utilisé pour l'excitation de la μ-PL. De plus, nous montrons que l'intensité de l'émission du trion peut être contrôlée indépendamment en utilisant une énergie d'excitation plus basse que la bande interdite. Il s'agit d'une preuve du contrôle de la densité de porteurs dans ces systèmes 2D.

Nous avons également étudié la diffusion Raman en résonance dans une monocouche de WS_2. Nous observons un mode acoustique longitudinale (2LA), seulement $4cm^{-1}$ en-dessous du mode E^1_{2g}. Nous montrons qu'en fonction du rapport des intensitée et la largeur de ligne de chacun de ces deux pics, toute analyse qui néglige la présence de la mode 2LA peut conduire à une estimation incorrecte du nombre de couche.

Les propriétés électroniques de chaque vallée d'une monocouche de WSe_2 ont été sondées par μ-PL via l'étude de l'émission et de la polarisation des excitons neutres et chargés. Nous montrons que le temps de diffusion de l'exciton entre les vallées de K + et K- est de l'ordre de plusieurs picosecondes.

Enfin, grâce à la magnéto-spectroscopie, nous mettons en évidence différents types de porteurs de charges entre la monocouche et le cristal massif de dichalcogénures. Nous montrons que dans la monocouche, les porteurs de charge se comportent comme des fermions massifs Dirac, tandis que dans le monocristal de WSe_2 nous observons un comportement excitonique, décrit par le modèle de l'atome d'hydrogène.

Mots clés: Dichalcogénures, monocouche, fermions massifs Dirac, vitesse Fermi.